Abstract

This thesis deals with the self-organization of individual building blocks, specifically organic molecules and metal atoms, into supramolecular structures on metal surfaces under ultra high vacuum conditions (UHV). Self-organization of supramolecular systems is a promising candidate for a bottom-up approach in the fabrication of complex structures with specific properties. This process is steered by interactions between functional groups of the individual building blocks and is of apparent interest to gain a detailed understanding of the influence and the behavior of these functional groups enabling intermolecular binding. In the first part of the thesis, we investigate hydrogen bonded structures on metal surfaces. Of especial interest is the possibility of the formation of *ionic hydrogen* bonds, a special class of hydrogen bond which connects a charged donor (acceptor) and a neutral acceptor (donor) and is important in biological systems. By combined Scanning Tunneling Microscopy (STM), X-ray Photoelectron Spectroscopy (XPS) and Near Edge X-ray Absorption Fine Structure (NEXAFS) measurement we show the deprotonation of carboxylic functions in the molecules, forming carboxylate groups involved in intermolecular binding. With our complementary experimental and theoretical examinations we clearly show that the carboxylate groups are indeed still charged although adsorbed onto a conducting metal surface and that the observed structures can be computationally reproduced by using these charges in classical molecular dynamic calculations. Our investigations clearly reveal that all requirements for the formation of *ionic hydrogen* bonds in these samples at metal surfaces under solvent free conditions are fulfilled. In the second part, the confinement of surface state electrons in self-assembled hydrogen-bonded structures is investigated. The examined structure contains two-dimensional cavities, with different inner diameters in the periodic arrangement and in domain boundaries. Inside the cavities we detect a spatially localized modification in the local density of states (LDOS) of the Ag(111) surface state electrons. The energy of the peak correlates with the cavity area as predicted by a simple "particle in a box" model. This clearly shows that the surface state electrons form a confined state inside the cavities. Furthermore we examine self-assembled periodic structures as templates for binding single macrocyclic molecules. The macrocyclic molecules can be deposited by sublimation, as STM-topographs with submolecular resolution reflect the shape of the intact molecules and reveal a coverage dependent aggregation behavior. We show that it is possible to fabricate a structure in which at most one macrocyclic molecule per pore can be found in a defined binding position. In the last part of the thesis we investigate the influence of individual metal atoms on the chemical activity and the self-assembly process of molecules on metal surfaces. First, we demonstrate the high chemical reactivity of these metal atoms. In our experiments we address the chemical reactivity of static *active sites*, like kinks and step edges, and of dynamic *active sites*, like the metal atoms, separately. Doing this we show that a non-negligible amount of the chemical reactivity of a metal surface is due to this dynamic adatom gas. Furthermore the influence of metal atoms on the structure formation of organic molecules is investigated. We show that two-dimensional structures based on a complex formation between metal centers and ligands can be formed and that the coordination number is independent of the substrate symmetry. Furthermore, we show the possibility that on metal surfaces one can prepare three-fold coordinated Fe-centers, a coordination number which is rarely seen in three dimensional chemistry. In the last part we study catenanes, which consist of two interlocked macrocyclic molecules. Main interest is on the confirmation of a structural change of the catenanes adsorbed on a metal substrate. For our experiments we use the fact that the catenanes are designed to "trap" a Cu-atom by complex formation. As this reaction is associated with a structural change and a change in intermolecular interaction, we can verify a reaction of catenanes adsorbed onto a surface with Cu adatoms and therefore a structural alteration by simply imaging the formed structures. Our measurements show the possibility of depositing large molecules like catenanes by sublimation and of their potential for use as molecular machines adsorbed onto metal surfaces.

Self-organization, organic molecules, metal surfaces, Scanning Tunneling Microscopy, X-ray Photoelectron Spectroscopy, Near Edge X-ray Absorbtion Fine Structure

Zusammenfassung

In dieser Arbeit wird die Selbstorganisation von individuellen Bausteinen, wie organischen Moleküle und Metallatome, zu supramolekularen Strukturen auf Metalloberflächen unter Vakuumbedingungen untersucht. Die Selbstorganisation von supramolekularen Systemen ist ein vielversprechender Kandidat für den sogenannten "bottom-up" Ansatz, welcher die Erzeugung von komplexen Strukturen mit definierten Eigenschaften aus einfacheren Bausteinen beschreibt. Dieser Prozess wird durch das Zusammenspiel von funktionellen Gruppen, die Bindungen zwischen den Molekülen ermöglichen, gesteuert. Ein detailliertes Verständniss des Verhaltens und des Einflusses dieser funktionellen Gruppen auf die gebildeten Strukturen ist von offensichtlichem Interesse und Untersuchungen darüber stellen den Inhalt dieser Arbeit dar. Im ersten Teil der Arbeit untersuchen wir durch Wasserstoffbrücken gebundene Systeme auf Metalloberflächen. In diesen Systemen ist die Bildung von ionischen Wasserstoffbrücken von besonderem Interesse. Diese spezielle Klasse von Wasserstoffbrücke ist in der Biologie von Relevanz und verbindet einen geladene Donator (Acceptor) mit einem neutralen Acceptor (Donator). Durch kombinierte Messungen mittels Rastertunnelmikroskopie, Röntgen-Photolektronenspektroskopie und Röntgen-Absorptionsspektroskopie zeigen wir die Bildung von Carboxylatgruppen, welche in intermolekulare Bindungen involviert sind. Durch das Zusammenspiel unserer experimentellen und theoretischen Untersuchungen zeigen wir, dass die Carboxylatgruppen trotz Adsorbtion auf einer Metalloberfläche eine elektrische Ladung tragen. Durch Einbeziehen dieser Ladungen in Modellrechnungen können die beobachteten Strukturen reproduziert werden. Unsere Untersuchungen zeigen eindeutig, dass in diesen Systemen alle Anforderungen für die Existenz von ionischen Wasserstoffbrücken erfüllt sind. Im zweiten Teil wird untersucht, ob Oberflächenelektronen diesen selbstorganisierten Strukturen eine stehende Welle bilden können. Die untersuchte Struktur beinhalten zweidimensionale "Hohlräume" mit unterschiedlichen inneren Durchmessern in der periodischen Anordnung und in Domänengrenzen. Im Inneren dieser Hohlräume kann eine räumlich und energetisch begrenzte Veränderung der lokalen elektronischen Zustandsdichte der Oberflächenelektronen festgestellt werden. Der Zusammenhang zwischen der Energie bei der die Veränderung der Zustandsdichte zu finden ist und der Fläche des Hohlraumes kann durch ein simples ”Teilchen in der Box” Modell beschrieben werden. Dies zeigt, dass in diesen Hohlräume die Oberflächenelektronen eine stehende Welle bilden. Desweiteren testen wir die Verwendung diese periodischen, selbstorganisierten Strukturen als Schablone für die Bindung einzelner makrozyklischer Moleküle. Die verwendeten makrozyklischen Moleküle können durch thermische Sublimation deponiert werden und zeigen ein bedeckungsabhängiges Aggregationsverhalten. Wir zeigen, dass es möglich ist Strukturen herzustellen in denen allerhöchstens ein einzelnes makrozyklisches Molekül pro Pore gefunden werden kann. Im letzten Teil der Arbeit wird der Einfluss einzelner Metallatome auf die chemische Aktivität der Oberfläche und den Selbstorganisationsprozess von Molekülen untersucht. Dazu untersuchen wir die chemische Reaktivität von statischen Reaktionszentren, wie Stufenkanten, und von dynamischen Reaktionszentren, wie der Metallatome, getrennt. Wir zeigen, dass in dem betrachteten Modellsystem ein nicht unerheblicher Teil der chemischen Reaktivität der Metalloberfläche ihren Ursprung in den individuellen Metallatomen hat. Weiters wird der Einfluss von Metallatomen auf die Selbstorganisation von organischen Molekülen untersucht. Wir zeigen, dass in zweidimensionalen Strukturen die auf einer Komplexbildung zwischen Metallzentren und organischen Liganden basieren die Koordinationszahl des Metallzentrums unabhängig von der Symmetrie des Substrats ist. Weiters zeigen wir die Bildung von dreifach koordinierten Fe-Zentren, einer Koordinationszahl die in dreidimensionalen Systemen selten zu beobachten ist. Im letzten Teil untersuchen wir Catenane, welche aus zwei ineinander verbundenen makrozyklischen Molekülen bestehen. Hauptaugenmerk liegt auf der Bestätigung des Konzepts, dass an eine Metalloberfläche gebundene Catenane strukturelle Änderungen durchführen können. Für unsere Experimente machen wir uns die Komplexbildung zwischen Cu-Zentren und Liganden auf den Catenanen zu eigen. Diese Reaktion ist nicht nur verbunden mit einer Änderung in der Form der Moleküle, sondern auch mit Änderungen im intermolekularen Bindungsverhalten. Eine Reaktion der Catenane mit den Cu-Atome und die einhergehende Formänderung kann damit einfach durch Beobachtung der geformten Struktur feststellt werden. Unsere Messungen zeigen die Möglichkeit, grosse Moleküle wie Catenane durch Sublimation zu deponieren und ihre Fähigkeit, auf Metalloberflächen als molekulare Maschinen zu agieren.

Selbstorganisation, organische Moleküle, Metalloberflächen, Rastertunnelmikroskopie, Röntgen-Photolektronenspektroskopie, Röntgen-Absorptionsspektroskopie

Contents

Chapter 1

Abbreviations and Symbols

UHV	Ultra High Vacuum
STM	Scanning Tunneling Microscopy
STS	Scanning Tunneling Spectroscopy
IETS	Inelastic Electron Tunneling Spectroscopy
XPS	X-ray Photoelectron Spectroscopy
NEXAFS	Near Edge X-ray Absorption Fine Structure
TEY	Total Electron Yield
BE	Binding Energy
OMBE	Organic Molecular Beam Epitaxy
TMA	1,3,5-benzene-tricarboxylic acid
BTA	4,4′,4″-benzene-1,3,5-triyl-tri-benzoic acid
mt33	macrocyclic molecule $C_{45}H_{35}N_5O_2$
cat30	catenane molecule $C_{68}H_{68}N_4O_{12}$
TPA	1,4-benzene-dicarboxylic acid
DHBP	4,4′ dihydroxybiphenyl
MOCN	Metal-Organic Coordination Network
2D	two dimensional
ML	MonoLayer
z	tip sample distance
U	Bias voltage
I	Tunneling current
LDOS	Local Density Of States
e	elementary charge $1.602 * 10^{-19}$C
$\hbar$	natural unit of action $1.054 * 10^{-34}$Js
m_e	mass of electron $9.109 * 10^{-31}$kg
FWHM	Full Width at Half Maximum

k	wave vector
m*	effective mass of electron 0.40m$_e$
Θ	step function
ρ	LDOS
U_{stab}	stabilization voltage of the tip
I_{stab}	stabilization current of the tip
f	modulation frequency of lock-in amplifier
V_{pp}	modulation amplitude of lock-in amplifier (peak to peak)

Chapter 2

Introduction

With the advancement of technology the building units of industrially fabricated structures get smaller and smaller. As an example, the Intel Pentium $4^{©}$ processor in 2006 is fabricated with the *65nm process*, with the transistors having a gate length of 32nm and a gate oxide thickness of 1.2nm [1]. The understanding of the properties of such structures as well as possibilities for their modification is based on the application of quantum mechanics to solid state physics, especially bulk-like systems (infinite and periodic crystals). But the description of the properties and functions of such devices is still a projection of macroscopic concepts onto smaller length scales. If the structures shrink to a size comparable to the typical length scale of quantum effects, the physical properties will deviate significantly from those of the bulk material and a further miniaturization by a simple scaling down of the components will become more and more complicated [2]. But the appearance of quantum effects due to decreasing feature size can become an advantage, if one can utilize the different properties of nanoscale objects to produce novel type of applications [3].

A detailed understanding of the quantum effects in structures with a length scale of only a few nanometer is a prerequisite for their use and a targeted modification. One way to gain an understanding of quantum effects in nanometer-scale structures is their investigation when adsorbed onto a surface, as a large variety of measuring techniques can be applied. Especially Scanning Tunneling Microscopy (STM) offers access to local physical properties at the atomic scale. For example, the influence of a single magnetic atom on the local properties of a non-magnetic substrate can be addressed on the atomic scale [4, 5] as well as single-molecule vibrational spectroscopy with spatial resolution on the atomic scale [6, 7]. It is also possible to manipulate single atoms and molecules into desired structures when adsorbed onto surfaces by means of Scanning Tunneling Microscopy (STM) [8, 9].

Building nanostructures atom-by-atom with STM enables the fabrication of an immense variety of structures interesting for fundamental research but is a time-consuming process not suitable for industrial applications. And as only a minute fraction of the surface can be covered with the fabricated nanostructures, it is only suitable for local probe investigations and not for measurement techniques which integrate over an extended area of the surface. A promising approach for a controlled, predictable and fast fabrication of extended structures with features in the nanometer scale regime is the self-assembly of organic supramolecular structures on metal substrates [10]. Self-organization describes the modular assembly of simple building blocks, e.g. molecules containing functional groups, into complex architectures steered by the interaction between the functional groups. The spatial arrangement of the building blocks and the functionality of the resulting supramolecular structure is determined by directional intermolecular interactions. These are non-covalent bonds such as hydrogen bonding, van der Waals forces, metal-ligand complex formation, etc., and are of weak or intermediate bonding strength. The various bond types differ in their directionality, strength and bond length.

Apart from its use as template to study nanostructures, the properties of the surface itself are of outstanding importance e.g. for heterogeneous catalysis. Obviously, one wants to be able to modify the properties of a surface in a controlled way. One way to modify the properties of surfaces can be by self-assembled adsorbates, delivering specific binding sites or modifying the electronic or optical properties of the surface. For example, it is possible to create chiral architectures at surfaces which can stereodirect chemical reactions [11].

Within this thesis, we examine the properties of organic molecules on metal surfaces with an emphasis on understanding the influence of the intermolecular binding and the role of the metal surface on the self-assembly process and the formed supramolecular structures. The thesis is organized as follows:

Chapter 2 gives an introduction on the experimental setup and the experimental techniques used. The setup of our home-built Besocke-type STM, the damping system, the cryostat and the vacuum system are explained. The setup for the X-ray Photoelectron Spectroscopy (XPS) and for the Near Edge X-ray Adsorption Fine Structure (NEXAFS) measurements at the HE-SGM beamline at the BESSY 2 synchrotron radiation facility in Berlin is explained. Information on the sample preparation is also given.

In Chapter 3 the theoretical background of STM, XPS and NEXAFS is explained. Special emphasis is laid on the theoretical background of STM, which is necessary to understand the two main modes of operation of STM used within this thesis, the *constant current* mode for acquiring topographic information of the sample and *tunneling spectroscopy* for acquiring information on the local density of states (LDOS) of the substrate. A simple method for the quantification of XPS-data used to acquire the relative concentrations of different chemical states from the XPS-spectra is explained.

In Chapter 4 our experiments on supramolecular self-assembly via hydrogen bonding at metal surfaces are presented. Hydrogen bonding is one of the most important bonding motifs in nature and therefore of especial interest and a well-investigated bonding motif in supramolecular chemistry on metal surfaces [12, 13, 14, 15, 16, 17, 18]. One class of hydrogen bond is the *ionic hydrogen* bond, which connects charged donors (acceptors) and neutral acceptors (donors) [19]. Although well-investigated in solution, they have not been examined on metal substrates up to now. An essential prerequisite for the formation of *ionic hydrogen* bonds on a metal surface is of course that an electric charge can rest on the molecules and is not compensated or shielded by electrons of the substrate. The main goal of our experimental and theoretical investigations is to identify charged groups in organic molecules adsorbed onto a metal substrate and to reveal the influence of these charges on the self-assembly process and the formed supramolecular structures.

In Chapter 5 the influence of supramolecular self-assemblies on the Shockley-type surface state of a noble metal (111) surface, in which the electrons show the behavior of a two-dimensional electron gas, is investigated. Various measurements on the influence of adsorbates, like metal atoms [20, 21] and organic molecules [22], show that these adsorbates scatter the surface state electrons and furthermore that one can confine surface state electrons in structures on the surface [23, 24, 25, 26, 27], modifying the electronic properties of the surface. Considering this, we investigate the possibility of a confinement of the surface state electrons in self-assembled supramolecular structures. This will not only enable a fast production of such structures, but also the fabrication of periodic ensembles of uniform quantum corrals, which allow the use of integrating measurement methods.

Large and complex molecules adsorbed onto surfaces have been examined in solution [28, 29, 30, 31, 32, 33], but little is known about their behavior under solvent-free conditions. Therefore we report in Chapter 6 of experiments on macrocyclic molecules, precursors for rotaxanes and catenanes which are promising candidates for molecular machines. Catenanes are two mechanically interlocked macrocyclic rings whereas rotaxanes consist of a dumbbell shaped molecule mechanically interlocked into a macrocyclic molecule. We are mainly interested in the sublimation of large molecules like macrocycles and their behavior adsorbed onto a Ag(111) surface. Furthermore we test the possibility of using self-assembled periodic structures as template for binding single macrocyclic molecules.

In Chapter 7 we investigate the influence of metallic adatoms on organic molecules adsorbed onto metal substrates. This is of special importance as this adatom gas is native to every metal surface, notably at elevated temperatures [34, 35, 36, 37, 38] and individual metal atoms show a high chemical reactivity [39, 40, 41]. Furthermore, the metallic adatom gas can also be of artificial origin. In the first part of this chapter we use a model system to investigate the influence of this single metal atoms on the chemical reactivity of a metal substrate, which is important for heterogeneous catalysis. In the second part we study the complex formation between ligands and metal centers, as this is a possibility to create supramolecular structures on surfaces [42, 43, 44, 45, 46, 47, 48, 49]. In particular, we want to examine to what extent the substrate symmetry influences the coordination number of the metal centers in the compounds. In the last chapter, we study the possibility to use catenanes adsorbed onto a metal surface as molecular machines. The main goal of the experiments was to investigate if catenanes can act as molecular machines by performing conformational changes when adsorbed onto a substrate. We therefore investigate catenanes which can "incorporate" Cu atoms due to complex formation. This complex formation is not only connected to an alteration of the molecular shape, the attribute we are interested in, it also modifies the intermolecular binding motif and therefore the formed structures, which can be used to detect the structural changes of the adsorbed molecule.

Chapter 3

Experimental setup

3.1 The Scanning Tunneling Microscope

The main scientific instrument used within this work is the Scanning Tunneling Microscopy (STM), developed by Gerd Binning and Heinrich Rohrer [50] which utilizes the wave nature of electrons to determine spatially resolved topographic, electronic and vibrational properties of surfaces and adsorbates. In Figure 3.1 the basic idea of an STM is shown. Between the tip and sample, which are separated by a small gap of width z, a bias voltage U is applied. If z is small enough ($\sim$1nm) a tunneling current between tip and sample in the order of 1nA can be detected. As the tunneling current I depends exponentially on the distance z, one can obtain a topographic image of the sample surface with very high spatial resolution by scanning the tip over the sample. The experimental challenges in performing STM are manifold: The tip has to be approached over a macroscopical distance in microscopical steps to avoid crashing into the sample surface. Once the approach is finished, the tip-sample distance has to be stable in the picometer regime to achieve the necessary resolution. As the tunneling current I is typically smaller than 1nA, particular attention has to be paid to the wiring to avoid a cross-talk between different signals.

The STM used for our experiments is of Besocke-type. The coarse approach is carried out by a slip-stick motion of helical ramps resting on balls mounted to piezos, which can induce a movement [51]. In our design we want to have the possibility for an easy *in situ* exchange of both sample and tip. In conventional Besocke-type STMs this is not trivial, as both the tip and the sample are connected to wires to establish electrical contacts and furthermore mechanical forces on the piezos have to be avoided, making a considerable demand on the mechanical design. To simplify our design, the

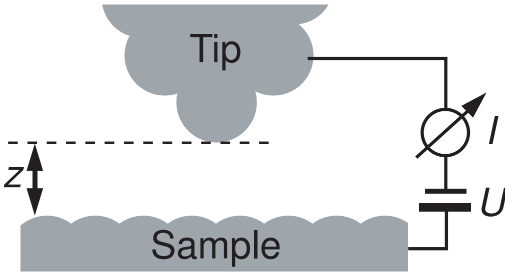

Figure 3.1: Principle idea of Scanning Tunneling Microscopy. A bias voltage U is applied between a tip and a sample and the tunneling current I is measured. In constant current mode used in all our topographic measurements a feedback loop controls the z distance to maintain a constant I. By scanning the tip over the surface and simultaneously recording z one can obtain a “topographic“ image of the surface.

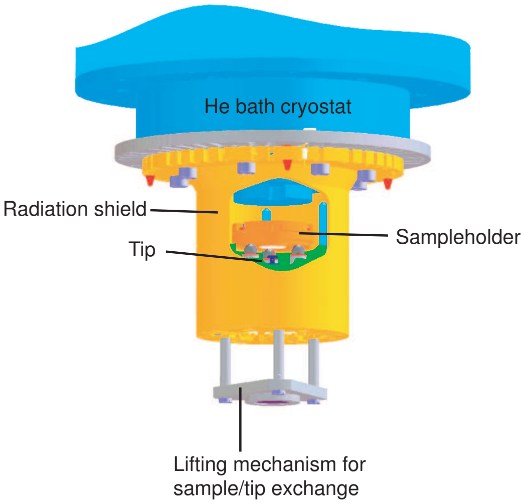

Figure 3.2: Sketch of our Besocke-type STM, one can see the principle design: The Mo-sampleholder has three helical ramps, with which it rests on CuBe-covered balls mounted on the coarse approach piezos. By appropriate actuation of the coarse approach piezos one can induce a rotational movement of the sampleholder by a slip-stick motion. Due to the helical ramps, one can approach or retract the sample to the tip, which is placed on a piezo in the middle of the coarse approach piezos. By a different actuation of the coarse piezos one can also shift the sampleholder horizontally.

bias voltage contact to the sample is made via the helical ramps and the balls of the coarse approach mechanism [52], with the design of the STM being shown in Figure 3.2. Sample exchange in our STM is performed by lifting up the sampleholder to avoid forces on the piezos and taking the sampleholder out with the wobblestick and vice versa. The tip is magnetically mounted to the scan piezo and can be exchanged by a tip exchange mechanism which can be introduced into the STM instead of a sample holder. The tip can be fixed and released from the tip exchange mechanism with the use of the wobblestick while the exchange mechanism rests on guiding rods to impede mechanical forces on the piezos. The main advantage in this design brings also a drawback. In the design used for our STM, the balls used for a slip-stick motion have to be conductive to establish an electrical contact to the sample. Whereas in conventional designs often ruby balls are used, we had to use metal balls. The problem using metal balls on metal ramps (molybdenum in our system) is that an intermixing of the material of the balls and the ramps can be expected, which cold-welds the two parts and hinders the slip-stick motion. This problem is solved by using CuBe as material for the balls, as Cu and Mo are inmixable [53]. Instead of bulk CuBe-balls we use a 0.125mm thick CuBe foil, which is glued on top of TiC-balls. An abrasion of this foil takes place, but only in a negligible quantity. The foil was replaced the first time after almost two years of use. Another disadvantage of our system is the magnetic anchorage of the tip to the scan piezo, which makes this design unsuitable for measurements of magnetic properties or measurements where magnetic fields have to be applied.

We use electrochemically etched polycrystalline W-tips (purity ∼99%), with a diameter of 0.2mm and a length of ∼5mm. The length of the tip has to be carefully adjusted as the height difference of the coarse approach is limited to a distance of 700μm. The tip is cleaned *ex situ* by etching with HF and *in situ* by field emission ($U\sim$600V and $I\sim$200μA). During operation the tip is cleaned by gently dipping it into the surface to remove small dirt particles.

The STM is used in two different ways: the constant current mode to acquire topographic information and the spectroscopic mode to acquire information on the local density of states and the work function. In the constant current mode the tunneling current I is compared during scanning over the surface with a preset current value and the difference is fed back to the z-piezo to minimize the difference between measured and preset current. The voltage applied to the z-piezo is recorded during scanning and used to compile a topographic image of the surface. In the spectroscopic mode several subtypes can be distinguished: In point-spectroscopy the differential tunneling conductance as a function of the bias voltage is recorded for a fixed tip position, providing information of the local density of states at this point. This is done by opening the feedback loop and ramping the bias voltage. The differential conductance is derived from the tunneling current with a lock-in amplifier. Instead of ramping the bias voltage U, one can also ramp the tunneling gap z, the $I(z)$ curves provide information on the work function of the surface. Furthermore it is possible to scan the surface at a given bias voltage U and tunneling current I and record at the same time the differential conductance. This gives a map of the spatial distribution of the local density of states at this certain bias voltage U.

Typical tunneling parameters for our measurements are a bias voltage of 500mV and a tunneling current of 500pA for TMA-, BTA-, TPA- and DHBP-structures as they are very stable. On mt33- and cat30-structures the bias voltage U has to be increased up to 2V and the tunneling current I has to be decreased down to 100pA to prevent a shifting of the molecule due to a tip-molecule interaction as the intermolecular forces and the binding forces to the surface are very small in these systems. Typical settings for the lock-in amplifier are a modulation amplitude of 10mV, a modulation frequency of 5kHz and an integration time of 3ms.

The STM measurements are performed using an SPM100 electronics of RHK with a home-built high-voltage amplifier for driving the coarse approach piezos. We use a DLPCA-200 from Femto as preamplifier for the tunneling current set to a gain of 10^8V/A. The tunneling current is low-pass filtered with a cut-off frequency of 3kHz. The bias voltage is low-pass filtered with a cut-off frequency of 10Hz and can be divided by 1 to 100 to fit the voltage range of interest to the bit resolution of the DA converter of the RHK electronics (±10V, 12bits). All signal lines are radio-frequency filtered on top of the cryostat. The lock-in amplifier is a Model 5110 from EG&G Princeton Applied Research.

3.2 The vacuum and damping system of the Scanning Tunneling Microscope

As we want to perform measurements on well-defined surfaces we have to avoid the contamination of our samples. Especially the adsorption of residual gas would perturb our measurements or even make them impossible. To achieve maximal cleanness all our experiments are therefore performed under ultra-high vacuum (UHV) conditions.

The UHV-system (Figure 3.3) consists of two main parts: a preparation chamber and an analysis chamber, separated by a gate valve. The prepara-

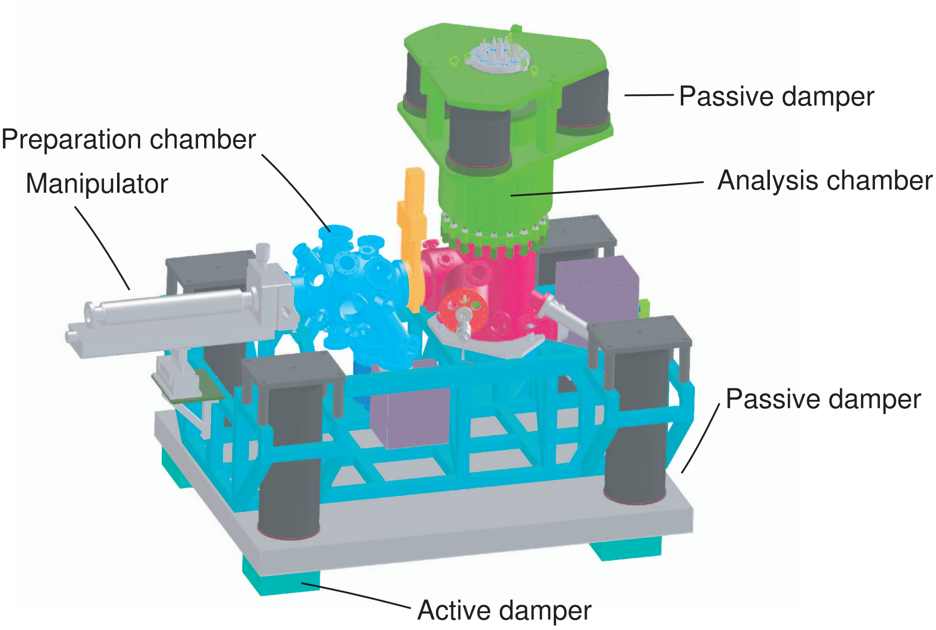

Figure 3.3: The vacuum system. It consists of two main chambers, the preparation chamber and the analysis chamber. The preparation chamber contains all equipment necessary for sample preparation and the analysis chamber contains the STM attached to the He bath cryostat. The whole system is pumped by a three-stage pumping system to a base pressure smaller 1×10^{-9}mbar. A three-stage damping system consisting of active and passive dampers decouples the STM from vibrations.

tion chamber is equipped with the equipments necessary for sample cleaning and preparation whereas the analysis chamber mainly contains the STM attached to a liquid He bath cryostat. The separation of preparation chamber and analysis chamber is mandatory as otherwise the Ar gas used for sputtering would condense on the cryostat, which has to be strictly avoided.

In the preparation chamber the base pressure is 3×10^{-10}mbar and the analysis chamber 3×10^{-11}mbar. Furthermore, a load lock exists to transfer samples and tips in and out of the UHV system without breaking the vacuum. The system is pumped by three different pumping stages. The first stage is a membrane pump, providing a pressure of $\sim$1mbar used as pre-vacuum for the second pumping stage, a turbo pump which is providing a pressure of $\sim1\times10^{-5}$mbar. This vacuum is used as pre-vacuum for the third pumping stage, the main turbo pump which is pumping the preparation chamber. Between main turbo pump and preparation chamber is a gate valve. During STM and STS measurements the mechanical pumps can be switched off to reduce the vibrations and the preparation chamber and the analysis chamber are pumped by ion-getter pumps attached to each chamber. Furthermore, the second pumping stage provides the pre-vacuum for the turbo pump pumping the load lock, to pump the gas-tubes and to pump the rotational feed-through of the sample-manipulator.

The preparation chamber is equipped with pressure gauges, a quadrupol mass spectrometer, a sputter gun, evaporators and gas dosing equipment. For sample handling a manipulator and a wobble-stick are installed. Also the load lock is attached to the preparation chamber and can be pumped and baked individually from the rest of the system. Two different types of evaporators are attached to the preparation chamber. Organic Molecule Beam Epitaxy (OMBE) sources for depositing molecules and electron beam evaporators for depositing metals. The evaporators are mounted to small load locks, so one can exchange the materials to be deposited without breaking the vacuum. Gas dosing is performed with gas lines, which can be pumped with the pre-vacuum from the second pumping stage to clean the line. Positioning of the sample in front of the different cleaning and preparation devices within the preparation chamber and transfer to the analysis chamber is done with a manipulator, which can be moved translational along the x, y and z axis and rotated freely around the z-axis. The sample can also be cooled down to $\sim$50K with liquid He or annealed up to $\sim$1000K with electron beam heating inside the manipulator, which is equipped with connections to the thermocouple contacts of the sample holder.

The analysis chamber is equipped with a pressure gauge, the bath cryostat, the STM, a wobble stick for sample- and tip-holder-handling and a storage for the samples and tip holders. The cryostat consists of two parts: The outer, tube-like liquid N_2 bath cryostat acts as a radiation shield for the inner He bath cryostat. The liquid N_2 bath cryostat contains approximately 36 liters of liquid N_2, which lasts for three days and can be pumped to freeze the N_2 to minimize vibrations due to boiling. The inner cryostat contains approximately 10 liters of liquid He, which also lasts for three days. The STM is directly mounted to the He-cryostat, without any further damping which has the advantage of an extremely good thermal contact, reflected in a fast cooling of the sample to 5K, but the disadvantage of a high sensitivity to vibrations. The STM is shielded against thermal radiation by two rotatable radiation shields and is accessible for sample or tip exchange by two windows, which can be opened by rotating the shields in the correct positions.

As in Scanning Tunneling Microscopy one measures elongations in the sub-nanometer range, the damping of vibrations is a crucial point. To be undisturbed from external high-frequency noise one has to built the STM itself as rigid as possible to have a high eigenfrequency in the range of kilohertz.

The low frequency noise has to be filtered out by using appropriate damping systems. In our setup *in situ* damping mechanisms like viton-damped copper-stacks or springs combined with an eddy-current damping can not be used, because of a breakdown of damping at low temperature and insufficient thermal contact, respectively. Instead, the whole low-frequency damping is situated outside the vacuum system. As shown in Figure 3.3 we use a three stage damping system. The first stage, situated between the floor and the optical table bearing the whole vacuum system, is an active damping system eliminating low-frequency vibrations from the building. The second stage is a passive damping system which separates the vacuum system from the optical table by air cushion. The third damping stage is again a passive damping based on air cushion, which separates the He-cryostat from the rest of the vacuum system. The He cryostat and the rest of the vacuum system are connected with a flexible metal bellow. Furthermore the whole system is placed in a sound proof chamber to avoid acoustic noise.

3.3 The experimental setup at the BESSY-2 synchrotron radiation facility

X-ray Photoelectron Spectroscopy (XPS) and Near Edge X-ray Absorption Fine Structure (NEXAFS) measurements were made at the HE-SGM beamline at the BESSY 2 synchrotron radiation facility in Berlin to gain information on the chemical composition of the structures and the binding geometries of the molecules in respect to the surface.

In XPS-measurements one excites core-level electrons of atoms with monochromatic x-rays. The kinetic energy of the emitted electrons is analyzed and does not only give information on the chemical element but also on the chemical state of the atom. The XP-data for the C 1s and O 1s peak were acquired with beam energies of 400eV and 650ev, respectively, with the pass energy of the analyzer set to 50eV. For quantitative analysis a complete set of XP spectra was acquired in addition with the Al K_α radiation of the laboratory source at a pass energy of 100eV. All spectra are referenced to the Ag $3d_{5/2}$ line at 368.2eV.

In NEXAFS-measurements the absorbed x-ray intensity is measured as a function of x-ray photon energy, requiring a tunable x-ray light source like a synchrotron. Due to an excitation from occupied orbitals to unoccupied molecular orbitals one obtains a fine structure in the absorption behavior, giving information on the bonding environment of the absorbing atom. By using polarized light one can furthermore gain information on the orientation of the chemical bonds, thus of the whole molecule. All NEXAFS-spectra were recorded in the total electron yield (TEY) mode using an electron detector based on a double channel plate. For energy calibration of the NEXAFS-data the photocurrent of a carbon-contaminated gold grid with a characteristic peak at 285eV was recorded simultaneously with each spectrum. This grid is also used as radiation flux monitor. For the NEXAFS experiments the resolution was set to ΔE=0.4eV at 300eV. The C 1s NEXAFS raw data were normalized by a procedure consisting of several steps: First the spectrum recorded for the clean substrate was multiplied with a correction factor to yield equal intensities in the energy range from 272eV to 278eV and then subtracted. The resulting data were then normalized to the photon flux by division through a spectrum obtained for a freshly sputtered sputtered gold sample. Finally the spectra were normalized to yield an intensity difference between 275eV and 325eV (the edge jump) of one.

The UHV-system at the HE-SGM beamline at BESSY 2 consists of an analysis chamber, a preparation chamber and a load lock and is pumped similar to our STM by a three-stage pumping system. The preparation chamber is equipped with standard facilities for sample cleaning, OMBE-sources and e-beam evaporators for sample preparation and pressure gauges. The analysis chamber is equipped with a quadrupole mass spectrometer for residual gas analysis, a twin anode x-ray source and a CLAM2 energy analyzer. Sample transfer between preparation chamber and analysis chamber is done by a magnetic transfer line whereas sample positioning in the preparation and analysis chamber is done by two manipulators. The sample can be cooled to 100K and heated to 1000K in the manipulators.

3.4 Sample Preparation

Our experiments are performed on single crystal samples supplied by MaTeck, with a surface diameter of approximately 8mm and an orientational misfit of smaller than 0.1° with respect to the perfect (100) and (111) orientations. The samples are cleaned *in situ* under UHV-conditions by repeated cycles of sputtering and subsequent annealing. The samples are sputtered for typically 20min with 500eV Ar^+ ions under an incidence angle of 45° and a flux of $\sim 1\mu A/cm^2$. The annealing is performed at temperatures of ~830K at a pressure lower 5×10^{-9}mbar. Samples exposed to air or new samples are typically cleaned with 10 cycles, whereas samples already in use are cleaned with 3 cycles. This preparation results in atomically clean and flat samples with terrace widths larger than 100nm. An impurity coverage smaller than ~0.05% is observed with STM and STS. Similar procedures are made for the sample preparation at the BESSY 2 synchrotron radiation facility in Berlin.

After sample cleaning, the molecules are deposited *in situ* by sublimation of the molecules. This is done using a home-built Organic Molecular Beam Epitaxy (OMBE) source. The molecules are solids at room temperature with a very low vapor pressure, which can be raised significantly by increasing the temperature. In the OMBE sources the molecules in powder form are contained in an inert, resistively heated glass crucible. After the OMBE-source is in thermal equilibrium at the chosen sublimation temperature, the shutter between sample and crucible is opened and the sample therefore exposed to a molecular flux. Typical deposition rates are in the range of one monolayer (ML) in several minutes. A monolayer is in this work always defined as the surface is fully covered by flat-lying molecules. During deposition the pressure in the preparation chamber does not exceed 5×10^{-9}mbar and no fragmentation of the molecules can be observed at the moderate sublimation applied in our experiments. Metal atoms are deposited by using an electron beam evaporator (EFM 3 from Omicron). The calibration of the deposition flux is done estimating the area covered by metal-islands and typical deposition rates are 1 monolayer per hour. After preparation the sample is transferred into the STM and cooled to 5K for measurement.

Chapter 4

Experimental methods

4.1 Theory of Scanning Tunneling Microscopy STM

STM is a technique closely related to the electron tunneling measurements used by Giaever [54]. Due to the wave nature of the electrons the amplitude of the wave function of an electron does not end abruptly at the surface but decays exponentially into the vacuum, like an evanescent wave of totally reflected light in optics. When a second substance is brought into close vicinity of the tip, the wave function reaches into the second metal, giving rise to a finite transmission probability of the electron to the second metal. This transition across a classically forbidden region is known as the *tunneling effect*. Upon applying a potential difference U between the two metals a tunneling current I flows, with an exponential dependence on the distance between the two electrodes. In both methods this tunneling current I between two separated electrodes biased with a voltage U is measured. As the current I flowing between this two electrodes not only depends strongly on the distance between the electrodes but also on the local density of states of the electrodes, I is providing information on the electronic structure of the surfaces of the electrodes. In the tunnel junction experiments planar electrodes are used, separated by an oxide layer. Obviously, this tunneling experiments are integrating methods, as no spatial resolution can be achieved. The outstanding advancement of the STM is that the electrodes are now separated by a vacuum gap (although also insulating gaseous or liquid gaps are widely applied) and one electrode is tip-shaped on a microscopical length scale and can be positioned relative to the second, planar electrode. This setup offers the possibility of locally resolved electron tunneling experiments. Because of the exponential dependence of the tunneling current on the tip-sample distance the current flows highly localized through a few atoms at the apex of the tip, causing the high spatial resolution of the STM.

Fundament of a detailed understanding of the STM is the first-order perturbation theory, using *Fermi's golden rule* [55]:

$$I(U) = \frac{2\pi e}{\hbar} \sum_{s,t} |\mathbf{M}_{s,t}|^2 \times \delta(E_t + U - E_s) \\ \times (f(E_s)[1 - f(E_t)] - f(E_t)[1 - f(E_s)]) \tag{4.1}$$

where the summation goes over all unperturbed quantum levels of the sample s with energy E_s and of the tip t with energy E_t. U is the potential difference between sample and tip. The Fermi-Dirac distributions f, at the sample and tip temperature T, are ensuring that only tunneling from occupied to unoccupied electron levels occur. The delta-function δ assures that the energy of the tunneling electrons is conserved (This limits the theory to elastic tunneling). According to Bardeen [56], the probability of transition from level t to level s is given by the tunneling matrix element $\mathbf{M}_{s,t}$

$$\mathbf{M}_{s,t} = -\frac{\hbar^2}{2m_e} \int_{\Sigma} d\mathbf{S}(\psi_t^* \nabla \psi_s - \psi_s \nabla \psi_t^*) \tag{4.2}$$

with the wave functions of the unperturbed sample ψ_s and tip ψ_t levels and the integral running over an arbitrary surface Σ within the tunneling barrier region. $\mathbf{M}_{s,t}$ depends on the overlap of the two wave functions, i.e. roughly exponential on the barrier width z_t as well as on the electron momentum perpendicular to the surface.

This expression for the tunneling current I in Equation 4.1 can be simplified by assuming a step-like behavior of the Fermi-Dirac distribution, which is in principle correct at a temperature of 0K and a good approximation at low temperature. Equation 4.1 then simplifies to

$$I(U) = \frac{2\pi e^2 U}{\hbar} \sum_{s,t} |\mathbf{M}_{s,t}|^2 \times \delta(E_s - E_F) \times (E_t - E_F) \tag{4.3}$$

where we have introduced the Fermi energy E_F.

To evaluate $\mathbf{M}_{s,t}$, Tersoff and Hamann made the assumption that the tip wave functions are s-orbitals [55]. The sum of the absolute squares of the wave-functions yields the local density of states (LDOS) of the sample ρ_s and the LDOS of the tip ρ_t at the position (x, y). This allows to write Equation 4.3 in the following form

$$I(U) \propto \int_0^{eU} \rho_s(E, x, y) \times \rho_t(E - eU) \times \mathcal{T}(E, U, z) dE \tag{4.4}$$

where the Fermi level is at E_F=0V and $\mathcal{T}$ is the transition matrix describing the tunneling probability. The tunneling current $I(U)$ depends in this model on the density of states of the tip at the applied voltage U, on the density of states of the surface at the Fermi-level and on the transition matrix $\mathcal{T}$. Making the approximations that the tunneling is purely vertical and disregarding all surface contributions other than of s- or p_z-symmetry, one can write $\mathcal{T}$ in the following form [57]

$$\mathcal{T}(E,U,z) = e^{\left(-2z\times\sqrt{\frac{m_e}{\hbar^2}\times(W_s+W_t-2E+eU)}\right)} \tag{4.5}$$

Equation 4.5 can be further simplified to the final result of this approach to calculate the tunneling current I by assuming $-2E+eU \lll W_s+W_T$ what allows to put $\mathcal{T}$ in front of the integral. Equation 4.4 can therefore be written as:

$$\begin{aligned} I(U) &\propto e^{-2\kappa z}\int\limits_0^{eU} \rho_s(E,x,y)\times\rho_t(E-eU)dE && (4.6) \\ \kappa &= \sqrt{\frac{m_e}{\hbar^2}\times(W_s+W_t)} && (4.7) \end{aligned}$$

Equation 4.6 is the final result for the Tersoff-Hamann approach for the tunnel current I in Scanning Tunneling Microscopy. As one can see, Equation 4.6 consists of two parts: an exponential factor describing the dependence of the tunnel current on the tip-sample distance (the *topographic* information) and an integral factor describing the dependence of the tunneling current from the LDOS of sample and tip. It is therefore obvious, that Scanning Tunneling Microscopy not only shows topographic information of the surface, but also reflects the electronic configurations of the sample-tip system.

Scanning Tunneling Microscopy can be performed in two ways: in the constant-height mode and the constant-current mode. In the constant-height mode one keeps the sample-tip distance constant during scanning with the tip over the sample, which allows extreme fast scanning on flat surfaces. One obtains a map of the varying tunneling current, which rarely allows a quantitative analysis of the surface structure using Equation 4.6. More common and always applied within this work is the constant-current mode. Here the tunneling current is kept constant by varying the sample-tip distance during scanning, the recorded signal is the sample-tip distance. According to Equation 4.6 this image reflects a map of constant LDOS and hence of the electronic structure rather than the geometrical structure.

In Scanning Tunneling Spectroscopy, one can directly evaluate the sample LDOS at the position (x,y) as a function of energy. The tip is kept at the position (x, y) and a sample-tip distance z. The bias voltage V is ramped while recording the tunneling current I and the differential conductance $\frac{\mathrm{d}I}{\mathrm{d}V}$ (the differential conductance was acquired using the *lock-in* technique, which will be described in the experimental setup). The differential conductance can be calculated by taking the derivative of Equation 4.6:

$$\frac{\mathrm{d}I}{\mathrm{d}U} \propto \left(\left[-\int_{0}^{eU} \rho_s(E) \frac{\mathrm{d}\rho_t}{\mathrm{d}E}(E - eU)\mathrm{d}E \right] + \rho_s(eU)\rho_t(0) \right) \tag{4.8}$$

It is typical to assume that the tip-DOS is not depending on the voltage. Then the integral in Equation 4.8 vanishes and one obtains for the differential conductance

$$\frac{\mathrm{d}I}{\mathrm{d}U} \propto \rho_s(eU)\rho_t(0) \tag{4.9}$$

Equation 4.9 states that the $\frac{\mathrm{d}I}{\mathrm{d}U}$-signal is proportional the sample LDOS at the bias voltage U.

4.2 X-ray Photoelectron Spectroscopy XPS

Photoelectron spectroscopy measurements are based on the photoelectric effect: A sample exposed to light with sufficiently small wavelength and thus high energy emits electrons. The number of photoelectrons depends on the intensity of the light and their energy on the wavelength of the photons [58]. One usually probes core-level electrons of the atom with X-rays and valence electrons with Ultra-Violet (UV) light. X-ray Photoelectron Spectroscopy (XPS) was developed in the 1950‘s by Siegbahn et al. and is nowadays among the most frequently used techniques in surface science, yielding information like chemical composition or oxidation state of the elements in a large variety of materials like metals, oxides, polymers and even biological samples. Monochromatic photons with energy $h\nu$ are absorbed by the atoms in a solid, a liquid or a molecule, resulting in the ionization of the atom and the emission of core (inner shell) electrons. XPS is an integrating technique, as the signal is averaged over a relatively large area of the sample. In XPS, one measures the intensity of the emitted photoelectrons $N(E)$ as a function of their kinetic energy. The XPS-spectrum is however usually a plot of $N(E)$ versus the binding energy BE. The kinetic energy of the emitted photoelectrons is

$$E_{kin} = h\nu - BE - \phi \tag{4.10}$$

where E_{kin} is the kinetic energy of the photoelectrons, h the Planck-constant, ν the frequency of the exciting radiation, E_b the binding energy of the photoelectron with respect to the Fermi level of the sample and ϕ is the work function of the spectrometer. Although X-rays can penetrate metals easily several micrometer, XPS is a surface sensitive method due to small mean free path of the generated photoelectrons, which is energy dependent and in the energy range from 15eV to 1keV the mean free path is in the range of 1nm to 2nm [59]. The inelastically scattered photoelectrons form a background in the acquired spectrum which is usually corrected by subtracting a linear or a Shirley background [60]. In addition to the expected photoelectron peaks the XPS-spectra also show peaks related to Auger electrons. These arise from the deexcitation of the photo ion by an Auger transition. Auger electrons have fixed kinetic energies which are independent on the X-ray energy. Therefore Auger peaks can be recognized by recording the same spectrum at two different x-ray energies: XPS peaks will have the same binding energies whereas Auger peaks will shift on the binding energy scale. Furthermore one can observe additional peaks related to shake-up, shake-off and plasmon loss processes. Shake-up and shake-off losses arise when the photoelectron imparts energy to another electron of the atom, lifting this electron to a higher unoccupied state (shake-up) or to an unbound state (shake-off), therefore loosing energy and appearing at higher binding energy. The observed binding energies are not only depending on the element but contains also chemical information. The energy levels of the core electrons depend slightly on the the chemical state of the atom, with typical chemical shifts of the binding energy of up to 3eV. As a rule of thumb, one can say that the binding energy is increased with increasing oxidation state and for a fixed oxidation state with the electronegativity of the ligands [61]. The elements and their chemical states are usually identified by comparing the measured peak positions to known species reported in literature [62]. XPS cannot only be used to identify the elements and their chemical states within a sample, but also their concentrations assuming a structure model. The general expression for the intensity of an XPS peak is

$$I = F_X S(E_k)\sigma(E_k)\int\limits_0^\infty n(z)e^{-\frac{z}{\lambda(E_k)\cos\theta}}\mathrm{d}z \tag{4.11}$$

with I being the intensity (area) of the XPS peak, F_X the x-ray flux on the sample, $S(E_k)$ the spectrometer efficiency for detecting electrons at a kinetic energy E_k, $\sigma(E_k)$ is the cross section for photoemission, $n(z)$ is the concentration of the element, z is the depth below the surface, $\lambda(E_k)$ is the mean free path at the kinetic energy E_k and θ is the angle between emission direction of the photoelectron and the surface normal. In case of a homogeneous sample Equation 4.11 can be simplified to

$$I = F_X S(E_k)\sigma(E_k) n \lambda(E_k) \cos\theta \tag{4.12}$$

Equation 4.12 can be simplified further if one assumes that the spectrometer efficiency $S(E_k)$, the cross section for photoemission $\sigma(E_k)$ and the mean free path $\lambda(E_k)$ are element and energy independent. One then obtains that the ratio between the intensities of two peaks is the ratio between the two concentrations:

$$\frac{I_a}{I_b} = \frac{n_a}{n_b} \tag{4.13}$$

For a detailed explanation of XPS see [61] and the references therein.

4.3 Near Edge X-ray Absorption Fine Structure NEXAFS

In X-ray Absorption Spectroscopy and the more specific Near Edge X-ray Absorption Fine Structure the absorbed X-ray intensity is measured as a function of the energy of the incident X-ray photons. The second method refers to the absorption behavior around an absorption edge in a narrow energy range of typically 50meV, in which large variations of the absorption coefficient and intense and narrow resonances can be observed. As the X-ray energy has to be altered one needs a tunable light source, what can be provided by an synchrotron radiation facility. A synchrotron radiation facility not only offers a wide range tunable light source, but also high intensity and brilliance, enabling absorption experiments with submonolayer sensitivity.

The fine structure of the absorption coefficient has its fundament in the excitation from occupied into unoccupied molecular orbitals. Obviously the measurement is very sensitive to bonding environment of the absorbing atoms and by comparing measured spectra with reference lines one can identify the local bonding environment of the chemical species. The spectra not only exhibit chemical shifts for different chemical states, comparable to XPS, but furthermore a fine structure rendering the local bonding environment. NEXAFS-spectra are also dependent on the polarization of the used X-rays. In systems with oriented bonds one can use linear polarized X-rays to probe the direction of the chemical bonds. Especially in the case of aromatic molecules one can use the unoccupied molecular orbitals with π and σ symmetry to obtain information on the orientation of the molecule as they are oriented in and out of the benzene ring plane.

A detailed description of NEXAFS can be found in [63].

Chapter 5

Hydrogen bonded supramolecular systems at metal surfaces

One way to fabricate materials with specific structures and properties is the *bottom-up* approach, which is the formation of specific structures out of individual atomic or molecular entities. The arrangement of the single building blocks can be accomplished by manipulation on the atomic level, as shown by Crommie et al. when forming quantum corrals out of individual Fe-atoms [25], but this is a very time consuming process. A method which provides appealing opportunities for fast engineering of low-dimensional nanostructures is supramolecular self-assembly of molecular building blocks on well-defined substrates [10]. Ideally, as realized in nature, reversible non-covalent bonds mediate the controlled assembly and hierarchical growth of fully integrated systems [64, 65, 66]. Understanding how the molecular components self-arrange via non-covalent interactions is a key step for the realization of molecular devices by *bottom-up* construction [67]. Control of the self-assembly process of functionalized molecules in two-dimensions on solid surfaces may open the way for applications such as organic network templates, molecular electronics or molecular motors. Some of the molecules widely employed for self-assembly studies have functional groups which enable hydrogen bonding between the molecules. Carboxylic acid groups are especially important because of their ability to form self-complementary dimer synthons, i.e. the pairing of directed $\mathrm{OH}\cdots\mathrm{O}$ hydrogen bonds as shown in Figure 5.1, which enhance the strength of the hydrogen bonding considerably [18, 68].

A crucial requirement in the stability of these structures is the integrity of the carboxylic groups acting as linkers between the adsorbed molecules. It has been shown that carboxylic groups can undergo deprotonation upon

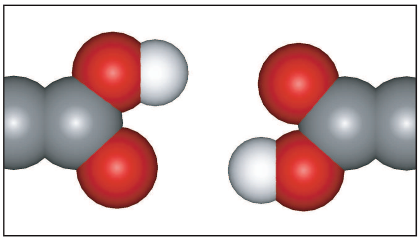

Figure 5.1: Sketch of a hydrogen-bonded carboxylic acid dimer. (Grey – Carbon, Red – Oxygen, White – Hydrogen)

adsorption on metal surfaces, producing carboxylate functions [69, 70, 71, 72, 73, 74, 75, 76]. This process destabilizes the dimer synthons and introduces new possibilities of intermolecular interactions. If the carboxylate groups stay charged upon adsorption onto a surface this would enable the formation of stronger intermolecular ionic hydrogen bonds. This is a special class of hydrogen bond that forms between an ionic donor (acceptor) and a neutral acceptor (donor) and has a bond strength up to a third of the strength of a covalent bond [19, 77]. The ionic hydrogen bond represents a new type of motif-controlling functional elements to assemble supramolecular structures at surfaces under solvent-free conditions.

To understand the role of ionic hydrogen bonds in the supramolecular assembly process we studied two similar molecules on a metal surface as model systems. Each molecule consists of a benzene ring backbone and carboxylic acid groups as endfunctions. The molecules we investigated were 1,3,5-benzenetricarboxylic acid (Trimesic acid - TMA) and 4,4′,4″-benzene-1,3,5-triyl-tri-benzoic acid (BTA), a derivative of TMA (Figure 5.2). TMA and its derivates represent prototype systems for the formation of two-dimensional networks on surfaces. It is known that TMA molecules form an open honeycomb structure on highly ordered pyrolytic graphite (HOPG) under vacuum conditions. This structure can be modulated by the addition of alkyl chains alcohols [78, 79]. TMA on either Cu(100) or Ag(111) forms open honeycomb networks at temperatures below 280K [76, 80]. On the Cu(100) surface an irreversible phase transformation from the open honeycomb network to a dense-packed striped array can be observed at 300K. In solutions under strong acidic conditions TMA forms two-dimensional networks on Au(111), with the structure depending on the electric potential [81, 82].

TMA was studied extensively by scanning tunneling microscopy (STM), scanning tunneling spectroscopy (STS), X-ray photoelectron spectroscopy (XPS) and near edge X-ray absorption fine structure (NEXAFS) measurements, which were compared to molecular dynamics calculations. Emphasis

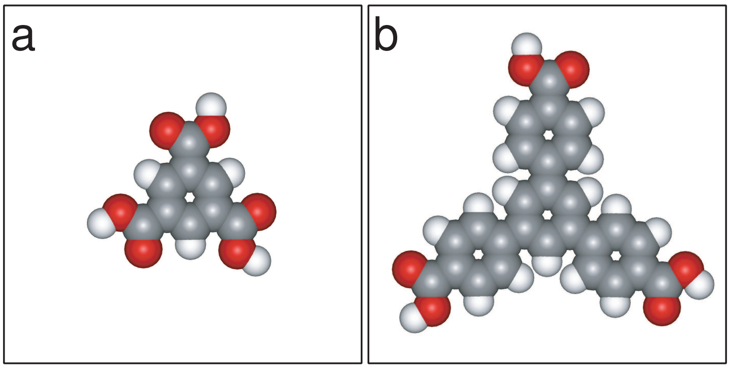

Figure 5.2: **a** Molecular structure of TMA (1,3,5-benzenetricarboxylic acid) **b** Molecular structure of BTA (4,4′,4″-benzene-1,3,5-triyl-tri-benzoic acid).

was placed on the investigation of the purely hydrogen bonded structure and the structure containing carboxylate groups. TMA forms irregular islands after annealing with a temperature below 200K. In the range of 250K-340K, a structure mediated by neutral hydrogen bonds is observed and after annealing at 420K an irreversible deprotonation of one out of the three carboxylic groups per TMA molecule can be identified. This deprotonation results in an irreversible structural transformation to a densely packed phase which was shown to be stabilized by ionic hydrogen bonds between the remaining carboxylic functions and the deprotonated carboxylate functions.

Investigations on BTA were made by STM- and STS-measurements, which were again combined with molecular dynamics calculations. BTA shows a more elaborate behavior due to its more complex structure, forming three different structures. Up to annealing temperatures of 300K, a structure mediated by hydrogen bonds between the carboxylic groups is formed. After annealing to temperatures in the range of 320K-400K an irreversible phase transition occurs, resulting in the formation of one carboxylate group per molecule. Further increase of the temperature above 420K induces a second irreversible phase transition into a structure of molecules with two carboxylate groups.

In both the TMA- and the BTA systems the ionic hydrogen bonds effectively overcome the Coulomb repulsion between the charged species, stabilizing the systems. To our knowledge it is the first time that the ionic hydrogen bond and its role in supramolecular organization in solvent free ”dry” ultra-high vacuum conditions is addressed.

5.1 1,3,5-benzenetricarboxylic acid on Ag(111)

The Ag (111)-surface was cleaned by repeated cycles of sputtering with 500eV Ar^+ - ions and subsequent annealing to ∼800K. Commercially available TMA-molecules (Aldrich, purity ∼95%) in powder form were deposited by sublimation onto the Ag (111)-surface with the crucible containing the TMA-molecules held at a temperature of 473K during deposition. The Ag(111) substrate was kept at a temperature of ∼100K during deposition, followed by an annealing in the temperature range from 100K to 420K. The coverage was always in the submonolayer range, typically a quarter to a third of the surface was covered by TMA-molecules.

STM and STS data were acquired at a temperature of 5K. ST-spectra were recorded using with the lock-in amplifier set to a frequency of 5kHz and a modulation-amplitude of 10mV. The cleanness of the tip was checked by acquiring ST-spectra on the clean Ag (111) surface (Figure 5.5), which showed the typical onset of the two-dimensional surface state at an energy E_0 of -70.9±5.3meV and a width of 10.6±8.4meV [83, 84, 85]. The energy and the width of the surface state onset were obtained by taking the derivative of the dI/dV-signal and the maximum and the Full Width at Half Maximum (FWHM) of the so obtained peaks were allocated to the energy and width of the surface state onset. The XP-spectra were referenced to the Ag $3d_{5/2}$-line at 368.2eV and were fitted after a linear background substraction with a suitable number of Gaussian-shaped peaks, linked to carbon and oxygen atoms in different states within the structures. Consulting literature [75, 86, 87, 88, 89, 90, 91], these peaks could be allocated to the different states of carbon and oxygen in the TMA-molecules and the areas of the peaks were used as a measure for the amount of atoms within these states. All NEXAFS spectra were recorded in the total electron yield mode using a double channel plate as electron detector. For the methods used for energy-calibration of normalization of the spectra see [75].

In the theoretical investigations, performed in collaboration by Alessandro De Vita (King's College London), a combination of *ab initio* and classical molecular dynamics calculations was used. The electronic densities resulting from first principle calculations were used to determine a classical potential with effective partial point charges positioned on the the atom cores. These charges were used in two-dimensional classical molecular dynamics annealing runs with the molecules treated as rigid bodies to find the energetically most stable structure, which reproduces the 420K-structure. For details of the calculations see [93].

Figure 5.3 shows an STM-topograph of the TMA-structure after annealing the sample to 300K. The molecules are aggregated into the well known

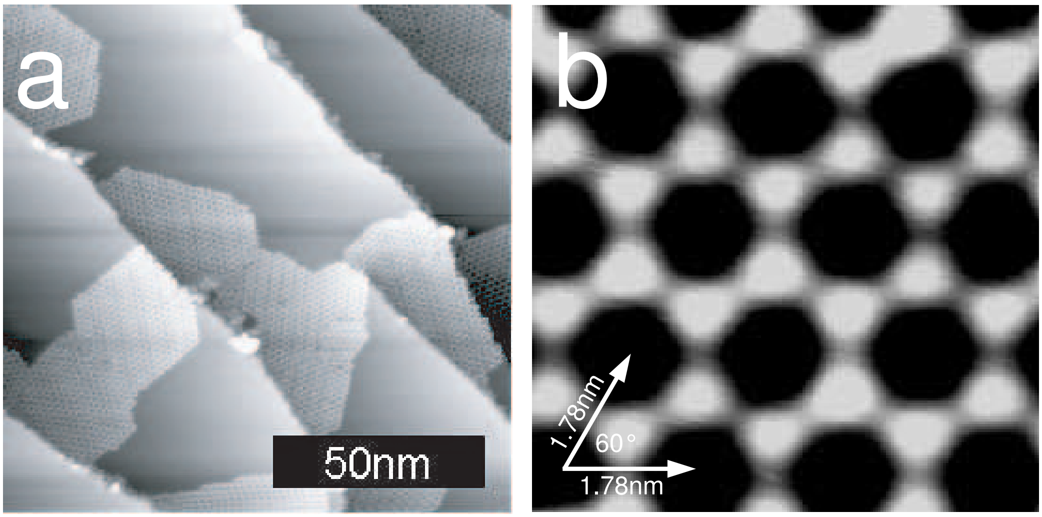

Figure 5.3: **a** STM-topograph of TMA on Ag(111) after annealing at 300K. The TMA-molecules form the well-investigated *honeycomb-structure*. **b** The TMA *honeycomb-structure* shows a lattice constant of 1.78nm and the estimated O···O distance in the hydrogen bonds of 0.34nm is in agreement with previous measurements. The molecules appear triangular, indicating flat lying molecules. (U=500mV, I=500pA, T=5K)

honeycomb structure where every molecule is connected to three neighboring molecules via carboxylic-acid dimer synthons between the carboxylic groups. This gives a hexagonal lattice with a lattice constant of 1.78nm and the O···O distance in the hydrogen bonds of 0.34nm is in agreement with previous results obtained with TMA on other substrates [76, 78, 81, 82]. Attempts to determine the registration of the honeycomb structure with respect to the Ag(111) surface were not successful because we could not resolve the Ag(111) atomic lattice and the *honeycomb structure* simultaneously. The large number of different angles between various orientated domains could not be explained by tentative models based on the lattice constants of the TMA *honeycomb structure* and the Ag(111) surface, suggesting that the *honeycomb structure* is non-commensurate to the Ag(111) substrate.

ST-spectra acquired on the 300K-structure still show a surface state formed by a two-dimensional electron gas, but the onset is shifted to -9.7±9.8meV and is broadened to 17.1±20.5meV (Figure 5.5) with the flat plateau extending above 1500meV. Because there is no significant difference between ST-spectra taken at different positions of the TMA-honeycomb structure, we can rule out that the onset is a signature of TMA molecular orbitals. We attribute this onset to the surface state formed by a two-

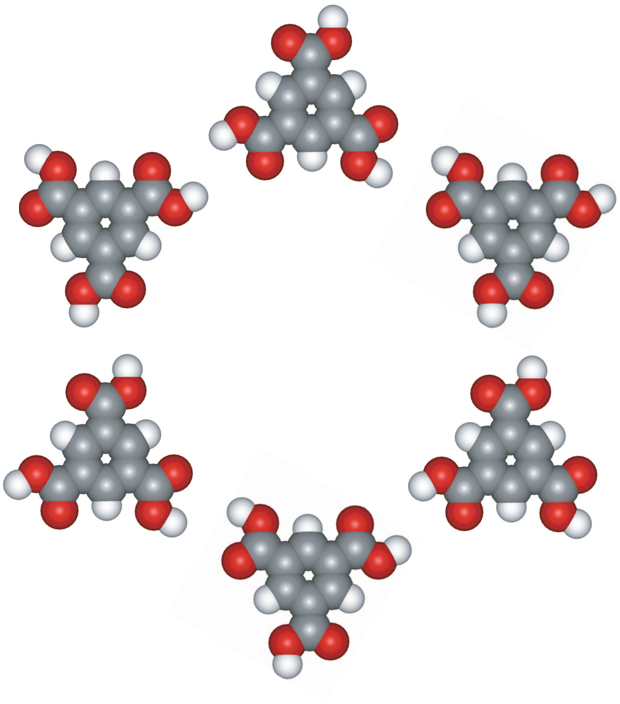

Figure 5.4: Model of the TMA-*honeycomb structure*. Every TMA-molecule is connected to three neighboring molecules via carboxylic acid dimer synthons between the carboxylic groups.

dimensional electron gas, but shifted to higher energy and broadened by the weakly adsorbed TMA-molecules. It has been reported that weakly adsorbed noble gas atoms have similar effects on the surface state of (111) surfaces of noble metals [94, 95, 96]. We propose that TMA weakly binds to the Ag surface, presumably van der Waals type like in the case of noble gas adsorption. This assumption is in agreement with the generally accepted picture that planar aromatic hydrocarbons are weakly π-bonded with the benzene rings parallel to the metal substrate [97, 98].

XPS- and NEXAFS-measurements provided complementary insight into the chemical states and the bonding geometry of the TMA-molecules in the 300K structure, endorsing the picture obtained by the STM-measurements.

Figure 5.6a shows the C 1s XPS-signal of the 300K structure and Figure 5.6b shows the O 1s XPS-signal of the 300K structure. In the C 1s spectrum two well separated peaks are identified, a larger one at a binding energy (BE) of 285.0eV which is assigned to the 6 carbon-atoms in benzene rings and a smaller one at a BE of 289.1eV which is assigned to the 3 carbons in the carboxyl groups in accordance with previous reports [75, 86, 86, 87, 88, 89,

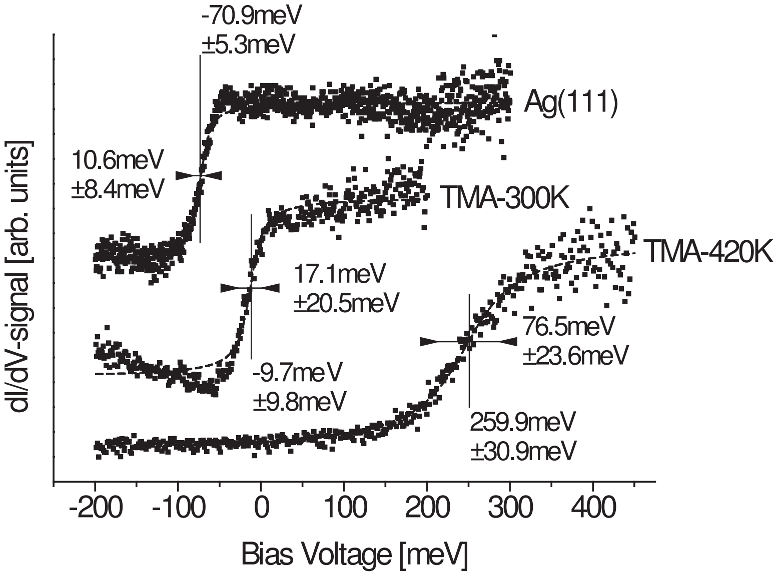

Figure 5.5: Tunneling spectra made on clean Ag(111), on Ag(111) covered with TMA *honeycomb-structure* after annealing to 300K and on Ag(111) covered with TMA-quartets, after annealing to 420K. As a shift of the onset of the surface state to higher energy indicates a negatively charged layer and a shift to lower energy indicates a positively charged layer, we conclude that the TMA *quartet structure* is negatively charged.

90, 91]. The fit of the spectrum with Gaussian-shaped peaks with a full width at half maximum (FWHM) of 1.4eV is improved by adding a small additional peak at a BE of 287.3eV, which is assigned to a small amount of the carboxylic groups of TMA-molecule being deprotonated and thus forming carboxylate groups. The O 1s signal consists of a broad symmetric peak which is a convolution of the signals of oxygens in hydroxyl groups (BE of 533.6eV) and in carbonyl groups (BE of 531.5eV), in accordance to similar systems bound by hydrogen bonds between carboxylic acid groups [75, 87, 88, 89]. The C 1s and O 1s XP spectra clearly show that after annealing to 300K the carboxylic groups of the TMA molecules were still mostly protonated, forming dimerised hydrogen bonds between carboxylic groups.

NEXAFS-spectra of the 300K *honeycomb structure* are displayed in Figure 5.7 where several pronounced $\pi^\star$-resonances are clearly discernible. The $\pi^\star$-resonance at 284.6eV is assigned to transitions related to the carbon atoms of the benzene-ring, whereas the prominent peak at 288.2eV and the shoulder at 290.0eV are assigned to transitions related to the carboxyl carbons. Both the $\pi^\star$-resonances of the benzene carbons and of the carboxyl carbons

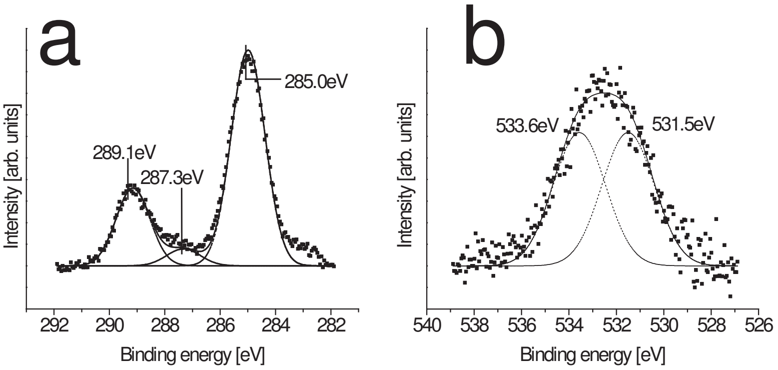

Figure 5.6: XPS-data of the TMA *honeycomb-structure* on Ag(111) at 300K. **a** C 1s spectrum. The larger peak can be assigned to carbon in the benzene ring and the smaller peak to carbon in carboxylic groups. The minor peak might be due to carbon in different states or impurities. **b** O 1s spectrum. The broad symmetric peak is a convolution of the signals of oxygen in hydroxyl groups and in carbonyl groups. Both the C 1s and the O 1s signal indicate intact TMA-molecules, forming dimerized hydrogen bonds between carboxylic groups.

show a pronounced dichroism with almost completely vanishing intensity for normal photon incidence (90°) The average tilt angles calculated from the observed dichroism are 18°±7° and 20°±7° for the benzene and carboxyl part of the molecule, respectively. These data indicate that the carboxylic acid groups are coplanar with the benzene rings. There is a significant deviation of the obtained average tilt angle from 0° expected for perfectly flat lying molecules. Rather frequently average tilt angles significantly different from zero, i.e. up to 10°, are observed in NEXAFS spectroscopy even for perfectly flat lying aromatic molecules on metal surfaces [99, 100, 101]. The tilting has been attributed to adsorption-induced aplanar intramolecular distortions, involving a bent of the CH-bonds out of the ring plane. Therefore a plausible explanation of the data is that the vast majority of the TMA-molecules is indeed adsorbed in a flat geometry and the larger average tilt angle is caused by a small number of molecules deviating significantly from a flat adsorption geometry. These latter molecules can be adsorbed at defects or step edges or even in a second layer. For a detailed analysis of the NEXAFS-data see [93].

When depositing the TMA-molecules at a Ag(111) surface held at a temperature of 420K or after annealing the *honeycomb structure* to 420K the open TMA *honeycomb-structure* transforms irreversibly to a dense-packed structure as shown in the STM-picture in Figure 5.8. The basic motif of this

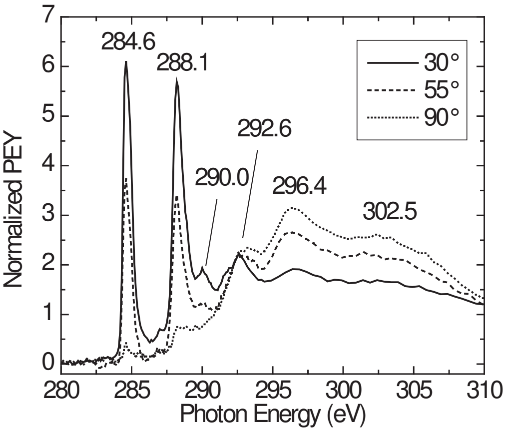

Figure 5.7: NEXAFS-data of the TMA *honeycomb-structure* on Ag(111) at 300K. The NEXAFS-data reveal almost flat-lying TMA-molecules, with the carboxylic acid groups being coplanar to the benzene ring.

structure is a TMA quartet, a group of four closely packed TMA molecules in a rhomboedric arrangement with a side-length of 0.9nm and an angle of 68.4°. These quartet units repeat in a oblique lattice with lattice-constants of 1.87nm, 1.77nm and an angle of 102°. Similar to the 300K structure the registration of the 420K structure with respect to the Ag(111) substrate could not be determined. No tentative model of the 420K structures based on the lattice constants of the 420K structure and the Ag(111) surface is given, as none of these models reproduced the structure better than the others.

ST-spectra acquired on the 420K structure (Figure 5.5) reveal marked changes in the surface electronic structure, implying a remarkable impact of the TMA-quartets on the surface electronic state compared to the neutral adsorbates in the 300K structure. The spectra show a broad onset around 259.9±30.9meV with a width of 76.5±23.6meV. As no significant difference between various spots of the structure could be seen, we attribute the onset feature in the ST-spectra to the surface electronic state. It is known that an excess negative charge at the surface associated with the adsorption usually results in an upward shift of the onset energy [94, 95, 102, 103, 104], whereas a downward shift is observed for electropositive adsorbates like alkali metals [105, 106]. The observed upward shift of the onset energy of the surface state can therefore be associated with the 420K structure being negatively charged.

An analysis of XPS-measurements on the dense-packed 420K structure showed a rigorous change in the chemical states of the TMA-molecules. The C 1s signal of the 420K-structure as shown in Figure 5.9a still consisted of two

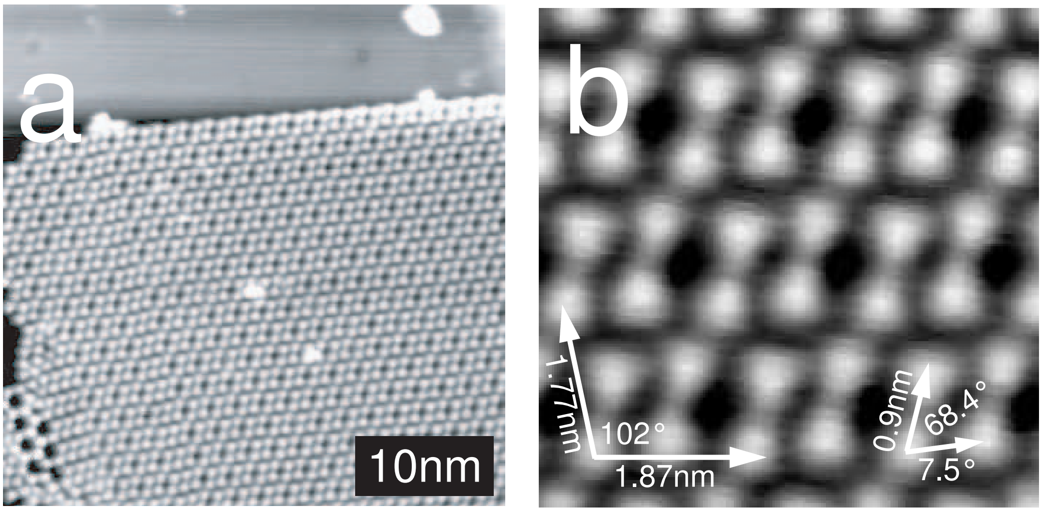

Figure 5.8: **a** STM-topograph of TMA on Ag(111) after annealing with 420K. The TMA-molecules form a *quartet-structure*. **b** The TMA *quartet-structure* shows a unit cell with oblique lattice with lattice constants of 1.87nm, 1.77nm and an angle of 102°. The molecules appear triangular, indicating flat lying molecules. (U=500mV, I=500pA, T=5K)

peaks, but the smaller one at a BE of ∼289eV was broadened compared to the adequate peak in the 300K-structure. The C 1s signal was fitted by three Gaussian-shaped peaks with a FWHM of 1.4eV and the so obtained binding energies were compared with the results of the 300K-structure and literature. Doing this, the smaller peak could be deconvoluted into two peaks, one for carbon in carboxylic group at a BE of 288.7eV, in good agreement with the 300K-structure, and one for carbon in a new state at a BE of 287.5eV. This new peak can be assigned to carbon in carboxylate groups according to previous measurements [69, 73, 75, 86, 87, 88, 89, 90, 91]. Carbon in the benzene ring was found at a BE of 284.6eV, also in good agreement with the 300K-structure. The peak areas, with the area under the whole spectrum normalized to 9 carbon atoms in the TMA-molecule, were 5.9 for the benzene-peak, 2.1 for the carboxylic peak and 1.0 for the carboxylate peak. The areas of the carboxylic peak and the carboxylate peak sum up to 3 carbon atoms, implying that the carboxylate groups have their origin in the carboxylic groups.

The O 1s signal (Figure 5.9b) became asymmetric after annealing with 420K and could not be fitted anymore with two equal Gaussian-shaped peak. Instead, the signal had to be fitted by two or more nonequivalent Gaussians, clearly showing the formation of oxygen atoms in different chemical states

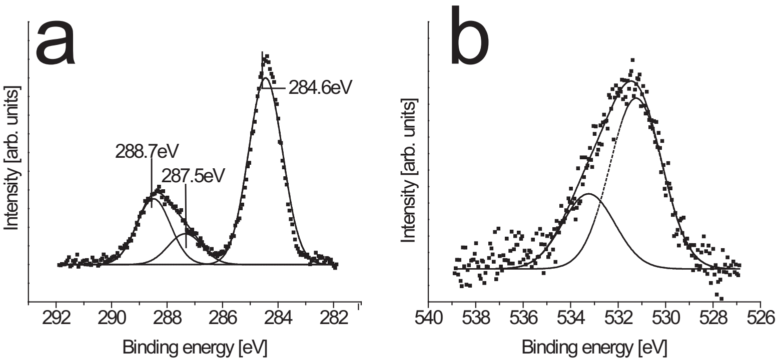

Figure 5.9: XPS- data of the TMA *quartet structure* on Ag(111) after annealing to 420K. **a** C 1s spectrum. The larger peak can be assigned to carbon in the benzene ring and the smaller peak to carbon in carboxylic groups. The third peak can be assigned to carbon in carboxylate groups. **b** O 1s spectrum. The broad peak is asymmetric, showing the formation of oxygen atoms in different chemical states than those found in the purely hydrogen bonded *honeycomb-structure*. Both the C 1s and the O 1s signal indicate the formation of carboxylate groups in the TMA-molecules after annealing to 420K. A detailed analysis showed that one-third of the carboxylic groups were deprotonated, forming carboxylate groups.

in contrast to those found in the purely hydrogen bonded 300K-structure [69, 86, 87, 88, 89]. A quantitative interpretation of the O 1s signal is much more delicate compared to the C 1s signal, because of the large number of different species of oxygen atoms in a complex chemical neighborhood within the 420K-structure and the unknown BE of the different oxygen atoms within the ionic hydrogen bonds. Therefore we refrained from a quantitative analysis of the O 1s signal.

In summary the appearance of new chemical states in the carbon- and oxygen spectra is attributed to the often observed deprotonation of carboxylic acid groups upon adsorption on metal surfaces and the formation of carboxylate groups [70, 72, 74, 76, 107]. Based on the relative peak-areas in the C 1s signal the number of carbon atoms in carboxyl acid groups is 2.1 and in carboxylate groups 1.0. Considering the high symmetry of the structure we conclude that one out of three carboxylic acid groups per molecule is deprotonated and changed into a carboxylate group. This formation of carboxylate groups also explains the negative charge of the 420K structure on Ag(111), as observed by STS.

NEXAFS spectra of the 420K structure are displayed in Figure 5.10.

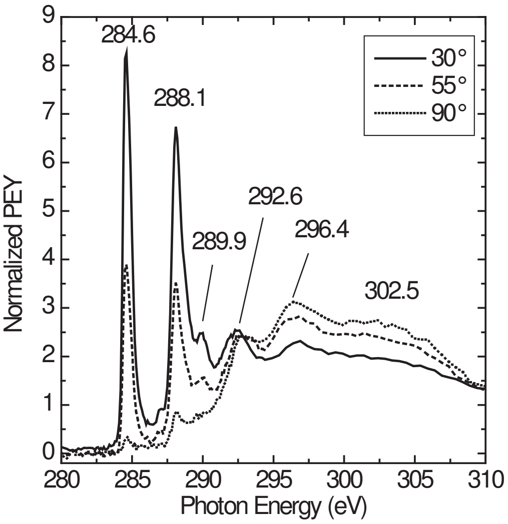

Figure 5.10: NEXAFS-data of TMA honeycomb on Ag(111) at 420K. The NEXAFS-data reveal almost flat-lying TMA-molecules, with the carboxylic acid groups being coplanar to the benzene ring. A tilting of the molecules due to a binding of the oxygens of the carboxylate group to the substrate cannot be observed, in contrast to previous measurements on other systems.

Upon warming to 420K and measuring the sample again at 300K the dichroism of the $\pi^\star$-resonances remains very pronounced.The average tilt angles are now 14°±5° for the benzene ring and 23°±5° for the carboxyl groups. This indicates that the TMA-molecules remain in a essentially flat-lying geometry on the surface. It seems that the carboxylic groups on average are now tilted by 5° to 10° out of the plane of the benzene rings. Comparing the NEXAFS spectra obtained for the 300K *honeycomb phase* and those obtained after annealing with 420K one notices only small differences, in particular, the intensity of the carboxyl $\pi^\star$-resonance is not much reduced relative to the $\pi^\star$-resonance of the benzene ring. These changes are consistent with only a partial deprotonation of the carboxylic acid groups. For complete deprotonation we would expect a much more pronounced decrease of the $\pi^\star$-resonance as has been observed in a related sytem, i.e. TPA on Cu [75]. For a detailed analysis of the NEXAFS-data see [93].

Annealing to temperatures higher than 420K did not result in structures containing more carboxylate groups than the 420K-structure, unquestionably showing that the 420K structure is the most stable structure.

The deprotonation of carboxylic acid groups upon adsorption on metal surfaces has been observed in many other systems but usually the oxygen atoms of the carboxylate groups bind to substrate atoms, tilting the whole molecule to an up-standing configuration [70, 72, 74, 76, 107]. In contrast to these results, our STM, STS- and NEXAFS-measurements for the 420K structure clearly provide evidence for flat lying, negatively charged TMA-molecules containing one carboxylate group. This suggests that the negatively charged carboxylate groups are engaged in lateral intermolecular binding, forming ionic hydrogen bonds between charged carboxylate functions and neutral functions of other TMA-molecules. A fundamental and evident precondition for the formation of ionic hydrogen bonds is of course that the charge is not distributed over the entire molecule or compensated by the metallic substrate.

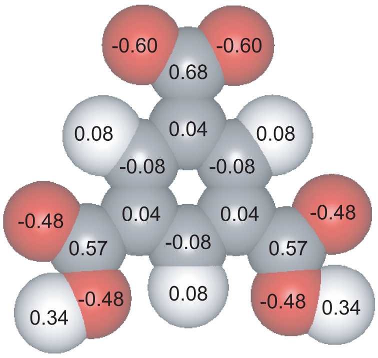

Figure 5.11: Point charges positioned on the cores of the atoms of the deprotonated TMA-molecule, as result of the ab-initio calculation. The total charge of the deprotonated TMA-molecule adsorbed onto the Ag(111) surface is 0.5 electrons, with 0.52 electrons cumulated at the carboxylate group, consistent with the observed shift of the surface state onset.

To gain quantitative information about the charge distribution in the TMA-molecules and within the TMA-structure *ab initio* calculations of a single TMA-molecule possessing one carboxylate group were performed. As a nomenclature, TMA-molecules containing one and only one carboxylate group will be called *deprotonated* subsequently. Subsequently, molecular dynamics calculations were made to reproduce the 420K-structure and to gain a better understanding of the interplay between charged carboxylate groups and neutral species.

In this *ab initio* calculation a single deprotonated TMA-molecule placed on a 5 layer slab of Ag(111), with the temperature of the system set to 0K and taking into account a relaxation of the system, was regarded to investigate its charge upon deprotonation. The so obtained electron densities were used to determine a classical potential according to [108, 109, 110]. As a result of these calculations, effective partial charges concentrated on the cores of the atoms of the TMA-molecules were obtained, shown in Figure 5.11. Overall, these calculations reveal a total charge of the partial deprotonated TMA-molecule of 0.5 electrons and suggest the formation of a residual surface dipole on the Ag(111) substrate after deprotonation, consistent with the observed shift in the ST-spectrum of Figure 5.5 and [94, 102, 103], with a charge of 0.52 electrons cumulated on the carboxylate groups. For details of these calculations see [93].

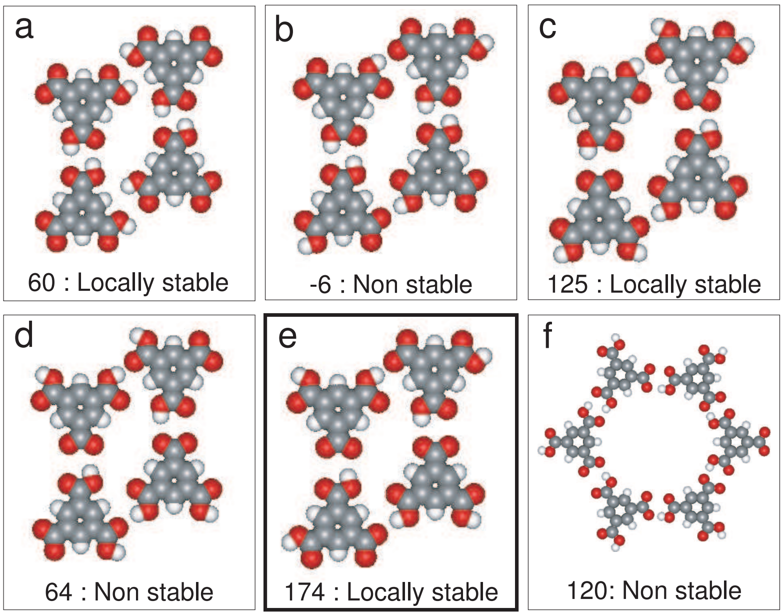

Figure 5.12: **a-e** The different investigated configurations of the quartet unit. As the 420K structure showed a C_2-symmetry, only configurations with a C_2-symmetry were tested. Additionally the calculated interaction energy in arbitrary units and the local stability is given. The interaction energy per molecule calculated with the classical force field is given in units of 10^{-4}a.u. (1a.u.=4.359×10^{-18}J). The structure in **e** is the by far most stable structure. **f** The deprotonated *honeycomb-structure*. Again interaction energy and local stability are given

In a second step we wanted to find out the positions of the carboxylate groups to understand the 420K-structure. Two-dimensional classical molecular dynamics simulated annealing runs were performed, with the TMA-molecules treated as rigid bodies. The interaction between the molecules was modeled by a superimposition of a Coulombic term derived from the charges determined as above and a short range repulsive term, necessary to exclude an overlap of the molecules. Electrostatic screening due to the metal surface was taken into account by introducing mirror images of the partial point charges of the potential [111]. Consistent with the XPS-results and due to the high C_2-symmetry of the structure, we assumed that each TMA-molecule bore one carboxylate group. The stability of every configuration has been calculated by systematically changing the positions of the carboxylate group of each TMA-molecule in the unit cell. Since the 420K-structure showed a C_2-symmetry, we limited the search to configurations possessing this symmetry as shown in Figure 5.12.

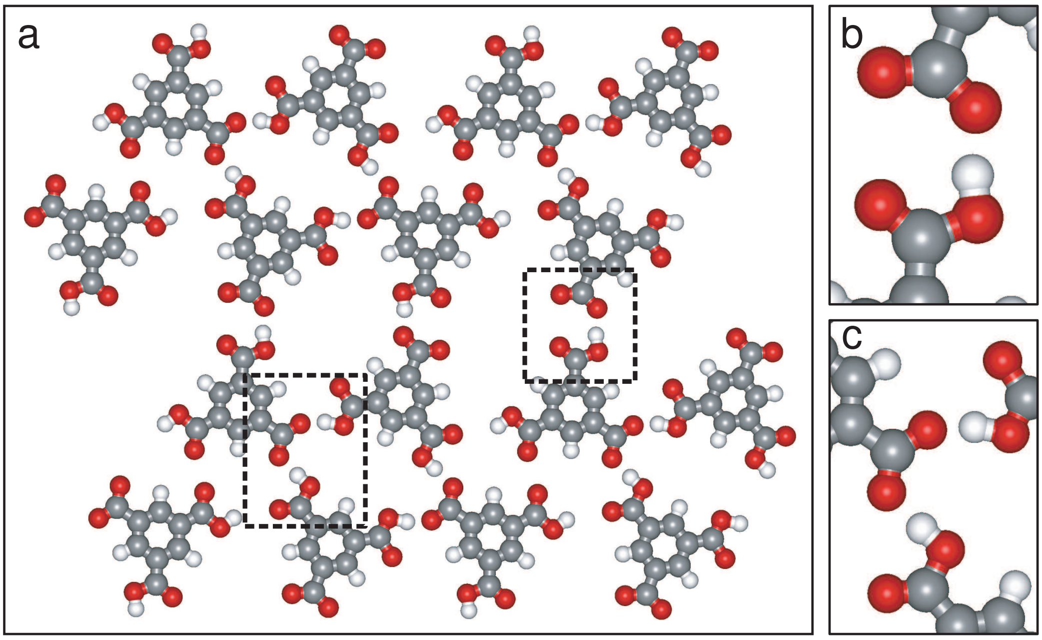

Figure 5.13: **a** Model of the 420K-structure obtained with ab-initio and 2D molecular dynamics calculations. The simulated 420K structure is in good agreement with the STM-topographs of the 420K structure shown in Figure 5.8. The structure contains two different kinds of ionic hydrogen bonds shown in **b** and **c**. **b** Ionic hydrogen bond between one carboxylate group and one carboxylic group. **c** Ionic hydrogen bond between one carboxylate group and two carboxylic groups on different molecules. This binding to two different molecules catenates the dimers in the observed structure. The calculated O···O distance was 0.256nm for both ionic hydrogen bonds.

The final equilibrium structure obtained in this way, shown in Figure 5.13, is in good agreement with the experimentally observed structure. All charged carboxylate groups are bound to neutral carboxylic groups and furthermore two different kinds of carboxylate groups exist within the 420K-structure, highlighted in Figure 5.13a and magnified in Figure 5.13b and 5.13c. Figure 5.13b shows the first kind of ionic hydrogen bond, stabilizing a TMA-dimer, in which the carboxylate group is bound to a single carboxylic group. Figure 5.13c shows the second kind of ionic hydrogen bond, in which the carboxylate group is bound to two carboxylic groups on different molecules. This binding to two different molecules catenates the dimers in the observed structure. The calculated $O \cdots O$ distance was 0.256nm for both ionic hydrogen bonds.

In addition, the protonated and deprotonated honeycomb structure were investigated to understand the mechanism of the structural transformation upon carboxylate group formation. We note that a honeycomb structure formed out of deprotonated TMA-molecules would involve the same overall number of hydrogen bonds observed here (as the overall residual number of hydrogens would be the same in the two structures). However, the hexagonal arrangement would imply couples of adjacent negatively charged and mutually repelling oxygen atoms, located on the non-hydrogen-bonded side of facing carboxylic group pairs. This does not happen in the denser packing experimentally observed, where carboxylic group pairs are never facing each other and can thus be connected by at most one hydrogen bond. As one can see from the interaction energies reported in Figure 5.12, the deprotonated hexagonal phase (*honeycomb-structure*) is significantly less stable than our densely packed model structure. The emerging physical picture is thus one in which the preferred arrangement of the molecules upon deprotonation is determined by the concurrent need of maximizing the number of hydrogen bonds while minimizing the Coulomb repulsion between negatively charged deprotonated carboxylic groups. In this scenario, the honeycomb structure becomes unstable upon deprotonation and the system "collapses" into a more packed structure in which ionic hydrogen bonds play an important role. The phase transition is driven by deprotonation and is thus irreversible, consistent with the experimental findings.

In conclusion our experiments and calculations suggest that intermolecular ionic hydrogen bonds offer a novel possible path to the assembly of supramolecular structures on surfaces. The obtained supramolecular structures are stable even in the absence of counter ions (which are necessary in the solvent phases to stabilize ionic hydrogen bonds) because of an effective screening of the charge by the nearby metal surface.

5.2 4,4′,4″-benzene-1,3,5-triyl-tri-benzoic acid on Ag(111)

Further experiments to examine the important role of surface chemical reactivity and ionic hydrogen bonds in supramolecular self-organization were done on two-dimensional self-assemblies of an phenyl-extended, rigid version of TMA, the 4,4′,4″-benzene-1,3,5-triyl-tri-benzoic acid (further on: BTA), which was synthesized as described elsewhere [112] and sublimed twice before use. The chemical structure of the BTA molecule is shown in Scheme Figure 5.2b: around the central benzene core three 4′-benzoic acid groups are arranged in a three-fold symmetry. We find that BTA displays a more complex assembly behavior than its homologous TMA, involving three distinct structures occurring at different temperatures on a Ag(111) surface. We have determined the supramolecular structures and the mechanics of the structural transition by combined STM- and STS-measurements and theoretical modeling.

The Ag(111) surface was cleaned by repeated cycles of sputtering with 500eV Ar^+ ions and subsequent annealing to ∼800K. The BTA molecules were deposited onto the Ag(111) surface held at a temperature of 200K to 250K by means of OMBE, with the crucible containing the BTA molecules held at a temperature of 550K during deposition. The BTA coverage was always in the submonolayer range, typically a third of the surface was covered with BTA molecules. STM and STS data were acquired at a temperature of 5K. Tunneling Spectra were recorded with the lock-in amplifier set at a modulation frequency of 5kHz and a modulation amplitude of 10mV. In all measurements the cleanness of the tip was checked on the clean Ag(111) surface. The computational modeling was done, like in the studies of TMA on Ag(111) in Chapter 5.1 in collaboration by A. De Vita, by a combination of *ab initio* calculations and classical molecular dynamics techniques. The first-principle calculation were carried out using the Car-Parrinello method [92], whereas the classical constant temperature simulations were performed using the AMBER© package with the metal surface modeled as a planar layer of benzenes at fixed positions. For details of the calculations see [113].

The deposition of BTA molecules onto a Ag(111) surface held at a temperature of ∼200K followed by an annealing in the range from 270K to 300K results in the formation of a regular two-dimensional *honeycomb-structure* (Figure 5.14a - Phase I). However, holding the temperature of the Ag(111) surface above 320K during deposition results in the evolution of a second phase, a *ribbon-structure* consisting of equal spaced one-dimensional rows (Figure 5.14b Phase II). Alternatively, the *honeycomb-structure* can be trans-

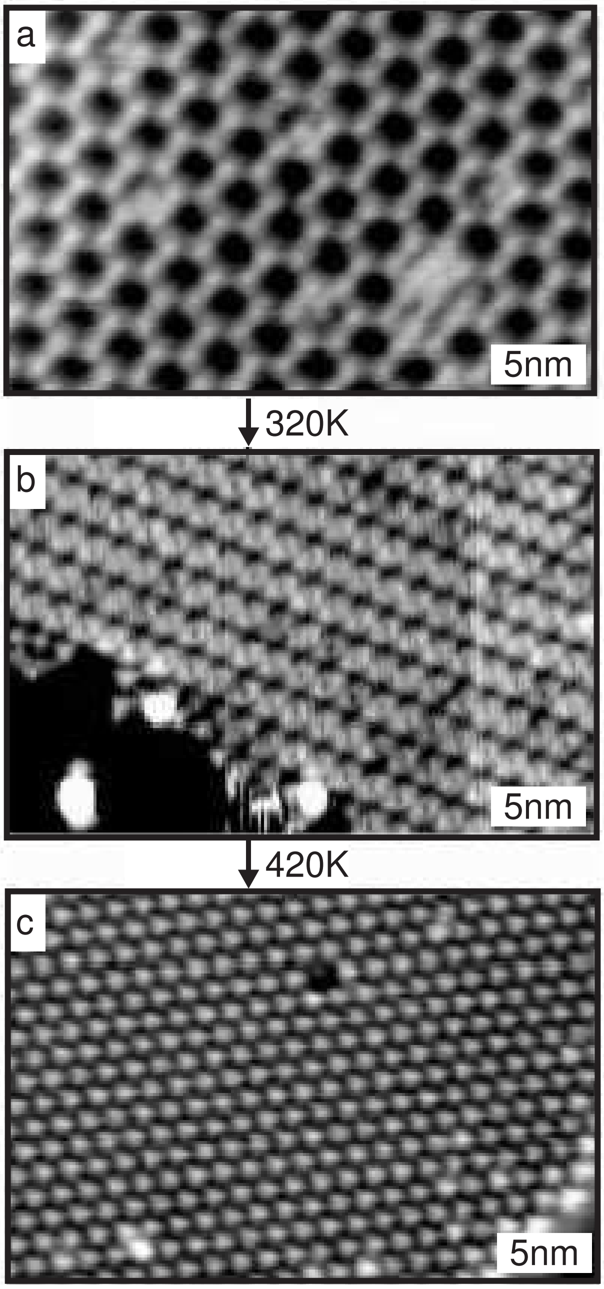

Figure 5.14: The deposition of the BTA molecules onto a Ag(111) surface results in the formation of three different supramolecular motifs, depending on the Ag(111) temperature. **a** Phase I - open two-dimensional *honeycomb structure* **b** Phase II - one-dimensional *ribbon structure* **c** Phase III - two-dimensional *close packed structure*. (U=500mV, I=500pA, T=5K)

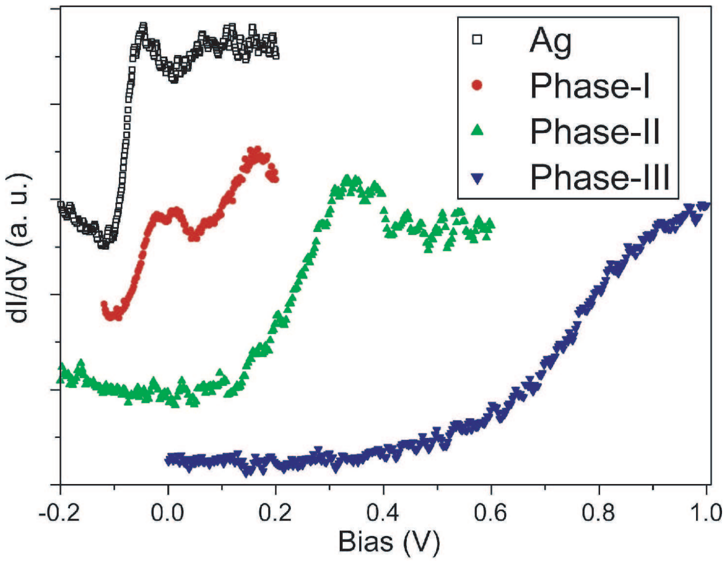

Figure 5.15: Tunneling spectra acquired at the clean Ag(111) surface and the three phases, respectively. All spectra were taken at 5K, with the lock-in amplifier set to a frequency of 5kHz and a modulation of 10mV. The tip was stabilized before taking the spectra at 0.2V and 1.5nA, 0.2V and 0.7nA, 0.6V and 0.5nA, 1V and 1nA, for clean Ag, phase I (*honeycomb*), phase II (*ribbon*) and phase III (*closed packed*), respectively. The tunneling spectra acquired on the clean Ag(111) surface shows an onset at -70meV, the characteristic feature of a two-dimensional Shockley type surface state. Tunneling spectra acquired on the three different structures still show this onset, but broadened and shifted to higher energies. This modification of the surface state indicates the presence of negatively charged adsorbates at the surface, which are associated with carboxylate groups.

formed into the *ribbon-structure* by annealing at a temperature of 320K. Further increasing of the Ag(111) temperature above 420K results in the emergence of a third phase, a two-dimensional *close packed structure* with three-fold symmetry (Figure 5.14c - Phase III). All three structures form extended domains and both phase transformations are completely irreversible. In all three structures the STM images reflect the shape of the BTA molecule and thus indicating flat-lying BTA molecules, meaning the molecules adsorb with their benzene rings parallel to the Ag(111) surface. The carboxylic acid groups are therefore located at the corners of the triangles. Annealing above 420K did not result in any new structures.

As BTA is a derivative of TMA and the functional groups acting as linkers between the molecules are in both cases carboxyl acid groups, one can expect a similar chemical behavior of BTA, especially a deprotonation of the carboxylic groups at elevated temperatures. To investigate a potential deprotonation of carboxylic groups as the origin of the phase transitions we considered our previous measurements of TMA on Ag(111) (Chapter 5.1), where we could show that the carboxylate groups stay partially negatively charged upon adsorption and thus shifted the onset of the surface state to higher energy, in agreement with previous measurements described in literature [94, 95, 102, 103, 104, 105, 106]. Therefore, tunneling spectra were acquired at the three phases (Figure 5.15). The tunneling spectrum taken on the clean Ag(111) surface shows as typical feature of a two-dimensional Shockley type surface state an onset at -70meV, in agreement with previous measurements [83, 84, 85]. This feature of the surface state is modified by the adsorption of BTA in all three phases, with the onset becoming broader and shifting to -20meV, 250meV and 700meV for phase I (*honeycomb*), II (*ribbon*) and III (*closed-packed*), respectively. The onset broadening and shifting is essentially independent of the tip position, i.e. positioning the tip at the center or the corners of a BTA molecule produced similar spectral features. This suggests that the observed onset essentially probes a modified surface state. Phase I (*honeycomb structure*) consists of neutral BTA molecules that weakly adsorb on the surface, comparable to the TMA *honeycomb structure* in Chapter 5.1, a fact that is reflected in the small upward shift (to higher energy) of 70meV of the surface state onset, comparable to adsorbed noble gas atoms [94, 95, 96]. In contrast, phase II (*ribbon structure*) and phase III (*close packed structure*) shift the onset by 320meV and 770mev upwards. These significant shifts to higher energies in both phases indicate the presence of negatively charged adsorbates at the surface, which are associated in accordance to Chapter 5.1 with charged carboxylate groups [102, 103, 104, 105, 106]. The further shifting and broadening of the onset of Phase III with respect to Phase II reflects the development of the deprotonation process, i.e. a stepwise increment of the number of carboxylate groups per BTA molecule [106]. No statement on the number of carboxylate groups per BTA molecule in Phase II and Phase III can be made. Furthermore, we do not have knowledge about the charge distribution within the structures. Based on STM- and STS-measurements and on calculations we propose the following models for the three BTA phases.

Phase I represents a two-dimensional open hexagonal network, which incorporates a regular array of cavities of 2.9nm inner diameter and 3.1nm periodicity (Figure 5.16a). The supramolecular interconnection of the BTA molecules is achieved by symmetric hydrogen bonds of carboxylic acid dimers, as shown in Figure 5.16b and 5.16c. The $O\cdots O$ distance is estimated at a value of 0.33nm, as expected for this type of bonds. Structurally the *hon-*

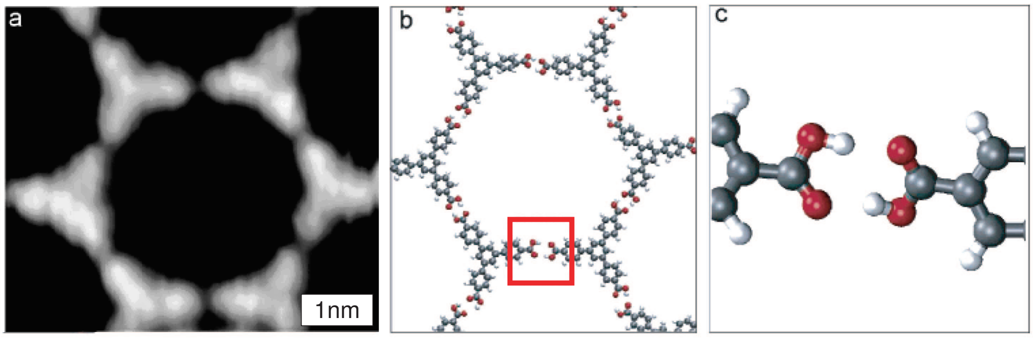

Figure 5.16: **a** High resolution STM image of Phase I (*honeycomb structure*). The STM-image reflects the shape of the BTA molecules, indicating flat lying molecules. **b** Atomistic model proposed for Phase I **c** The modeled double hydrogen bond between two carboxylic groups. (U=500mV, I=500pA, T=5K)

eycomb structure in Phase I is similar to that of the TMA system, shown in Chapter 5.1, although the pore size is significantly enlarged to 2.9nm. The STM images reflect the shape of the BTA molecules, indicating flat lying molecules. In order to investigate its stability, this phase was modeled with the AMBER© package. The system was held in planar geometry, as the BTA molecules adsorb flat lying, as shown in the STM images. The resulted equilibrium structure is shown in Figure 5.16b. Although the surface modeled out of benzene rings is probably less effective in stabilizing the structure than real metal substrate, the network proved to be stable up to relatively high temperatures in the modeling. The structure consists of a network of BTA molecules doubly bound to each other by neutral hydrogen bonds between the carboxylic acid groups as shown in Figure 5.16c to form the *honeycomb structure*.

Phase II has a *ribbon structure* as shown in Figure 5.17a. Within the single rows two BTA molecules are arranged in pairs forming a band of 1.70nm width. The periodicity along the row is 1.55nm and the row to row spacing in 2.18nm. The *ribbon structure* of Phase II is far less immediate to model, as it presents molecules arranged in stripes that keep apart from each other (Figure 5.17). The STM images reflect the shape of the BTA molecules, indicating flat lying molecules. The AMBER© package was used to investigate the stability of the observed *ribbon structure* in Phase II. The simulations were carried out for different ribbon configurations imposing the same temperature, spacing and substrate initial conditions. The rows were either made out of BTA molecules with the carboxylic acid groups fully protonated or with BTA molecules having one carboxylate group. It was found that in both cases the rows appear to be stable up to high temperatures (600K

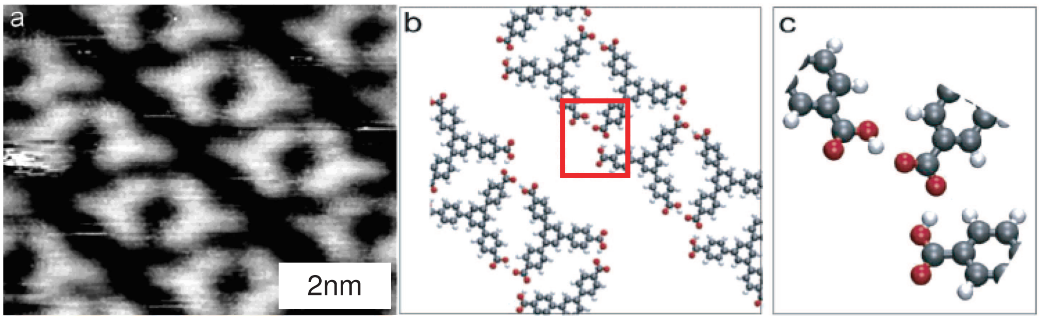

Figure 5.17: **a** High resolution STM image of Phase II (*ribbon structure*). As the STM image again reflects the shape of the BTA molecule we can emanate flat lying molecules **b** Atomistic model proposed for this chiral asymmetric structure. Each BTA molecule is singly deprotonated but still links with neighboring molecules by ionic hydrogen bonds between the carboxylate group and carboxylic groups **c** Detail of the ionic hydrogen bond corner linkage. (U=500mV, I=500pA, T=5K)

in the simulations). When using fully protonated BTA molecules, neighboring rows tend to stick to each other, contrary to our STM observations. On the other hand, when using BTA molecules containing one carboxylate group, neighboring parallel rows remain apart from each other during the simulations, consistent with the experimental results. This all suggests that the observed behavior is due to repulsive interaction between the neighboring rows containing negatively charged carboxylate groups on their borders. This electrostatic repulsion cannot be overcome by hydrogen bonds between carboxyl groups of neighboring chains, since all the available carboxyl hydrogens are involved in the internal linkage structure of the individual chains. Furthermore, the repulsion can be expected to be significant at short intermolecular distances even after taking into account the surface electrostatic screening, yielding stable structures with separated molecular ribbons at the experimental coverages. The most stable structure identified for Phase II is the one shown in Figure 5.17b. It contains one carboxylate group bound to two different protonated carboxyl acid groups by two ionic hydrogen bonds (Figure 5.17c). One of the hydrogen bonds is tilted backwards, yielding a chiral stepped structure for the row. This structure was found to be more stable than any other structure we could produce with further modeling and furthermore to be the structure in best agreement with the observed STM images. Similar to the results of TMA on Ag(111) of Chapter 5.1 we note, that while the *honeycomb structure* corresponds to the optimal hydrogen bonding geometry between fully protonated BTA molecules, it would be-

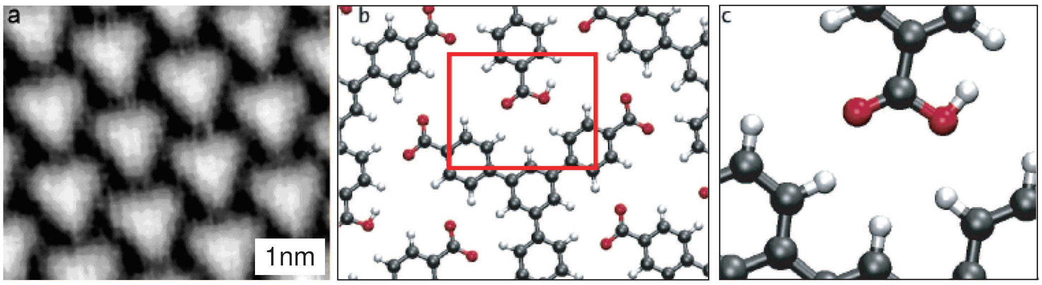

Figure 5.18: **a** High resolution STM image of Phase III (*close packed structure*). The STM images again reproduce the shape of the BTA molecules, indicating flat lying molecules. **b** Atomistic model of phase III. Each BTA molecule is doubly deprotonated in this model with the remaining hydrogen tilted backwards. No hydrogen bonds are formed between carboxyl or carboxylate groups. **c** Hydrogen bond between remaining protonated carboxylic acid group and the C-H atoms of the phenyl ring of a neighboring BTA molecule. (U=500mV, I=500pA, T=5K)

come relatively unstable if the BTA molecules contain one carboxylate group as such a structure would implying couples of adjacent negatively charged mutually repelling oxygen atoms, located on the non hydrogen bonded side of facing carboxylic acid group pairs. The results of the calculation, in agreement with the tunneling spectroscopy data, suggests that thermally initiated deprotonation of one carboxylic acid group per BTA molecule is the driving force for the transition from the *honeycomb structure* of Phase I to the *ribbon structure* of Phase II.

Phase III consists of a hexagonal *close packed structure* with a lattice constant of 1.36nm. In the STM images the shape of the BTA molecules is reflected, indicating that the molecules are adsorbed in a flat lying geometry. Within this structure, every carboxyl acid group is pointing to the mid-edge of an adjacent molecule as shown in Figure 5.18a. Therefore a binding between carboxylic acid functions (or carboxylate groups) can be excluded, but one has to suppose rather a binding between carboxylic (or carboxylate) groups and the C-H atoms of the phenyl rings of neighboring BTA molecules. Again simulations were performed to investigate the origin of the transformation from Phase II to Phase III upon elevated temperature. Considering the hitherto behavior of the carboxylic groups and the results of the tunneling spectroscopy performed on Phase III, one can assume that the phase transition is triggered by a further deprotonation of carboxylic acid groups of the BTA molecules. When subtracting more than one proton per molecule even Phase II becomes unstable, since at least two hydrogens are needed to bind together three carboxylic acid groups as shown in Figure 5.17c. Experimentally the system changes into the *close packed structure* upon further annealing. At first it would seem reasonable to assume that complete deprotonation of the carboxylic acid groups were implied by such a structure. However, our classical modeling indicates that the high density of negative charges left by a complete deprotonation introduces an exceedingly large repulsive contribution to the cohesive energy of the supramolecular structure. Any attempt to reproduce a stable packed structure of fully deprotonated (-3e charged) molecular ions with classical codes failed, the repulsive energy term being too high for the system to remain stable. A simple estimation of the repulsive energy can be obtained by approximating each negative carboxylate group (screened by the metal surface) with a standing electric dipole. The system thus becomes a network of dipoles set on a regular triangular lattice, with a repulsive energy per molecule of $\sim$10eV. This should be compared with the attractive interaction between the molecules, which can be estimated by an *ab initio* calculation modeling the bonding of a deprotonated benzoic acid with one BTA molecule in gas phase, which yields 1.8eV per molecule. This is much less than the repulsive contribution, indicating that a fully deprotonated, fully charged system is unlikely to form. Therefore different states of charge or less than fully deprotonation must be considered. To include a different charge state of the adsorbed, fully deprotonated BTA molecule, we modeled the system with an *ab initio* simulation containing a single BTA molecule over 5 layers of Ag(111) in each periodically repeated cell of a hexagonal surface lattice. After electronic and ionic relaxation, the electron density was integrated over the volume occupied by the molecule in order to evaluate its charge state. The calculated value for the charge of the fully deprotonated adsorbed molecule is -1.97e. The *ab initio* calculations predicts that the adsorbed, fully deprotonated is less negatively charged then the expected -3e. The repulsive energy estimated as before decreased to $\sim$4.5eV, which is still too high to yield the *close packed structure* of Phase III. We then addressed the alternative hypothesis of incomplete deprotonation, especially a doubly deprotonated system containing two carboxylate groups per BTA molecule. An *ab initio* calculation revealed that the Phase III arrangement is still compatible with the presence of protonated oxygens of carboxyl acid groups if the $O\cdots H$ bond is tilted backwards as shown in Figure 5.18b and Figure 5.18c. In such a system the calculated charge of the molecule is -1.17eV. This corresponds to an estimated repulsive energy of $\sim$1.5eV, which is low enough to be compatible with the occurrence of a *close packed structure*. Thus, the Phase III is rationalized by a structure formed of BTA molecules containing two carboxylate groups. In this structure, both the carboxylate groups and the still protonated carboxylic acid group bind to the inner pocket of C···H protons of the neighboring BTA molecules leading to an intermolecular ionic hydrogen bonding network, as shown in Figure 5.18b. For details of the calculations see [113].

Recapitulating, after depositing BTA onto a Ag(111) surface and stepwise annealing, three different supramolecular structures could be fabricated. An open *honeycomb structure*, a one dimensional *ribbon structure* and a two dimensional *close packed structure.* Tunneling spectra acquired at the three phases suggested that the phase transformations are due to progressive deprotonation of the carboxylic acid groups, forming negatively charged carboxylate groups, of the BTA molecules. This is in agreement with the irreversible phase transformations. Theoretical modeling by *ab initio* and classical molecular dynamics calculations has been used to reproduce and interpret the experimental results. When one carboxylic group per BTA molecule is deprotonated the first phase transition from *honeycomb structure* to *ribbon structure* takes place. When further deprotonation occurs the intermolecular links within the *ribbon structure*, consisting of ionic hydrogen bonds between carboxyl acid groups and carboxylate groups, are broken and the second phase transition onsets. During this processes the neutral hydrogen bonds connecting the carboxyl acid groups (*honeycomb structure*) are substituted with ionic hydrogen bonds between carboxylic groups and carboxylate groups (*ribbon structure*)and finally by ionic hydrogen bonds between carboxylic/carboxylate groups and phenyl C-H protons (*close packed structure*). Our results indicate that deprotonation is necessary to rationalize the occurrence of the self-assembled structures in the observed order.

In conclusion our experiments and calculations on the BTA/Ag(111) system augmented and endorsed our knowledge about the role of ionic hydrogen bonds in supramolecular systems on metal surfaces obtained by our investigations on the TMA/Ag(111) system in Chapter 5.1. Again charged carboxylate groups within the structures could be identified, catenating the BTA molecules via ionic hydrogen bonds into specific supramolecular structures. Due to the more complex shape of the molecules a more elaborate behavior can be observed.

Chapter 6

Surface state modification by self-assembled supramolecular nanocavities

In the idealized case of an infinite crystal, the Bloch wave-vectors have to be real-valued to ensure that the corresponding wave functions can be normalized. Complex-valued Bloch wave-vectors would correspond to exponentially growing wave functions which cannot be normalized and therefore have to be rejected [114]. By breaking the translational symmetry in one direction by introducing a surface, one obtains a semi-infinite crystal and complex-valued Bloch wave-vectors are allowed. The exponentially growing wave function inside the crystal can be matched at the surface with the exponentially decaying wave function in the vacuum, resulting in a wave function which can be normalized. This wave-function is obviously localized at the surface of the crystal, thus forming a *surface state*, whose origin is the breaking of the translational symmetry perpendicular to the surface. The translational symmetry parallel to the surface persists and the surface state electrons are free to move and consequently constitute a two-dimensional electron gas which can be characterized by the Bloch wave-vector $k_{\|}$. A prerequisite for the existence of a true surface state is the absence of bulk states with the same energy E and the same $k_{\|}$ as the surface state. When a crossing of a surface state band with projected bulk states occurs, one obtains a so called surface resonance, which are bulk states with an enhanced probability at the surface. A detailed introduction in the theory of surface states and the historical development can be found in [115] and the references therein.

Surface states can be found on various crystal surfaces. Especially on noble metal (111) surfaces one can find surface states in close proximity to the Fermi energy, which are easily accessible by STM [116]. Surface properties are influenced by the surface state as they contribute a considerable fraction to the local density of states (LDOS) at the surface. For example, they affect the physisorption potential, surface reconstructions and have an important role in epitaxial growth [117, 118, 119].

The Shockley-type surface states of noble metal (111) surfaces have been extensively studied by angle-resolved photoemission [120, 121, 122, 123, 124], k-resolved inverse photoemission spectroscopy [125, 126, 127, 128] and STM [25, 83, 84, 85, 129]. The picture which emerges from these measurements is that of a two-dimensional free electron gas. The surface-state dispersion relation is *parabolic* as well as *isotropic*:

$$E = E_\Gamma + \frac{\hbar^2}{2m^*} k_\parallel^2 \tag{6.1}$$

In Equation 6.1 E_Γ is the surface state band edge energy and m^* is the effective mass of the surface state electrons. In the case of the Ag(111) surface these parameters are E_Γ=-67meV and m^*=0.40m_e, with m_e being the mass of the electron [130, 131]. The effective mass m^* is considerably smaller than m_e due to the presence of the periodic crystal potential. The density of states of a two-dimensional free electron gas is a step function Θ with the onset at E_Γ:

$$\rho_{2D}(E) = \frac{m^*}{\pi\hbar^2}\Theta(E - E_\Gamma) \tag{6.2}$$

Scanning Tunneling Spectra taken on flat terraces far from impurities show indeed such a behavior. The total density n_0 of the surface state electron gas is given for $E_\Gamma < E_F$ by:

$$n_0 = |E_\Gamma| \frac{m^*}{\pi\hbar^2} \tag{6.3}$$

If we use for the energy E the physical unit electronvolt [eV], E is directly related to the bias voltage in dI/dV-measurements.

The step-function like LDOS of the surface state electron in Equation 6.2 is only valid for a perfect surface, where the surface state electrons behave as two-dimensional free electrons. But surface defects will result in a scattering of the electrons at and in close proximity of these defects. Surface state electrons may be reflected elastically on such defects and interference effects may alter the LDOS around these defects. These defects, acting as scatterers, can be of various kind. First of all even the best prepared surface shows impurities, step edges separating terraces and reconstructions. It was shown by STM-measurements that these defects as well as adsorbed atoms and molecules act as scatterers, which modify the surface state LDOS [20, 21, 22, 129, 131, 132, 133, 134, 135, 136, 137]. Apart from simple scattering, one can show that a confinement of surface state electrons due to defect structures can occur. It was shown with STM that the two step edges bordering a terrace form a Fabry-Prot resonator, which confines the surface state electrons [138] as well as islands and vacancy islands act as two-dimensional resonators for surface state electrons [26, 27, 139, 140]. Confinement of surface state electrons is also possible in closed structures made of single adatoms, assembled by individually positioning of the adatoms by the STM tip. This was first done by Crommie et al. and labelled *quantum corral* [25]. Due to the steered assembly of the structures by positioning of the atoms with the STM-tip one can fabricate a huge variety of surface state electron resonators, enabling a targeted engineering of properties of the surface state electrons [9, 24, 141, 142, 143].

In this Chapter we want to examine the idea if cavities in self-assembled supramolecular structures can act as *quantum corrals*, considering the measurements of Gross et al. that organic molecules act as scatterer for surface state electrons [22]. This would provide the possibilities for not only a quick production of *quantum corrals*, as the time-consuming sequential fabrication by tip-manipulation used nowadays would be replaced by a fast self-assembly process, but furthermore the production of extensive periodic patterns of *quantum corrals*, which might be suitable for integrating measuring methods and interesting for technological applications.

The self-assembled supramolecular structure used for our experiments within this Chapter is the hexagonal BTA *honeycomb* structure (shown in Figure 6.1, examined in our experiments in Chapter 5.2, where we investigated the structures formed out of BTA molecules on Ag(111). This structure contains cavities, which are areas of pristine Ag(111) enclosed by BTA molecules. One can expect that the cavity surrounded by molecules act as a resonator, confining surface state electrons and thus having a modified LDOS inside the cavities with respect to a clean Ag(111) substrate. The sample preparation was performed under the same conditions and parameters as described in Chapter 5.2. All STM measurements were performed at a temperature T of 5K and the settings of the lock-in amplifier were always 5kHz for the modulation frequency f and 10mV for the modulation amplitude V_{pp}. The tip was stabilized before acquiring the spectra at a bias voltage U_{stab} and a tunneling current I_{stab}.

In Figure 6.1a an STM-topograph of the BTA-*honeycomb* structure is shown and in Figure 6.1b a model of the geometry of the cavity is displayed. The registration of the BTA molecules on the Ag(111) substrate is not known, as it was not possible to resolve the Ag(111)-substrate simultaneously with

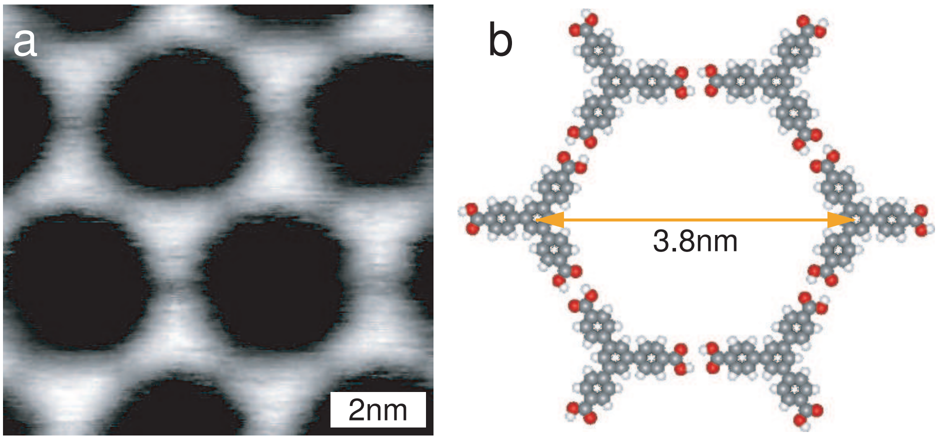

Figure 6.1: **a** STM topograph (U=500mV, I=500pA, T=5K) **b** model of the BTA *honeycomb* structure. The diameter of the cavity is defined as the as the center to center distance of the BTA molecules and equals 3.8nm.

the supramolecular structure. The cavities are of hexagonal shape and surrounded by six BTA molecules, with a diameter of 3.8nm, defined as the center to center distance of the BTA molecules located on opposing corners of the hexagon. No indication can be found that the interior of the cavity is anything but pristine Ag(111).

In Figure 6.2 a dI/dV-tunneling spectrum acquired in the center of a hexagonal cavity of the BTA-*honeycomb* network is shown, with a dI/dV-tunneling spectrum acquired on a clean Ag(111) area as reference. The cavity was located in the middle of a BTA-*honeycomb* island, far enough away from defects like step edges, island borders, domain boundaries or modified cavities to exclude a contribution of these defects to the measurement. As one can see, the LDOS in the center of the cavity is modified with respect to the spectrum of pristine Ag(111). Whereas on the clean Ag(111) the LDOS is of step-function shape, reflecting the two-dimensional free electron gas, the LDOS in the center of the cavity shows a pronounced, broad peak superimposed to a step function. The LDOS in the center cavity was fitted with the sum of an *arc tangent* (for the onset) and a Lorenz-shaped peak (for the peak). The fitting revealed that the peak is located at a bias voltage of 47mV±10mV and has a FWHM of 122mV±70mV. No higher order peaks could be seen in the dI/dV-spectra.

Mapping the dI/dV-signal at the peak voltage of 50mV simultaneously with the topographic data as shown in Figure 6.3a and b reveals that the modification of the LDOS at 47mV seen in dI/dV point-spectra is spatially localized to the center of the cavities of the BTA *honeycomb* structure. We

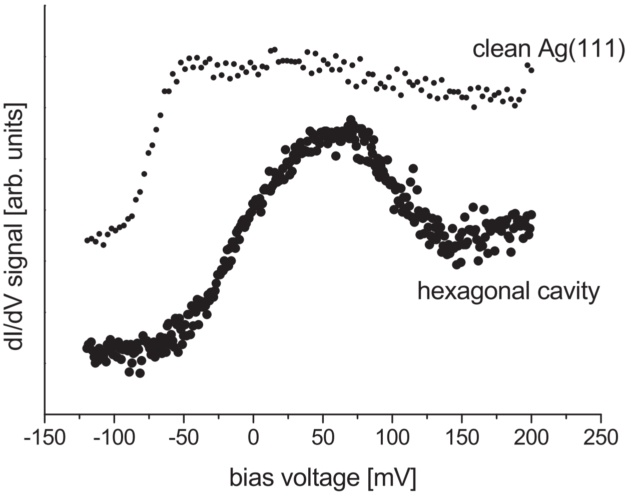

Figure 6.2: dI/dV-tunneling spectroscopy acquired in the center of a hexagonal cavity and on clean Ag(111). The LDOS on the clean Ag(111) surface shows the typical step-function like shape of a two-dimensional free electron gas whereas the LDOS in the middle of the cavity shows a broad peak located at 47mV±10mV and a FWHM of 122mV±70mV, superimposed to an onset. (f=5kHz, V_{pp}=10mV, U_{stab}=200mV, I_{stab}=500pA, T=5K)

can also see that in cavities located on the border of BTA-islands or bordering defects in the *honeycomb* structure, e.g. cavities filled with an accessory BTA-molecule, a modification of the LDOS inside the cavities at 50mV takes place.

It is of major concern if the LDOS modification inside the cavities is a periodic or local problem. To see possible differences between cavities in periodic and local environments we performed dI/dV-tunneling spectroscopy in the centers of cavities located in the middle of well-ordered BTA-islands, which are in a good approximation in a periodic arrangement, and on the border of a BTA islands, which is for sure a non-periodic arrangement. These spectra are shown in Figure 6.4. Fitting the dI/dV-spectrum taken in the center of a hexagonal cavity located on the border of a BTA *honeycomb* island revealed that the peak is at a bias voltage of 43mV, which is only slightly decreased compared to the 47mV in the periodic environment, and has a FWHM of 100meV, which is also comparable with the periodic environment. Our measurements in the periodic and local environment clearly show that the modification of the LDOS inside the cavities is rather a local phenomenon than a periodic problem, although a minor crosstalk between neighboring cavities cannot be excluded.

As the modification in the LDOS is spatially localized to the center of the cavities, which is pristine Ag(111), and not on the BTA molecules itself, we

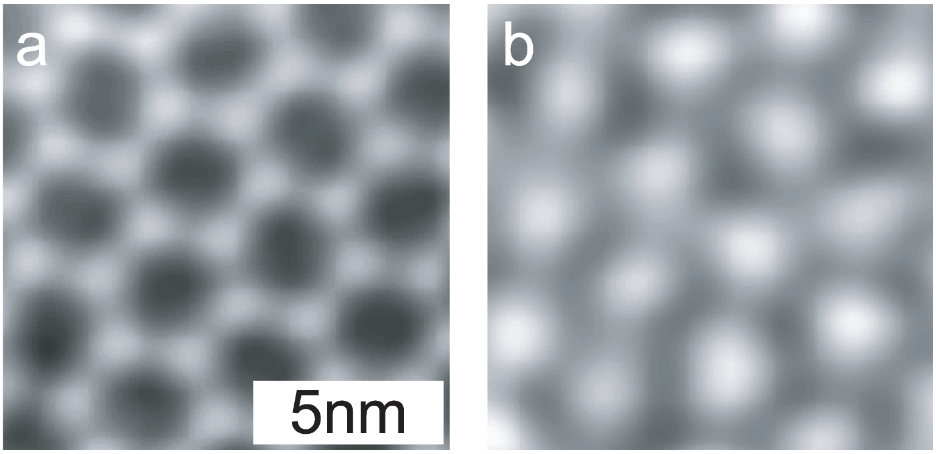

Figure 6.3: **a** STM topograph of the hexagonal BTA *honeycomb* structure (U=50mV, I=500pA, T=5K) **b** Map of the dI/dV-signal, acquired simultaneously with the topograph in **a**, at a bias voltage of 50mV which corresponds to the peak in the LDOS in the center of the cavity. (U=50mV, I=500pA, f=5kHz, V_{pp}=10mV, T=5K)

exclude electrons from molecular orbitals of the BTA molecules as origin of the LDOS modification, but conclude that we observe a modification of the Ag(111) surface state itself due to a confinement of the surface state electrons inside the resonator formed by the six BTA-molecules bordering the cavity. To verify if our observations are due to a resonance of the surface state electrons inside a cavity, we started with the simple model of a "particle in a box", which is also related to the Fabry-Perot Interferometer in optics. Although this model might be oversimplified as it deals with a strictly localized confinement in only one dimension, we will earn information on the energies of the resonance states with respect to the resonator size, which can be compared to experimental results. Under the assumption of a "hard wall", meaning that the surface state electrons cannot penetrate the wall, in a one-dimensional system a standing wave is formed inside the resonator if the diameter d of the resonator equals an integer multiple n of the half of the wavelength.

$$d = n \times \frac{\lambda}{2} \tag{6.4}$$

λ is related to the electron energy by the dispersion relation, with E_Γ being -67mV:

$$\lambda = \frac{2\pi}{k} \tag{6.5}$$

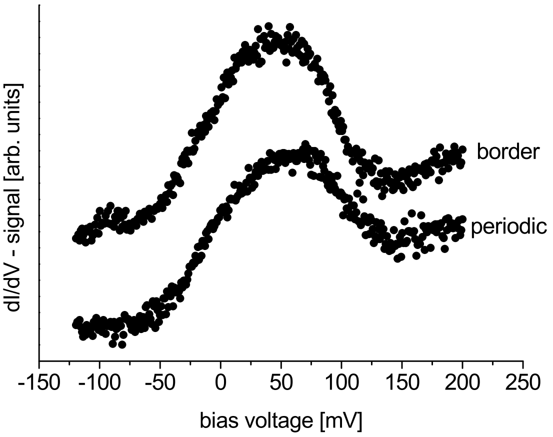

Figure 6.4: dI/dV-tunneling spectra taken in the centers of cavities located in a periodic arrangement (middle of an island) and non-periodic arrangement (border of an island). The peak position in the non-periodic environment is shifted to 43mV, which is only slightly decreased compared to the 47mV in the periodic environment.(f=5kHz, V_{pp}=10mV, U_{stab}=200mV, I_{stab}=500pA, T=5K)

$$k = \sqrt{\frac{2m^*}{\hbar^2}(E - E_\Gamma)} \tag{6.6}$$

For the energy E of the first standing wave (n=1) we therefore achieve:

$$d = \frac{\pi}{k} = \frac{\pi}{\sqrt{\frac{2m^*}{\hbar^2}(E - E_\Gamma)}} \tag{6.7}$$

Equation 6.7 describes the relation between the length of a one-dimensional resonator with impenetrable walls and the energy of the first standing wave. In a perfect resonator these standing waves are the only electronic states where one will find electrons. In an imperfect resonator with "leaking" walls (having a reflection coefficient smaller than 1) the energy levels will be broadened and shifted to lower energy with decreasing reflection coefficient [144]. We squared Equation 6.7 to obtain:

$$E - E_\Gamma = \frac{\pi^2\hbar^2}{2m^*} \times \frac{1}{d^2} \tag{6.8}$$

We now assume that d^2 is the area A of the two-dimensional resonator, an assumption which is correct apart from a form factor. By inserting the

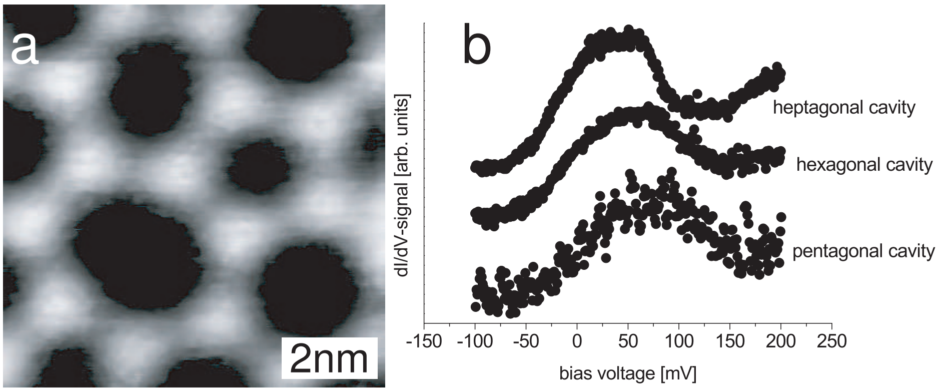

Figure 6.5: **a** STM image of a domain boundary showing cavities of pentagonal, hexagonal and heptagonal shape with different sizes. The cavity-area was defined as the polygon connecting the centers of the BTA molecules and accounted 5.7nm^2±0.5nm^2 for the pentagonal cavities, 9.0nm^2±0.5nm^2 for the hexagonal cavities and 12.8nm^2±0.6nm^2 for the heptagonal cavities. (U=500mV, I=500pA, T=5K) **b** Tunneling spectra acquired in the centers of pentagonal, hexagonal and heptagonal cavities. The expected shift of the peak position to a higher bias voltage for the smaller pentagonal cavity and to a smaller bias voltage for the larger heptagonal cavity can be seen. A detailed analysis revealed a bias voltage of 65.8mV±13.1mV for the peak in the pentagonal cavity, a bias voltage of 47.0mV±10mV for the peak in the hexagonal cavity and a bias voltage of 22.0mV±9.4mV in the heptagonal cavity. (f=5kHz, V_{pp}=10mV, U_{stab}=200mV, I_{stab}=500pA, T=5K)

constants in a way that the energy E is in [meV] and the length is in [nm] one obtains:

$$E - E_\Gamma = 939 \times \frac{1}{A} \tag{6.9}$$

The linear relation between $E - E_\Gamma$ and the inverse of the area was derived in a more accurate and systematic way for hexagonal and circular resonators [23, 27, 140] which differ only by a shape dependent prefactor. The area of the cavity was defined as a polygon connecting the centers of the BTA-molecules, with the so obtained area of the BTA cavity being 9.0nm^2±0.5nm^2. Calculating the energy of the first resonance with our simple estimation in Equation 6.9 gave a bias voltage of 39mV±6mV, which is in good agreement with our experimental findings.

If the experimentally observed modification of the LDOS inside the cavities is due to a confinement, the peak energy will depend on the cavity area as described Equation 6.9: $E - E_\Gamma$ is proportional to the inverse of the cavity area A. A strong indication for confinement of surface state electrons within our structures would be to check this coherence between energy and area. But in the examined BTA *honeycomb* structure we do not have any influence on the cavity area, which is predetermined only by the size of the used molecules, in our case BTA. The only way to examine cavities of different size is due to defects within the perfect hexagonal structure. In boundaries between differently oriented domains one can observe not only hexagonal cavities, but also smaller pentagonal and larger heptagonal cavities as shown in Figure 6.5a. This kind of defects provide us with cavities of different area, necessary to prove the idea of LDOS modification due to a resonance inside the cavities. Again the cavity area was defined as a polygon connecting the centers of the BTA-molecules. For the cavity areas we obtained 5.7nm^2±0.5nm^2 for the pentagonal cavities, 9.0nm^2±0.5nm^2 for the hexagonal cavities and 12.8nm^2±0.6nm^2 for the heptagonal cavities.

In Figure 6.5b dI/dV-tunneling spectra acquired in the centers of cavities with pentagonal, hexagonal and heptagonal shape, far from other defects which could influence the LDOS, are shown. One can see at first glance that the peak position is indeed shifted to a higher bias voltage in the smaller pentagonal cavities and to smaller bias voltage in the larger heptagonal cavities, with respect to the hexagonal cavities. A detailed analysis revealed that the peak in the pentagonal cavities is at a bias voltage of 65.8mV±13.1mV, in the hexagonal cavities at 47.0mV±10mV and in the heptagonal cavities at a bias voltage of 22.0mV±9.4mV. Furthermore a change in the FWHM of the peaks could be observed. The peak observed in pentagonal cavities had a FWHM of 140mV±65mV, the peak in hexagonal cavities had a FWHM of 122mV±70mV and the peak in heptagonal cavities had a FWHM of 91mV±31mV. Due to the large error bars of these measurements, no sound conclusions can be made based on them. But it seems that the peaks get broader with increasing energy, which would be equivalent with a degradation of the reflectivity of the walls. This would denote that at high energy more electrons can leave the resonator which is in agreement with the missing observation of higher order peaks.

In Figure 6.6 a plot of $E - E_\Gamma$ of the peak voltages in the pentagonal, hexagonal and heptagonal peaks as a function of the inverse cavity areas is shown, with E_Γ being -67mV. One can see an almost linear dependence of the peak energy on the inverse of the cavity area, as predicted by our simple model. A linear fit of the experimental data, with the line going through the origin, shows the relation connecting the inverse area and the peak energy is $E - E_\Gamma = 872\frac{1}{A}$ ($E - E_\Gamma$ in meV, A in nm^2), which is in qualitative good agreement to the $E - E_\Gamma = 939\frac{1}{A}$ predicted by our simple theoretical estimation. The line has to go through the origin for two reasons: in our

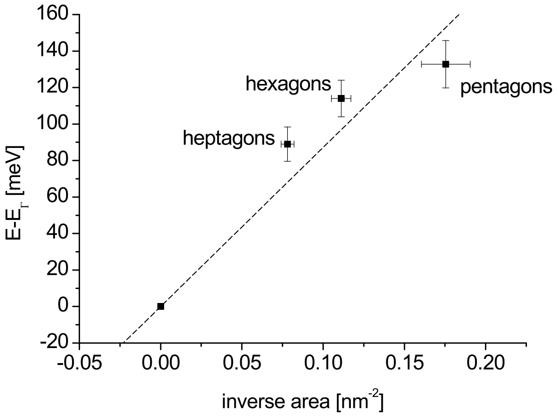

Figure 6.6: Peak voltages $E - E_\Gamma$ as a function of the inverse cavity area A. As one can see, there is a roughly linear relation between $E - E_\Gamma$ and the inverse of the cavity area A, as proposed by the simple model. A linear fit revealed that $E - E_\Gamma = 872\frac{1}{A}$, which is in good agreement with our estimation which resulted in $E - E_\Gamma = 939\frac{1}{A}$

model there is no offset. The second, intuitive reason is that if the inverse area goes to zero and therefore the cavity area goes to infinity the peak energy $E - E_\Gamma$ is shifted to the lowest possible value, which is zero. Therefore the line has to go through the origin.

As the measured bias voltages for the peak positions inside the different sized pentagonal, hexagonal and pentagonal cavities are in good agreement with the predicted energies, based on a very simple model, we conclude that the observed modification of the LDOS is indeed due to a standing wave formed inside the cavities bordered by BTA molecules, which act as *quantum corrals* for surface state electrons.

Chapter 7

Controlled grafting of macrocyclic molecules at surfaces: from spontaneously formed aggregates to single-molecule arrays

Within this chapter we report on investigations under UHV conditions on the sublimation, adsorption and the self-assembly behavior of the macrocyclic molecule mt33 (Figure 7.1) on the pristine Ag(111) surface and a prepatterned Ag(111) surface. mt33 is a typical building unit of catenanes or rotaxanes. Catenanes consist of two interlocked macrocyclic molecules, which do not have to be necessarily identical, and can rotate freely into each other. Rotaxanes are built up by a thread which is mechanically bonded into a macrocyclic molecule, which can translate freely along the thread and

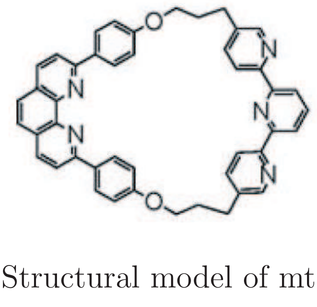

Figure 7.1: Structural model of mt33 molecules

rotate freely. Catenanes and rotaxanes are promising prototypes for molecular machines, as these molecules can be designed in a way that one can switch between a stable and a metastable configuration by an outer stimulation like exposure to light or a redox reaction, which is related to a change in properties like shape, conductance or wettability. Studies on the behavior of typical building units like macrocyclic rings are therefore necessary precursors for the more elaborate preparations and experiments on catenanes and rotaxanes [33, 145, 146, 147, 148].

On pristine Ag(111) the observation of the macrocyclic molecule mt33 was complicated by two disadvantages: Because of a weak molecule-substrate interaction the molecules are highly mobile at a substrate temperature around 300K. On the other hand, after cooling the sample to 5K, the molecules condensed into clusters which might hinder a real nanomachine in movement. To hinder the movement and the clustering of the mt33 molecules we investigated the possibility of preparing individual mt33 molecules by depositing them onto a prepatterned surface, allocating well-defined binding sites which can house individual mt33 molecules.

All measurements were performed under UHV-conditions at a base pressure below $\sim 1\times10^{-10}$mbar. The Ag(111) surface was cleaned by repeated cycles of sputtering with 500eV Ar^+ ions and subsequent annealing to 800K. The mt33 molecules were sublimed onto the Ag(111) surface, kept at a temperature of 300K, by means of an OMBE source with the crucible held at a relatively high temperature of 590K without any observation of degradation of the mt33 molecules. In the experiments the coverage was always in the submonolayer regime.

Attempts to perform STM measurements of mt33 at Ag(111) kept at a temperature of 300K failed. Only a flicker noise and a small amount of mt33 molecules decorating step edges could be seen, indicating a high mobility of the mt33 molecules on the Ag(111) surface and thus a very weak translational barrier for the mt33 molecules on the Ag(111) surface. The movement of the mt33 molecules could be hindered by lowering the sample temperature to 5K.

Figure 7.2 reproduces a typical STM topograph acquired at 5K of such a preparation. The mt33 molecules are imaged as "donuts", with the central part of each individual molecule appearing as a dark dent, which reflects the hollow nature of the ring shaped structure of the mt33 molecule, thus indicating intact molecules after sublimation. The observation of the "donut" shape points to a flat absorption of the individual molecules with their aromatic ring planes largely parallel to the surface. As evidenced in some recent investigations on metal substrates, the absorption of aromatic systems on metal surfaces is predominated by weak interactions of aromatic π-systems

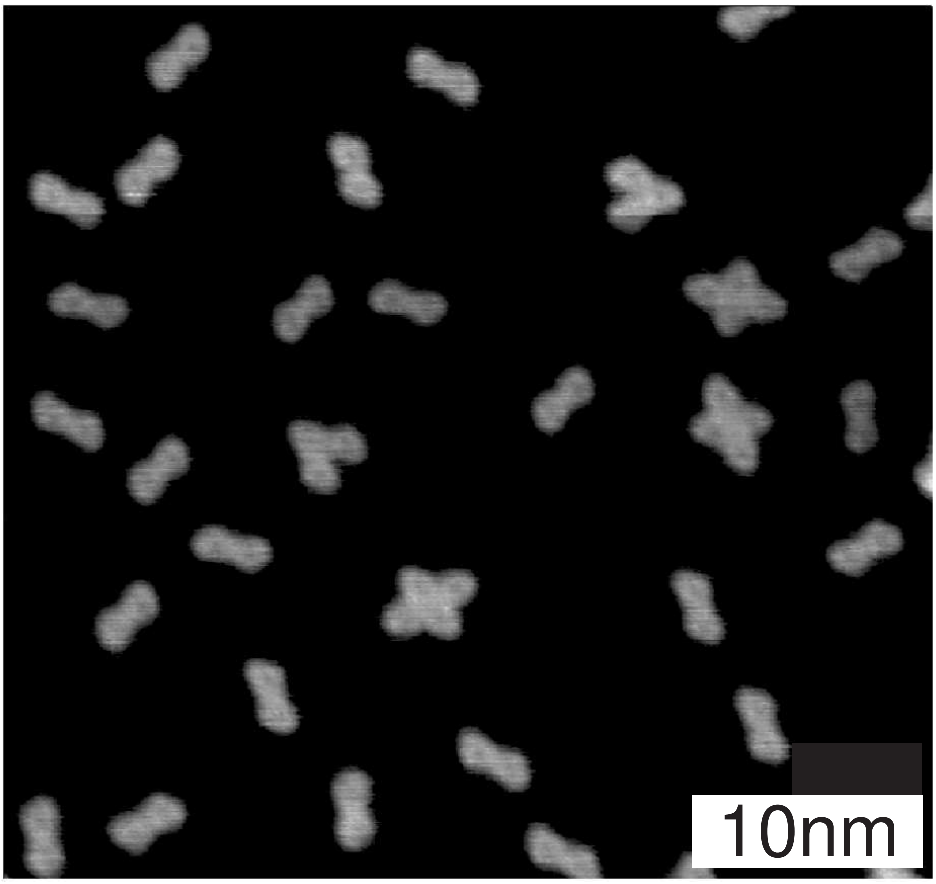

Figure 7.2: STM topograph of mt33 molecules at a temperature of 5K. Most mt33 molecules are aggregated into clusters. (U=2000mV, I=200pA, T=5K)

with the metal surfaces [149, 150]. The weak molecule-surface interaction scenario is further supported by high mobility of the mt33 molecules on the Ag(111) surface. The high resolution data in Figure 7.3a and Figure 7.3b elucidate an asymmetrically ellipsoidal shape of individual mt33 molecules consisting of a broader 2, $2'$, $6'$, $2''$-terpyridine (denoted as *head*) part and a sharper 1,10-phenanthroline part (denoted as *tail*).

An important observation is that in the STM topographs almost all mt33 molecules are aggregated into clusters, mostly dimers, trimers and tetramers. The cluster formation of mt33 on the Ag(111) surface was investigated in further detail in dependence on the molecular coverage. Figure 7.4 displays a statistical analysis of the cluster-size distribution at six different molecular adsorption dosages, with 400 to 1500 mt33 molecules being analyzed per coverage.

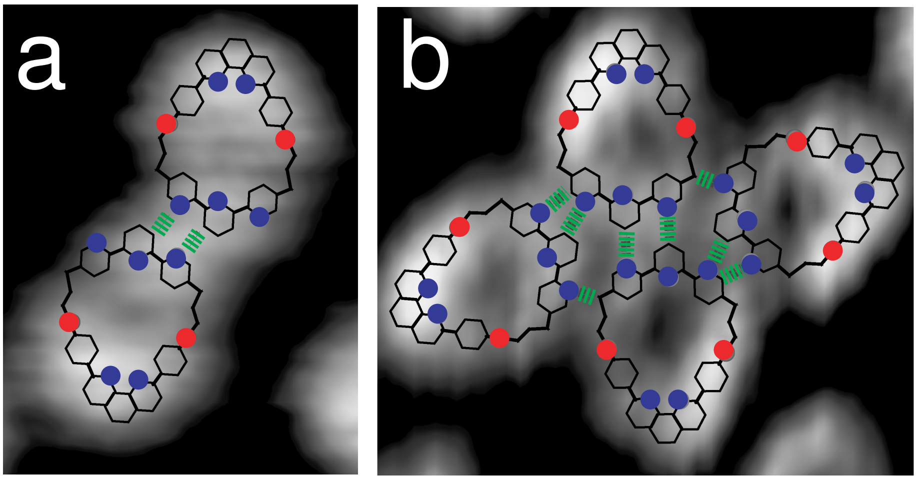

Figure 7.3: High resolution STM topographs of mt33 molecules in dimer and tetramer clusters at a temperature of 5K. U=2000mV, I=200pA, T=5K)

Only at very low coverages, very few isolated molecules can be observed, but already at a low density more than 50% of the adsorbed mt33 molecules form dimeric clusters. With increasing concentration, most of the adsorbed mt33 molecules form tetramers (with the intermediate observation of some few trimeric species) until they start to coalescence into larger clusters at coverage above 0.5 monolayer (1 monolayer = surface is fully covered by the adsorbed molecules). The driving force to spontaneous formation of dimeric and tetrameric clusters of mt33 at the Ag(111) surface lies in the preferential formation of the intermolecular hydrogen bonds between the terpyridine units.

Within the aggregates, the molecules form head-to-head arrangements for both the dimer and the tetramer. The intermolecular interactions are attributed to the hydrogen bonds between the nitrogen atoms and the protons of the aromatic rings of neighboring all *transoid* conformers of two 2, $2'$, $6'$, $2''$-terpyridine units, as proposed by the green dashed lines in Figure 7.3a and Figure 7.3b. Although C-H$\cdots$N bonds are considered to be weaker than O-H$\cdots$O or O-H$\cdots$N hydrogen bonds, *ab-initio* calculations indicate that two pyridine nuclei can be interact by C-H$\cdots$N bonds with a binding energy of 3.7kcal/mol and the formation of pyridine dimers on surfaces was also confirmed experimentally [146, 150, 151]. Such surface hydrogen bonding behavior is in strong contrast to the observed situation in the mt33 bulk-crystal: there the 2, $2'$, $6'$, $2''$-terpyridine units (also in the all *transoid* conformation) form exclusively intra-molecular hydrogen bonds and no inter-

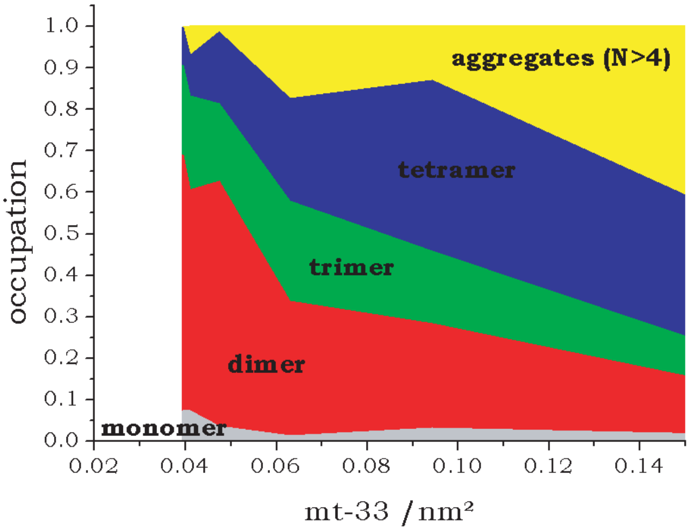

Figure 7.4: Amount of mt33 in the different kinds of observed cluster in dependence of the coverage.

molecular contacts could be observed. The different behavior in the bulk can be explained by predominance of the stronger π-π stacking interactions of the phenantroline moieties within the crystal lattice, which are hampered when the molecules are adsorbed on the metallic substrate. In addition, intercalated aromatic solvent molecules block efficiently the inter-molecular terpyridine-terpyridine interaction by N-H$\cdots$Ag interactions.

It was shown that the constituents of mechanical devices although grafted on a surface should only interact weakly with the substrate in order to be switched by external stimuli [146]. Therefore, the observed aggregation of the mt33 molecules may complicate the controlled individual addressing and manipulation due to the intermolecular coupling between the neighboring species. Hence it is imperative to graft individual mt33 molecules on the surface.

We could show that the intermolecular binding of the mt33 molecules in the clusters is weak. By reducing the tip-surface distance (by reducing the bias voltage U to 200mV) one can shift mt33 molecules with the tip. Doing this, one can produce mt33 monomers on the Ag(111) surface, but only on the area manipulated with the tip. This method to obtain individual mt33 molecules is only useful for local probe investigation but not for studies using averaging techniques and not at all for applications. A better

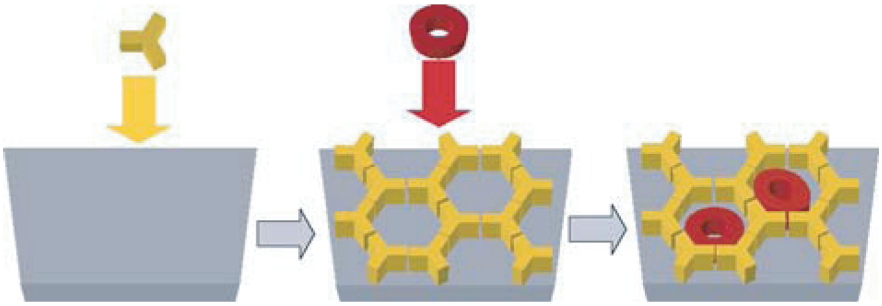

Figure 7.5: Idea of prepatterning a surface to obtain single molecule binding sites.

way to prepare individual molecules might be the adsorption on a prepatterned surface with well defined binding sites which are able to bind a single molecule in a certain binding geometry. For prepatterning of the surface one can use self-assembled supramolecular structures. To achieve this goal the Ag(111) is portioned into an array of identical cavities by the precedent self-assembly of an infinite supramolecular network, namely the *honeycomb structure* made out of BTA molecule described in Chapter 5.2. Similar approaches with different molecules were described recently by other groups [14, 152]. Figure 5.14a and Figure 5.16 reproduce typical STM topographs, showing the supramolecular adlayer self-assembled by BTA molecules on the Ag(111) surface. The BTA *honeycomb structure* contains an array of cavities of 2.95nm inner diameter, which represents an host to accommodate a single mt33 molecules per pore. In a second step mt33 molecules were deposited on top of the hexagonal network covered surface. As a result, isolated single mt33 molecules are confined within the nanometer size cavities of the networks.

STM measurements clearly identify larger species trapped in the *honeycomb structure*, as highlighted by the solid ellipse in Figure 7.6, which occurs exclusively after deposition of mt33. The external size and the ellipsoidal shape indicate that these objects are indeed mt33 molecules. Furthermore the mt33 molecules trapped within the cavities exhibit a central dip, which speaks for a flat adsorption on the surface as described above. As comparison, the dashed circle highlights alternatively a trapped BTA molecule non-included into the *honeycomb structure*, which can be easily distinguished from the macrocyclic molecule mt33. Figure 7.6 reveals further that only single species of mt33 are accommodated per cavity at this particular deposition condition, presumably due to the matching interior size of the cavity with the size of the mt33 molecule. No double inclusion of mt33 was observed

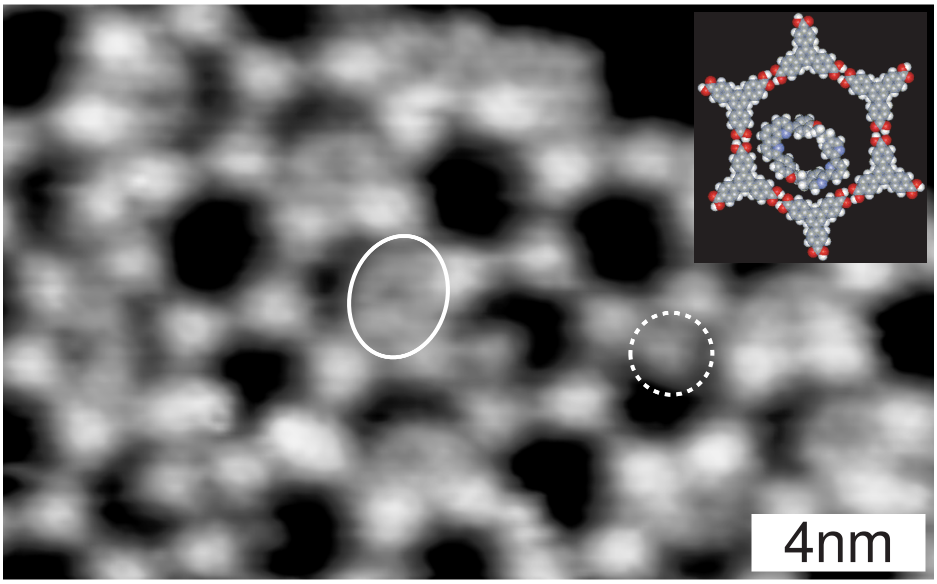

Figure 7.6: Individual mt33 molecules trapped in the cavities of the BTA *honeycomb structure*. The mt33 molecules appear elliptical with a depression in the middle. As the shape is the same as in the mt33 clusters on the pristine Ag(111) surface one can conclude that the mt33 molecules inside the BTA cavities have the same adsorption geometry as on the clean Ag(111) surface. U=1000mV, I=200pA, T=5K)

in any case. In more detail, the STM data reveal also that the molecules are confined eccentrically within the hexagonal cavities, contacting the inner cavity wall which indicates an attraction between mt33 and the inner rim of the cavities. The adsorption geometry with respect to the surface of the mt33 molecules trapped in the BTA cavities does not change much as compared to the one on the pristine Ag(111) surface.

The stability and the response of the sample consisting of mt33 molecules trapped in the BTA *honeycomb network* onto elevated temperature was likewise tested. We annealed such samples to 320K as at this temperature on the pure BTA/Ag(111) sample an irreversible phase transition from the *honeycomb structure* to the *ribbon structure* can be observed. Doing this, we can observe a total separation of the BTA molecules and the mt33 molecules. The BTA molecules aggregate into a *ribbon structure* whereas the mt33 molecules form clusters. No difference to samples with BTA or mt33 on Ag(111), respectively, can be observed. This strongly indicates that the interaction between the two kinds of molecules is negligible.

In conclusion, we have determined the adsorption configuration and the

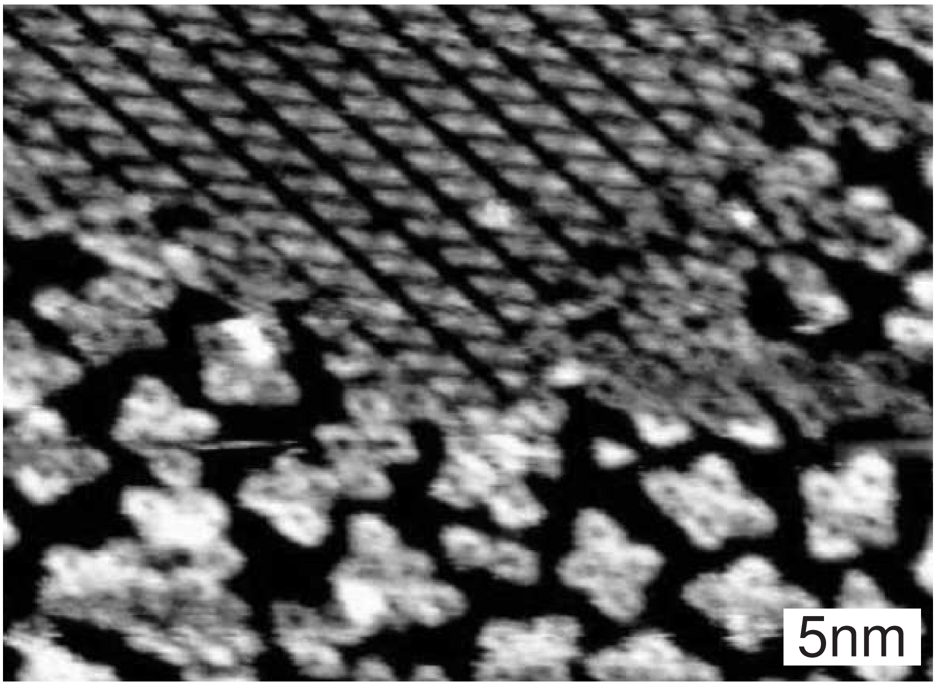

Figure 7.7: After annealing the structure consisting of individual mt33 molecules confined in the cavities of a BTA *honeycomb structure* to 320K one can see a separation into BTA *ribbon structure* and mt33 clusters. (U=2000mV, I=200pA, T=5K)

self-assembly behavior of the macrocyclic molecule mt33 on a Ag(111) surface. The molecules show a high mobility at the surface at 300K but flat adsorption can be determined by STM investigation at 5K. It was shown that the molecules tend to aggregate as preferably dimers and tetramers via inter-molecular C-H$\cdots$N hydrogen bonds of all the *transoid* terpyridine units. In order to achieve isolated grafting of individual molecules, single mt33 molecules were confined inside two-dimensional nanocavities, which were pregrown on the surface by hydrogen bonded self-assembly of BTA molecules. The perfect periodic arrangement of the BTA *honeycomb structure* is transferred to a regular single-molecular array of mt33 molecules. Following the presented concept we are working towards individual grafting of complete catenane or rotaxane molecules at the surface and in the controlled manipulation of their mechanic movements.

Chapter 8

Influence of metal atoms on the self-assembly process of organic molecules

The properties of a surface are given in the idealized case by the orientation of a cut through a perfect bulk crystal with respect to the lattice. The assumption of a perfect surface will of course not be fulfilled in reality. A real crystal cannot be ordered in a perfect way due to dislocations, which will alter the surface structure. Moreover a perfect cut through a crystal is an impossibility, one will always have a misalignment, resulting in a stepped surface. The idealized surface might not be in energetic equilibrium, requiring a reconstruction of the surface which will alter the surface with respect to the corresponding plane in the bulk crystal. A real surface has defects including terraces, steps, kinks , dislocations and reconstructions which cause the properties of a real surface to differ from the properties of an idealized surface in a remarkable way. The influence of such defects is well-investigated on many substrates and they are generally accepted as origin of various properties of a real surface, which cannot be explained within the picture of an idealized surface [153, 154, 155, 156, 157, 158].

Modeling a surface as a static system is also a significant simplification. This assumption is valid at low temperature where one can exclude movement of the atoms. At elevated temperatures, interesting for applications like heterogeneous catalysis, the atoms of the surface are thermally activated and the surface is in a continuous alteration. This not only affects the defects described above, but also creates a new kind of defects not existing in a static surface. At elevated temperatures atoms from step edges can "evaporate" from the steps into a two-dimensional *adatom* gas. [37, 159, 160]. At high temperatures in the order of several hundred Kelvin the coverage of this two-dimensional metallic adatom gas on the terraces can reach several percent of a monolayer and its influence on the properties of the surface might be non-negligible, especially as individual metal atoms should have a high chemical reactivity [34, 35, 36, 38]. This adatom gas can also have an important influence on self-organization processes. Molecules can be synthesized with functional groups to bind metal centers by complex formation. This can be used for the self-assembly of metal-organic coordination networks (MOCNs). The metal centers can have their origin in the native adatom gas of the metal surface, but can also be supplied artificially by depositing metal atoms on the molecular structure [76, 161, 162, 163, 164].

Within the first part of this Chapter we studied the contribution of the metallic adatom gas to the chemical reactivity of a surface, specifically, we studied the deprotonation of carboxylic groups on metal surfaces. In the second part we studied metal-organic coordination networks (MOCNs) with four-fold and three-fold coordinated Fe-centers and used them to study the influence of the surface symmetry on the coordination number of a complex on a surface. In the last part we studied the influence of the native but also artificially generated Cu adatom gas on cat30, a catenane which is capable of trapping a Cu atom in its interior by complex formation.

8.1 Metal-atom triggered deprotonation of 1,3,5-benzenetricarboxylic acid

More than 80 years ago H. S Taylor developed the concept of *active sites* in heterogeneous catalysis. He could show, based on experimental results, that the cleavage or formation of adsorbate bonds preferentially occurs at low coordinated surface atoms [165]. The identification and understanding of this *active sites* is a fundamental basis to get an insight into the functioning of surface reaction mechanisms, especially the rate limiting steps, needed for the design of advanced catalysts with improved efficiency or selectivity [166, 167]. With the improvement of surface science technology and theoretical calculations detailed studies of the structure of the surface of catalyst could be performed, resulting in the identification of *active sites.* Especially structural defects like steps, kinks, vacancies and dislocations could be assigned to centers of increased chemical activity with theoretical calculations revealing the proceeding processes [153, 154, 155, 156, 157, 158, 168, 169].

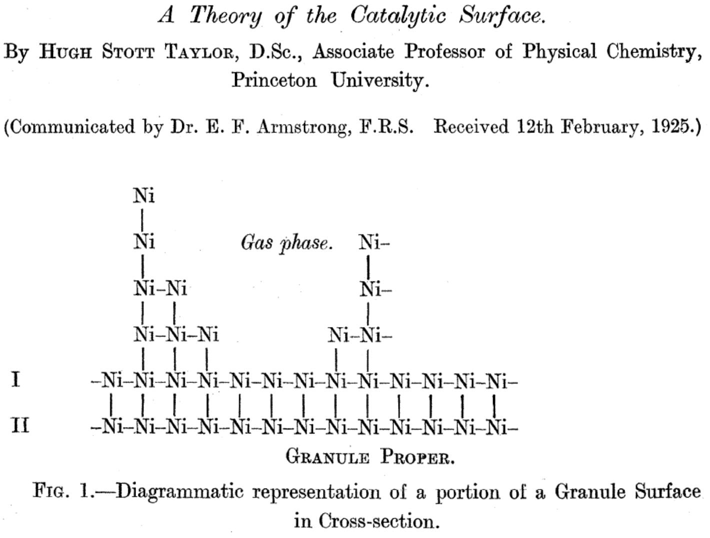

A Theory of the Catalytic Surface.

By Hugh Stott Taylor, D.Sc., Associate Professor of Physical Chemistry, Princeton University.

(Communicated by Dr. E. F. Armstrong, F.R.S. Received 12th February, 1925.)

Fig. 1.—Diagrammatic representation of a portion of a Granule Surface in Cross-section.

Figure 8.1: Extract of the original work of H.S. Taylor, in which he developed the concept of *active sites.*

But all these studies have the disadvantage that they regard the surface as a static arrangement, a constriction which is not fulfilled at the elevated temperatures up to 1000K where real catalysts are usually operated. At this temperatures, there are abiding morphological changes, especially the formation of a highly mobile adatom gas arising from evaporation at step edges. The existence of a two-dimensional lattice gas, formed out of atoms

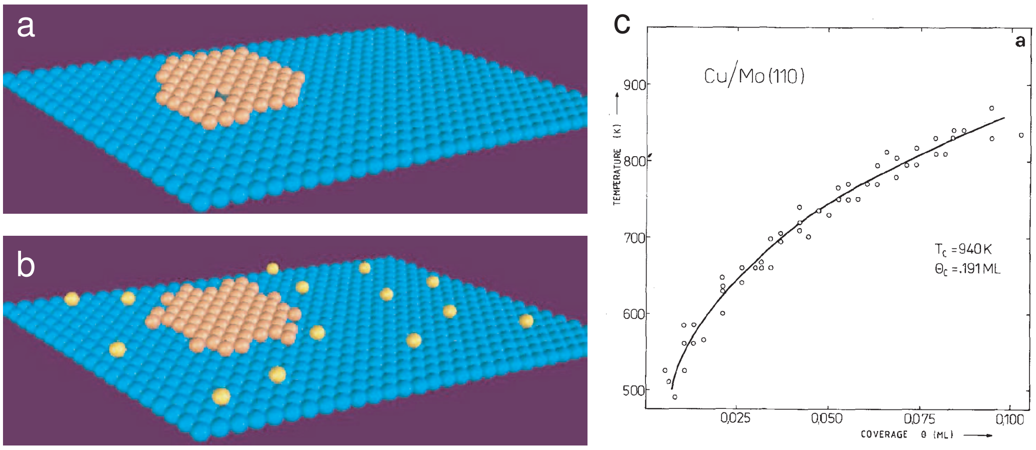

Figure 8.2: **a** Static situation at low temperature. **b** On thermal activation, island edges start fluctuating and emitting atoms from kink sites. A dilute 2D adatom lattice gas exists on the terraces [170]. **c** Phase diagram of coexisting Cu-islands and Cu-adatom gas on Mo(110) at elevated temperatures [38].

evaporated form kink sites of steps upon thermal activation, is an intrinsic property of metal surfaces and plays a decisive role it the formation of reconstructions [171, 172, 173], orientational ordering of adsorbed species and the formation of metallo-organic complexes [161, 76, 162, 163, 164]. The surface concentration of this adatom-gas was studied for a variety of systems and strongly depends on temperature, chemical nature and morphology of the substrate. For the catalytical important metals Pd, Cu and Ag the adatom densities are ranging between 1% and 6% at temperatures of 700K on Mo and W surfaces [34, 35, 36, 37, 38].

As this adatoms have a reduced coordination number compared to eg. atoms at kink sites and minding that lowered coordination number often correlates to an enhanced chemical activity, one can assume that this adatom gas acts as dynamic active sites with extreme efficiency in heterogeneous catalysis. Indeed the dynamic formation of *active sites* was already shown for the catalytic oxidation of CO on Ag(111) [174] and furthermore immobilized individual metal atoms on nonmetallic substrates have been proven to operate as single-site catalysts [39, 40, 41].

To reveal the contribution of the adatom gas on the chemical activity of a metal surface we studied TMA on various substrates as model system. In the previous Chapter 5.1 we showed that on a Ag(111) surface the carboxyl acid groups of the TMA molecules stay intact up to 350K and it requires high temperatures of 420K to deprotonate one out of three carboxyl acid groups, forming a carboxylate group. On the other hand it is reported in literature that TMA on Cu(100) exhibits already at 300K two carboxylate groups and forms after annealing to higher temperature metallo-organic complexes, with all carboxyl acid groups being converted into carboxylate groups [76, 164]. In our combined STM- and XPS-measurements we want to determine the base of the enhanced chemical reactivity of the Cu(100) surface compared to the Ag(111) surface. Special emphasis is laid on the differentiation between the static part (terraces, steps and kinks) and the dynamic part (the adatom gas) of the Cu surface. To do this, we address the chemical activity of the mobile Cu-adatoms and the chemical activity of static defects, like step edges or kinks, separately. As the individual adatoms are highly mobile and cannot be resolved by STM but rather appear as flicker noise, we can not observe the reaction directly but examine well defined initial states and final states of the system. The investigated system is TMA (1,3,5-benzenetricarboxylic acid) on a Ag(111) surface in UHV. As shown in the previous Chapter 5.1, the carboxyl acid groups of the TMA-molecules on Ag(111) are intact up to a temperature of 350K, which is of major importance for our experiment as we have to avoid an influence of the Ag-surface on the TMA-molecule in the temperature range needed for our experiments (up to 300K), as the Ag(111) surface only acts as support material. In the first part of the experiments we want to address the adatom gas. To do this, we prepare on a Ag(111) surface highly dispersed Cu-atoms in an irregular matrix of TMA-molecules. By increasing temperature their chemical activity become apparent, resulting in a fully deprotonation of the carboxylic groups, forming carboxylate groups. In the second part the influence of static defects is studied. This is done by fabricating on a Ag(111) surface Cu-islands embedded in an irregular matrix of molecules. After increasing the temperature only a much weaker chemical activity can be seen, with only a minor amount of carboxylic groups being deprotonated.

All measurements were done under UHV-conditions at a base pressure below $\sim 1 \times 10^{-10}$mbar, with the vacuum systems for the STM- and XPS-measurements being equipped with standard equipment for surface and thin film preparation. TMA was deposited onto the Ag(111) surface again by means of OMBE, whereas Cu was deposited by means of an electron-beam evaporator. The STM-measurements were again made with our home built Besocke-type STM at temperatures of 5K and 300K, respectively. The XPS-measurements were performed at the BESSY 2 synchrotron facility in Berlin at temperatures of 120K and 300K, respectively.

To address the influence of the Cu adatom-gas on the carboxylic groups we prepared on a Ag(111) surface highly-dispersed, individual Cu-atoms embedded in a matrix of TMA-molecules. To prepare such a system, we first deposited TMA-molecules on a Ag(111) surface kept at ∼120K, with TMA-

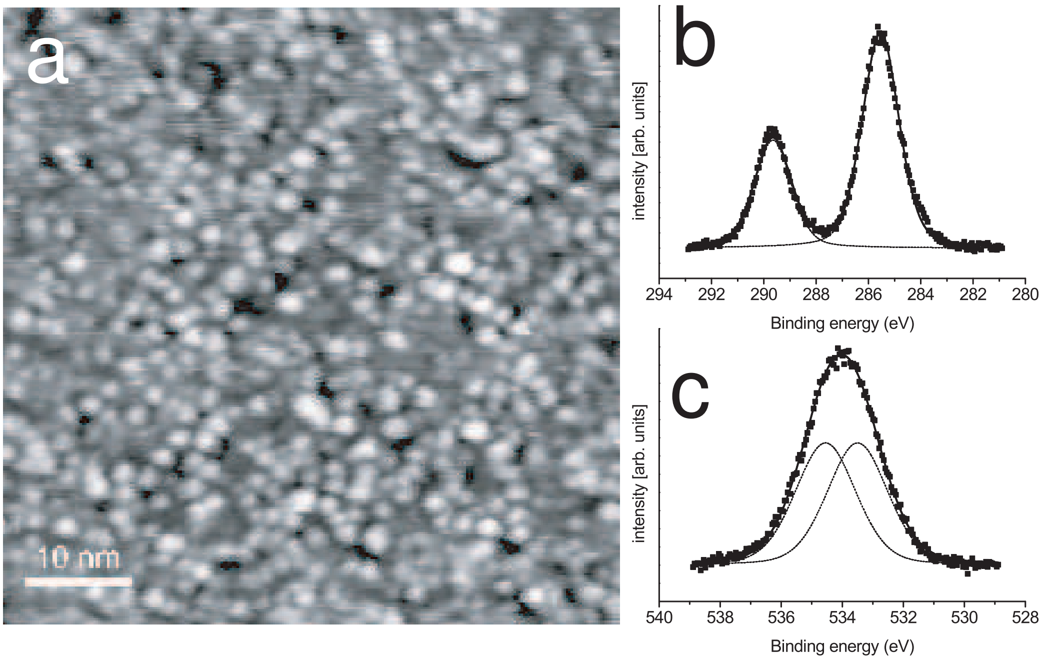

Figure 8.3: **a** STM-topograph of TMA-molecules with codeposited Cu atoms at 120K. One can see disordered TMA islands and no islands of the codeposited Cu atoms can be seen, indicating dispersed Cu-atoms embedded into the TMA matrix. (U=500mV, I=500pA, T=5K)**b** The XP-spectrum of the C 1s signal shows two well separated peaks, assigned to carbon atoms in carboxyl groups and in benzene rings. **c** The XP-spectrum of the O 1s signal shows a broad, symmetric peak. Both the C 1s and the O 1s spectrum indicate intact carboxyl groups.

coverages in the range from ~0.2 monolayer to ~0.5 monolayer. At this low temperature the TMA-molecules are immobilized on the surface [110], thus not forming an ordered honeycomb-structure but rather disordered islands. Without warming up the sample, subsequently small amounts of copper (~0.05 monolayer) were deposited onto this structure. These samples were either transported into the STM (operated at 5K) or XP-spectra were acquired (at a temperature of 120K) without warming up the sample. Although a diffusion of Cu adatoms on the Ag(111) surface and the formation of Cu dimers can already be observed at a temperature of 20K [175] and a temperature of 120K is a typical regime for fractal growth of dentritic metal islands on metal substrates [176] we could see no sign of Cu-island formation in STM-images. This is in agreement with observations of Kalousek et al. which revealed a significant hindering of Co adatom-diffusion due to coadsorbed CO [177]. In accordance with these measurements we suggest a strong hindering of Cu adatom diffusion due to the coadsorbed TMA molecules and conclude that this preparation resulted in individual Cu-atoms dispersed in an irregular matrix of TMA-molecules as evidenced by STM-measurements. The STM-image in Figure 8.3a shows an irregular TMA-island and no adumbration for Cu-islands.

Corresponding XPS-measurements acquired on such a preparation revealed that the TMA-molecules are unaffected from and stay intact due to the Cu-deposition. Figure 8.3b shows the C 1s signal and Figure 8.3c the O 1s signal from such a preparation. The C 1s signal consists of two peaks, a smaller one at a BE of 289.7eV and a larger one at a BE of 285.5eV. In analogy with the XPS-measurements of TMA on Ag(111) at 300K in Chapter 5.1 and consulting literature [75, 86, 87, 88, 89, 90, 91] these peaks have been assigned to carbon in carboxyl groups and in benzene rings. The areas of the peaks indicate intact TMA-molecules. The O 1s signal consists of a broad symmetric peak which is a convolution of the signals of oxygens in hydroxyl groups (BE of 534.6eV) and in carbonyl groups (BE of 533.5eV), similar to the TMA *honeycomb structure* in Chapter 5.1 and other systems bound by hydrogen bonds between carboxylic acid groups reported in literature [75, 87, 88, 89]. The C 1s and O 1s XP spectra clearly show that after depositing Cu atoms onto the TMA molecules at 120K the carboxylic groups of the TMA molecules were still protonated. The chemical activity of the Cu-atoms could be stimulated by increasing the substrate temperature. From our experiments on TMA on Ag(111) in Chapter 5.1 we know that in the temperature range from 250K to 340K a *honeycomb structure* is formed. Furthermore, it is known that TMA on Cu(100) forms at temperatures below 280K a *honeycomb structure* and annealing at temperatures higher 280K results in an irreversible phase transformation, connected to the

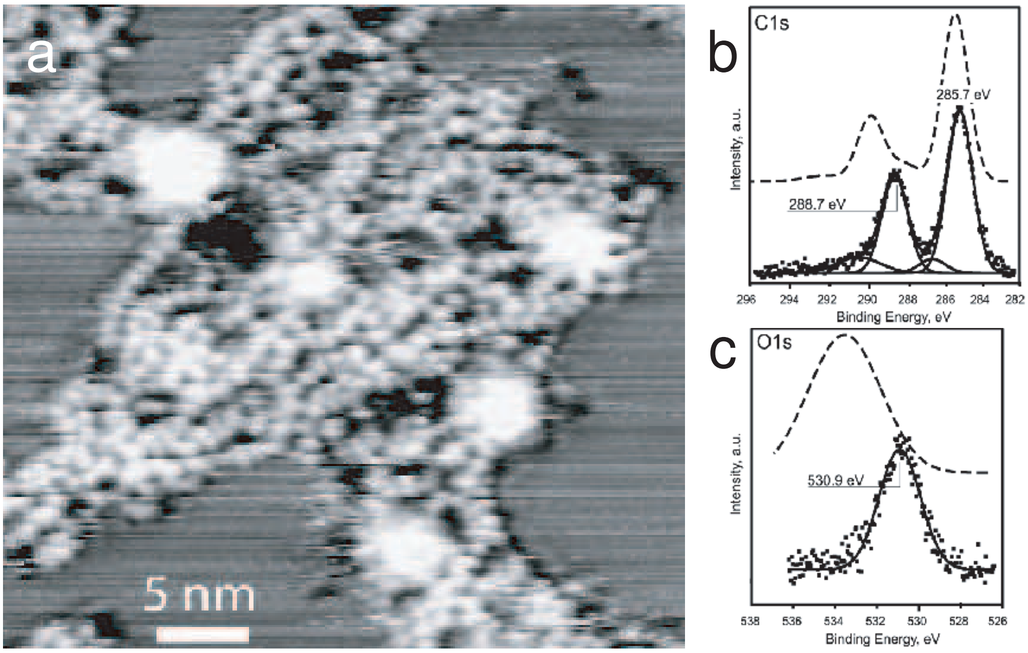

Figure 8.4: **a** STM-topograph of the intermixed TMA/CU layer after stimulating the chemical activity of the Cu-atoms by annealing to 300K. One can identify disordered TMA islands with embedded Cu-islands. No *honeycomb* structure could be found on the surface after this preparation, indicating an altered bonding motif of the TMA molecules. (U=500mV, I=500pA, T=5K) **b** The XP-spectrum of the C 1s signal consists of two peaks, one for carbon atoms in carboxylate groups and one for benzene rings. No carbon in carboxylic groups could be identified. **c** The XP-spectrum of the O 1s signal shows only a narrowed peak, assigned to oxygen atoms exclusive in carbonyl groups, indicating a tricarboxylate species. The dashed lines are the C 1s and O 1s spectra before annealing.

formation of carboxylate groups. A reaction of the TMA molecules due to the coadsorbed, single Cu Atoms at a temperature of 300K can therefore only be ascribed to the influence of the Cu-atoms, but not to the Ag(111) surface. The expected reaction of the TMA molecules onto the Cu atoms is a partially or fully deprotonation of the carboxylic groups. The deprotonation of carboxylic groups is very easy to detect in both the STM-images, as the carboxylic groups act as linkers between the molecules and a deprotonation must go hand in hand with a structural transformation similar to Chapter 5.1, and the XPS-measurements of the C 1s and O 1s signal of the structure, again similar to Chapter 5.1. While the details of the respective processes could not be elucidated with our experimental means, in view of their dynamic behavior involving rapid chemical transitions and structural reorganizations in the adsorbed layer, the final state could be conclusively addressed. The final state of the process showed drastic distinctions to the *honeycomb structure* formed of intact TMA molecules.

The analysis of the XPS measurements clearly showed the deprotonation of all carboxylic groups of the TMA molecules and the formation of a tricarboxylate species. The XPS chemical shifts shown in Figure 8.4b and Figure 8.4c clearly reveals the formation of a tricarboxylate species at 300K. This complete deprotonation of the carboxylic groups is associated with the presence of the Cu adatoms. In the C 1s signal shown in Figure 8.4b the peak associated to carbon in carboxyl groups, at a BE of 289.9eV, disappeared completely and was replaced by a peak associated to carbon in carboxylate groups, at a BE of 288.7eV. In the O 1s signal shown in Figure 8.4c the broad symmetric peak at a BE of 533.2eV is replaced by a narrowed peak at a BE of 530.9eV. This narrowed peak reflects the two equivalent oxygen atoms in a carboxylate moiety. This findings are substantiated by STM topographic data. The STM-data shown in Figure 8.4 reveal a complete inhibition of the TMA *honeycomb structure* formation, since the underlying hydrogen-bonding motive is absent. Instead the deprotonated TMA-molecules aggregate in disordered agglomerates containing bright protrusions, which are Cu-islands formed during the annealing process. This formation of Cu-islands reflects appreciable mass transport and a movement of the Cu-atoms. Since carboxyl groups are still present after the Cu deposition prior to sample annealing, it is concluded that the deprotonation reaction is not triggered by the impact of Cu in the deposition process, rather it must be mediated by thermal activation and Cu adatoms during warming. The corresponding temperatures are in a range for which recombinative desorption of molecular hydrogen occurs (on Ag(111) at T=190K [178]), a process which is similarly believed to be operative in the present scenario.

Furthermore, several experimental results hint that the observed depro-

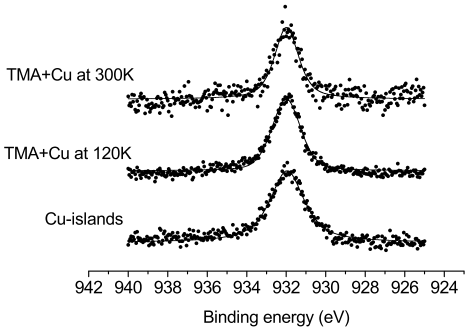

Figure 8.5: XP-spectra of the Cu $2p_{3/2}$ peak, acquired before and after the deprotonation process. As a reference the spectrum acquired on Cu-islands on clean Ag(111) is given. No indication for the formation of Cu(II) species could be found in the spectra.

tonation reaction is a catalytical process. A fundamental assumption for a catalytic process is that the catalyst, in this system the Cu adatoms, is not consumed during the reaction. In our experiments we varied the TMA coverage from ∼0.2ML to ∼0.5ML while keeping the Cu coverage almost constant at ∼0.05ML. The amount of Cu condensed in islands proved to be independent of the TMA coverage and corresponded to the quantity of Cu deposited on a clean Ag(111) surface. This demonstrates that no consumption of Cu atoms during the deprotonation reaction takes place. Furthermore, in XP-spectra of the $Cu2p_{3/2}$ signal made before and after the reaction of the TMA-molecules with the Cu atoms no evidence for Cu(II) species could be found. Also no Cu-TMA complexes could be observed in STM-images, in contrast to results made under similar conditions with TMA on the Cu(100) surface [164, 179, 180]. These metallo-organic complexes have very characteristic supramolecular patterns, which should be easy to see in STM images. Instead we only see rather irregular TMA protrusions. Consequently, the Cu active sites are not consumed in the deprotonation reaction in the form of metallo-organic complex formation. All these results indicate that the Cu-adatoms indeed are active sites in a catalytic process.

One could now claim that not the Cu adatom gas itself acts as dynamic *active sites* in the deprotonation process of the carboxylic groups, but that instead the Cu islands formed during the annealing process to 300K Cu act as static *active sites*. Therefore in a second step the potential chemical reactivity of static *active sites*, like steps and kinks of Cu islands, was addressed to clarify if the Cu-adatoms are responsible for the deprotonation of the carboxylic

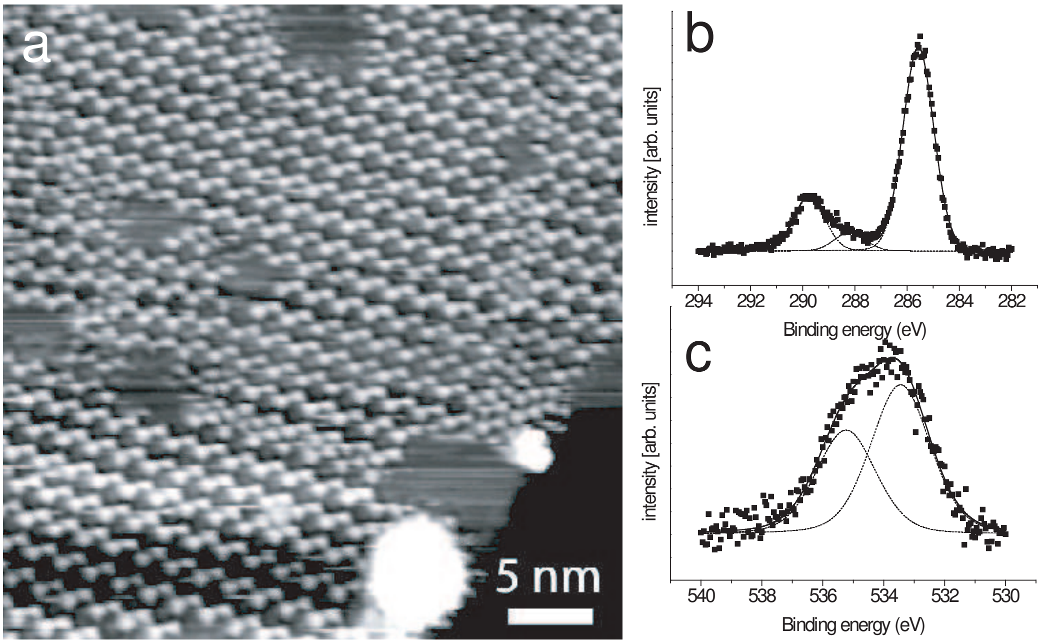

Figure 8.6: **a** STM and **b** and **c** XPS data showing the chemical activity of Cu islands. In the STM topographs mostly a TMA *honeycomb* structure can be identified, indicating intact TMA molecules. The XPS spectra show that only a minor amount of the carboxylic groups was transformed into carboxylate groups. The effect of predeposited Cu-islands on the deprotonation of the carboxylate groups of the TMA molecules is, compared to the influence of the single adatoms, negligible. (U=500mV, I=500pA, T=5K)

groups or Cu islands formed during the annealing process. To perform such a control experiment with Cu islands, the same amount of Cu as in the previous experiments was deposited on a Ag(111) surface at 300K, circumstances under which Cu islands are formed. The sample was then cooled to 120K and TMA was deposited. This preparation results in Cu islands embedded into an irregular matrix formed out of intact TMA molecules. To initiate the chemical activity of the Cu islands on the deprotonation process of the carboxylic groups of the TMA molecules the sample was again warmed up to 300K. In STM images acquired on such a preparation, shown in Figure 8.6a, a perfect *honeycomb structure* coexisting with the Cu islands can be observed. The underlying hydrogen bonding implies that no deprotonation of the carboxylic groups of the groups occurs in the presence of pregrown Cu islands, with the possible exception of molecules at step edges.

This picture is endorsed by complementary XPS measurements performed at such a preparation, shown in Figure 8.6b and c. The C 1s signal of this preparation is shown in Figure 8.6b. Again two clearly discriminable peaks can be identified, a smaller one assigned to carbon in carboxylic groups in agreement with our previous measurements (BE of 288.6eV) and a larger one assigned to carbon in benzene rings in agreement with our previous measurements (BE of 284.5eV). Like in the partial deprotonation of the carboxylic groups in Chapter 5.1, the fit of the signal could be improved by adding a third peak, again assigned to carboxylate groups, at a BE of 287.1eV. The ratio of carboxylate groups to carboxylic groups is 0.35. The O 1s signal shown in Figure 8.6c does not show a symmetric, broad peak, but has to be fitted by two unequal Gaussians, similar to the partial deprotonation in Chapter 5.1. Both XP-spectra show that most of the carboxylic groups are still intact, with only a minor amount deprotonated, thus forming carboxylate groups. The same behavior was encountered with pregrown Cu islands in control experiments in which TMA was codeposited at a substrate temperature of 300K. Also in this sample a *honeycomb structure* was fabricated, as would occur on a clean Ag(111) surface at the same temperature

The minute reactivity reflects the fact that the 2D adatom concentration in the presence of Cu islands at 300K is much smaller than in the highly dispersed state obtained by low-temperature deposition in an organic matrix. Only at elevated temperatures a two-dimensional Cu gas with appreciable density can be expected, but in the present system the chemical activity then comes into play. Moreover, in TMA deposition at elevated temperatures both high molecular diffusivity and rotary motions may interfere. The major difference between the two scenarios is that in the first case TMA molecules experience an environment of Cu adatoms whose density is much higher than that of a two-dimensional condensed submonolayer Cu/Ag(111) system. Hence the mobile Cu adspecies have a high probability of coming into contact with the carboxyl groups during the warm-up phase, before they eventually aggregate into Cu islands. By contrast, in the second case the Cu adatom density is in thermodynamic equilibrium with the Cu islands and thus much smaller (the two-dimensional vapor pressure is minute in the employed temperature range of 120K to 300K), hence the probability that deprotonation of postdeposited TMA can be mediated by mobile active sites is strongly reduced. Notably, the atomic steps of the Cu islands themselves also do not interfere in a significant way. The sharp distinction between the two cases must be associated with drastically decreased chemical reactivity. Consequently, the deprotonation rate depends on the Cu adatom density and Cu adatoms are the decisive element in mediating carboxyl group deprotonation, that is, this mobile species is the true *active site* in this surface chemical reaction.

Our findings reveal that adatom *active sites* interfering in a surface chemical reaction my be decisive for reaction pathways and formation of final products. Many catalytic surface reactions are run under reaction conditions for which the density of the intrinsic two-dimensional adatom gas of a catalytically active metal is in the percent range. It is likely that these highly mobile atoms are not only the *active sites* in the observed deprotonation reaction but also promote many other elementary processes. Our observations thus suggest that thermally activated formation on mobility of *active sites* is of general relevance in surface chemistry and may bestow a dynamic heterogeneity on catalysts.

8.2 Metal-organic coordination as supramolecular bonding motif

Using complex formation in coordination chemistry, it is possible to fabricate not only finite compounds, but with suitable ligand molecules one can even generate infinite one-, two- and three dimensional networks [181, 182, 183, 184, 185, 186]. These concepts of coordination chemistry have been successfully applied toward the design of surface-supported metal-organic coordination polymeric structures, with a non-negligible influence of the surface onto coordination number and geometry of the formed complexes [42, 43, 44, 45]. In particular, infinite two-dimensional metal-organic coordination networks (2D-MOCN), patterning the surface down to the nanometer scale with lattice parameters predetermined by the backbone length of the ligands, could be fabricated on metal surfaces [46, 47, 48, 49].

The question we want to address within this chapter is the influence of the surface on the coordination number and thus the geometry of the formed 2D-MOCN. To do this, we altered both the substrate material and the substrate symmetry. The surfaces used for our experiments were Cu(100) and Ag(111). On both substrates two different 2D-MOCN with a different coordination number were fabricated, with Fe as metal center in both cases and 1,4-benzoicdicarboxylic acid (terephtalic acid, TPA) or 4,4′-Dihydroxybiphenyl (DHBP) molecules as ligands. We can show that, independent of substrate symmetry or material, the Fe centers in the TPA+Fe system have a coordination number of of four whereas the Fe-centers in the DHBP+Fe system have the rare coordination number of three.

All experiments have been performed under UHV conditions at a base pressure below $\sim 1 \times 10^{-10}$mbar. The Cu(100) and the Ag(111) surface were cleaned by repeated cycles of sputtering with 500eV Ar^+ ions and subsequent annealing to 800K and 850K, respectively. The TPA molecules (>98%, Aldrich) and the DHBP molecules (>98%, Fluka Chemie) were deposited onto the pristine substrates kept at 300K by means of OMBE, with the crucible containing the molecules kept during deposition at temperatures of 440K and 415K, respectively. Ensuing, Fe atoms were deposited on the so obtained samples kept at a temperature of 400K by means of electron beam evaporation with a flux in the range of a few percent of a monolayer per minute. After the metal deposition the samples were heated to 400K-430K to promote network formation. The subsequent STM-measurements were performed at a temperature of 300K using electrochemically etched W-tips.

STM-pictures of the so obtained 2D-MOCN using TPA-ligands on the Cu(100)-surface and the Ag(111) surface are shown in Figure 8.7a and 8.7b,

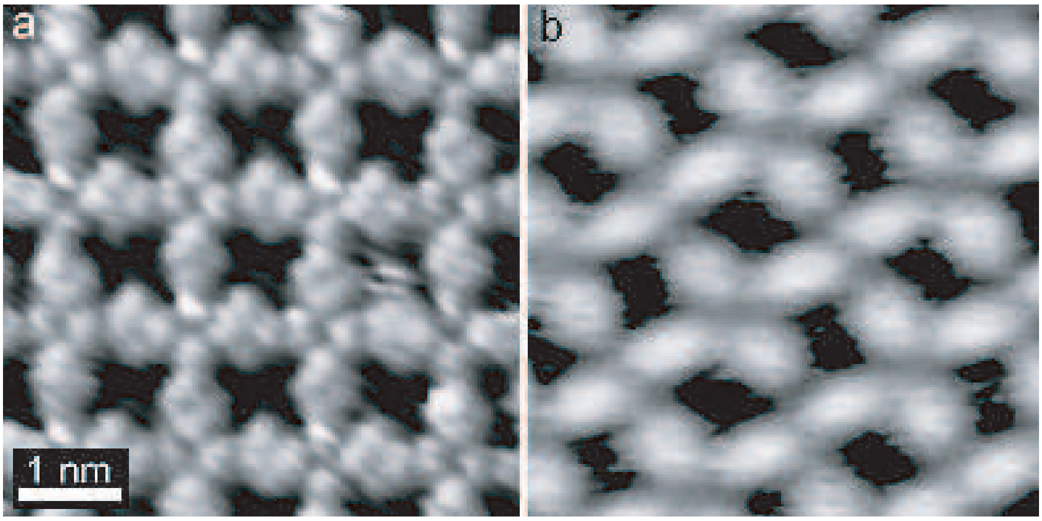

Figure 8.7: STM topographs of the rectangular 2D-MOCN made of Fe center atoms and TPA ligands on **a** Cu(100) [47] and **b** Ag(111). The four-fold coordination motif is abide on both the four-fold (100) Cu substrate and the three-fold Ag substrate. Both images have the same length-scale. (U=500mV, I=300pA, T=300K)

respectively. On both substrates, the four-fold Cu(100) surface and the three-fold Ag(111) surface, we find the same four-fold bonding motif of the 2D-MOCN, resulting in a rectangular structure, indicating that substrate symmetry does not alter the coordination bonding motif. The orthogonal binding mode can be explained by the coordination between a dinuclear iron center and four carboxylate ligands as shown in Figure 8.8. A more profound and general analysis of TPA-Fe networks on Cu(100) can be found in [47].

Obviously, it is not possible to alter the coordination binding motif by changing the substrate symmetry. To construct a hexagonal 2D-MOCN, one would need a three fold binding motif. Deplorable, trigonal coordination geometries, necessary to obtain hexagonal networks, are not very common in conventional coordination chemistry [187, 188, 189]. By utilizing Fe-phenolat coordination we could show that on a surface three-fold coordination can be realized. This demonstrates that surface assisted assembly of coordination complexes can introduce novel coordination configurations and opens new avenues of coordination chemistry.

STM-pictures of the networks obtained by self-assembly of DHBP-ligands and Fe-atoms on the Ag(111) surface are shown in Figure 8.9 and on the Cu(100) surface are shown in Figure 8.11. On both substrates, one can identify hexagonal networks, having a three-fold symmetry. In contrast, the

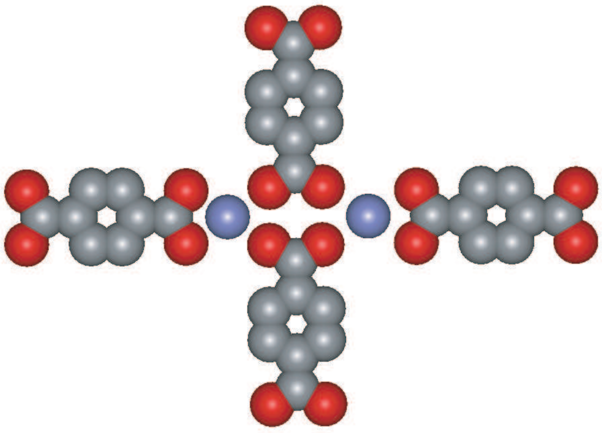

Figure 8.8: Schematic model of the four-fold binding motif of carboxylate coordinated dinuclear Fe

structures formed by DHBP on Cu(100) and Ag(111) without Fe-atoms show a two-fold symmetry.

Figure 8.9a shows an STM topograph of the hexagonal DHBP+Fe structure on the Ag(111) surface. Within the three-fold network, there exist two types of cavities, as indicated by *T* and *C* in Figure 8.9b. The *T*-type cavities posses a C_3 symmetry, while the *C*-type cavities are compressed in one direction. The domains can grow continuously over the entire terraces of the Ag(111) surface, frequently exceeding diameters of 100nm, as illustrated in Figure 8.9a, where two domains with different orientations, as indicated by the arrows, enclose an angle of $14.5° \pm 1°$. The domain boundary (marked by the dashed line) comprises distorted hexagons as well as heptagon-pentagon lattice faults. The *C*-hexagons tend to align in straight rows that go through a single domain, as indicated by the arrows in Figure 8.9b. Occasionally, two *C* can cross each other and various deviations from the two major types of hexagons (*T* and *C*) occur at the intersections. A hint for the emergence of the two different types of cavities was supplied by STM-measurements at various coverages. At a relative low coverage, when the surface is not fully occupied by the network, the *T*-type cavities are predominant. The *C*-type hexagons evolve at a full adlayer and the lack of open space leads to a compression of the structure. Presumably, when the network saturates the surface the more open *T*-type hexagons are compressed, forming the *C*-type hexagons.

Figure 8.9b shows a high-resolution STM topograph of the DHBP+Fe structure on the Ag(111) surface. A structural model is superimposed to

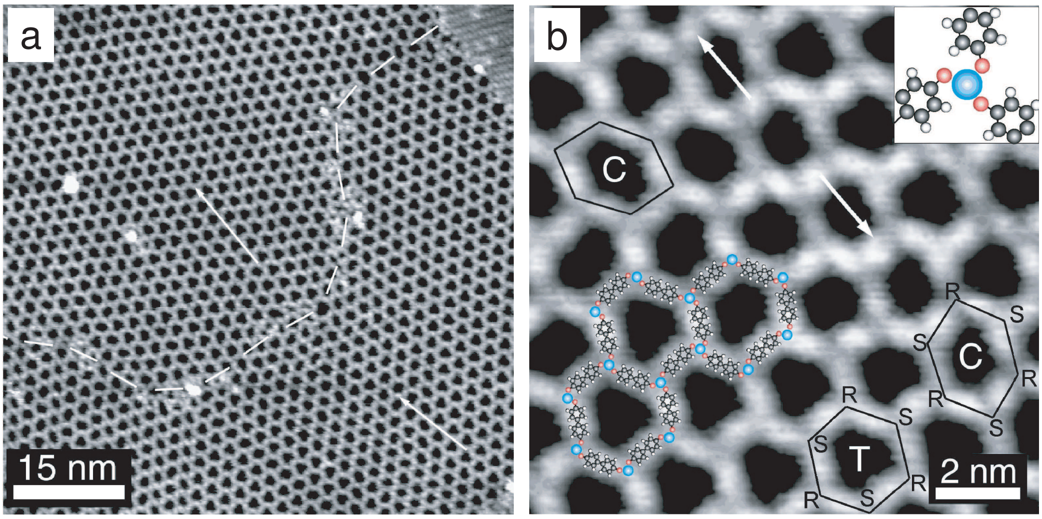

Figure 8.9: STM topographs of the hexagonal 2D-MOCN assembled on Ag(111). **a** Overview STM image showing that two domains are separated by a clear domain boundary (dashed line). The white arrows mark the domain orientation. **b** High-resolution STM image of the network. A structure model is superimposed on the STM-data (Color code: Fe in blue, O in red, C in grey and H in white). The inset shows a model of the trigonal Fe-phenolat coordination. Black frames highlight the shape and orientation of the *T*- and *C*-cavities. The two white arrows indicate a row consisting of *C*-cavities. *R* and *S* denote the clockwise and counter-clockwise arrangement of the ligand molecules around the Fe-centers. (U=500mV, I=300pA, T=300K)

the STM-image to deduce the coordination configuration. In this model, it is assumed that the DHBP molecules adsorb with the aromatic rings parallel to the substrate surface and there is no distortion of the molecules in comparison with those in the gas phase. XPS-measurements of DHBP on Cu(100) annealed to 380K, performed by Sebastian Stepanow (Fig. 8.10), reveal fully deprotonated hydroxyl groups, similar to the related carboxylic acids [75, 76, 191, 192, 193]. The XPS O 1s spectrum of this preparation consists of a single peak at a BE of 530.7eV with a FWHM of 1.48eV. The FWHM of the peak accords with the FWHM of the individual peaks in our measurements on TMA in Chapter 5.1, showing that only one species of oxygen exists in the DHBP-molecules. The BE of the O 1s peak is in accordance with measurements of phenol on Pt(111), in which oxygen in phenolate groups was identified at a BE of 530.1eV [220], clearly showing the deprotonation of the phenyl groups in the DHBP-molecules upon adsorption on Cu(100) at a temperature of 380K. It is known that deprotonation of phenyl

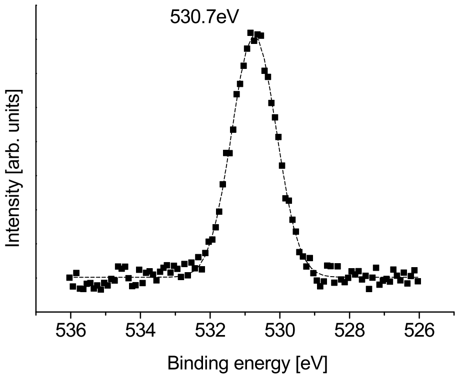

Figure 8.10: XPS O 1s spectrum of DHBP on Cu(100) after annealing to 380K. The O 1s spectrum consist of a single peak with a FWHM of 1.48eV at a BE of 530.7eV, which shows the complete deprotonation of the phenyl groups of the DHBP-molecules into phenolate groups.

groups is not likely to occur on the Ag(111) surface [194], but the chemical activity of the adatom gas of the codeposited Fe may play a significant role in the deprotonation process, as shown for the more acidic carboxylic groups in Chapter 8.1 and in [80, 163].

The model shown in the inset in Figure 8.9b demonstrates how the Fe central-atom is coordinated by the oxygen atoms of the three surrounding phenolat groups in a trigonal-planar configuration. The O-Fe-O angles of the *T*-hexagons amount to 120°, as expected for a perfect honeycomb. For the *C*-cavities, the angles can deviate by approximately 20° from 120°. The Fe-O distance amounts to 0.2nm±0.03nm. It should be noted that the given distances and angles represent only tentative values due to the uncertainty of the positions of the DHBP molecules and the Fe atoms onto the substrate in our modelling, as we could not resolve the complex structure and the atomic lattice of the Ag(111) substrate simultaneously. As illustrated in the model, the ligands do not point directly towards the central Fe atom, but are tilted in the same orientation around the Fe center. Therefore the ligands fold around the central Fe atom either clockwise (*R*) of counter-clockwise (*S*), which creates two-dimensional chirality [179, 195]. Both the *T*-type and the *C*-type hexagons possess alternately arranged *R*- and *S*-units (-*RSRSRS*-), as indicated in Figure 8.9b. The overall ratio of the two enantiomeric chiral centers is balanced, so globally the system is a two-dimensional racemate.

Figure 8.11a shows an overview STM topograph of the DHBP+Fe structure on the Cu(100) surface. Generally, one can identify a very similar net-

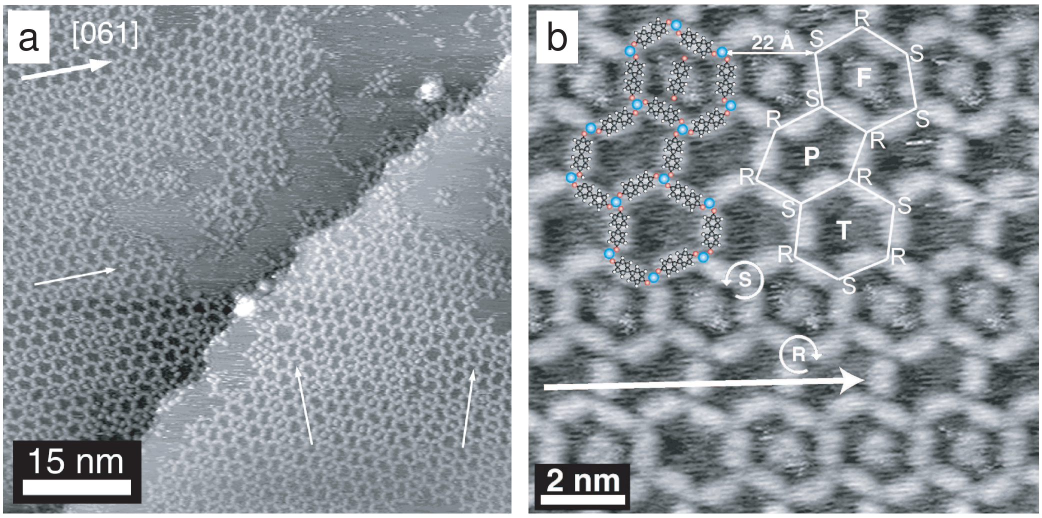

Figure 8.11: STM topographs of the hexagonal 2D-MOCN assembled at Cu(100). **a** An overview STM topograph showing three different oriented domains. They have smaller domain size compared to the 2D-MOCN formed on Ag(111), reflecting a modified influence of the Cu surface to the Ag(111) surface. **b** High-resolution STM image of the network. The arrow marks the *HS*-direction on the Cu(100) substrate. The periodicity length of 2.2nm along the *HS*-direction is noted. The white polygons highlight the *P*-, *F*- and *T*-cavities. A structure model of the coordination bonding motif is superimposed on the STM data (same colorcode as in Figure 8.9). The chiral Fe-centers enclosing the three different kinds of cavities are marked. (U=500mV, I=300pA, T=300K)

work as on the Ag(111) surface, molded by the same three-fold bonding motif. Figure 8.11b reproduces a high-resolution STM picture of the network on Cu(100), where a structure model is superimposed on the STM-topograph. Similar to Ag(111) the model suggests that the Fe central-atom is coordinated by three oxygen atoms of the surrounding deprotonated DHBP-ligands in a trigonal-planar configuration. The Fe-O distance is 0.2nm±0.03nm, as on Ag(111). The O-Fe-O angles are significant altered compared to the Ag(111) substrate, with one being 110°±5° and the other two being 125°±5°. The nearest-neighbor Fe-Fe distance is 1.27nm±0.05nm. Note that all these values are coarse numbers, as the registration of the DHBP-molecules and Fe atoms on the Cu(100) substrates is not known due to a lack of STM images showing the network and the atomically resolved substrate simultaneously.

In the two-dimensional network a strict periodicity of 2.2nm is only observed in one direction, marked in Figure 8.11b with an arrow and labeled as high-symmetry (*HS*) rows. In the STM-topographs three different kinds of *HS*-rows, distinguishable by the cavities forming the *HS*-rows, can be identified. One type of cavity, called *T*-cavity, consists of exiguously distorted hexagons with almost C_3-symmetry, whereas the other two types of cavities, called *F*- and *P*-cavity, have a low-symmetric, parallelogram-like shape, as marked in Figure 8.11b. The three types of *HS*-rows occur with the same probability. Comparable to the network on the Ag(111) substrate, the DHBP-ligands fold around the Fe center-atoms either clockwise (*R*) or counter-clockwise (*S*). The three different kinds of cavities do not only differ in shape, but also in the arrangement of the *R*- and *S*-centers. The *T*-type cavities consist of a alternating arrangement of *R*- and *S*-centers (-*RSRSRS*-), the *F*-type cavities of an alternating arrangement of one *R*- and two *S*-centers (-*RSSRSS*-) and the the *P*-type cavities of an alternating arrangement of two *R*- and one *S*-centers (-*RRSRRS*-). Another difference to the network on Ag(111) is the large amount of cavities embedding single DHBP-molecules. A statistical analysis showed that most (74%) of the *F*-type cavities are filled with single DHBP-molecules, whereas the *T*- and *P*-type cavities have a much lower filling ratio (10% and 3%, respectively). The reason for the different filling ratios is not enlightened. A possible explanation might be that the *F*-type cavities are stabilized by hydrogen bonds between the hydroxyl groups of the embedded molecules and the inner rim of the cavity.

Along the direction perpendicular the *HS*-rows, the three types of *HS*-rows do not form any periodic superstructure, however certain rules are obeyed. For instance *P*- or *F*-row always adjoin to other types of rows and also the vast majority of the *T*-rows adjoins to other type of rows. This specific behavior in the alignment of the rows can be explained by the chiral nature of the coordination centers. As shown in Figure 8.11b, the boundary between two adjacent rows consists of alternating *R* and *S* units arranged in a zigzag manner. This configuration excludes a self-engagement between two *P*-rows or two *F*-rows, but demands apart from the *T*-rows an alternating arrangement of *F*- and *P*-rows.

Overall, we observed four different *HS* row directions (three are visible in Figure 8.11a and marked by arrows), which are related to each other by rotation and mirror symmetry operations to the Cu(100) surface symmetry point group. The *HS*-row orientation can be assigned to the [061] and equivalent substrate directions. The domain size is significantly smaller than those formed on the Ag(111) substrate. Despite the identical coordination bonding motif, the networks formed at the two surfaces differ in the shape and organization of the cavities, the existence of different rotational and mirror domains and the domain sizes. We attribute these differences to the substrate template effects caused by the preferred adsorption sites of the DHBP-molecules and Fe-atoms onto the substrate atomic lattice. This effect becomes more significant on the Cu(100) surface due to the mismatch between the three-fold coordination geometry and the four-fold substrate lattice. In particular, the measured periodicity of 2.2nm along the *HS*-rows corresponds to identical binding sites, presumably hollow sites, of the Fe-atoms on the Cu(100) substrates, which may facilitate the growth of the *HS*-rows. Perpendicular to the *HS*-rows the Fe-atoms of a perfect three-fold hexagonal network cannot adsorb on the same preferred binding sites of the four-fold substrate. Therefore, the cavities are deformed and the *HS*-rows are arranged in the observed configuration in order to optimize the adsorption energy.

In conclusion, we have fabricated two-dimensional MOCNs expressing rectangular and hexagonal topologies according to the specific coordination bonding motifs. In particular we have shown that a planar three-fold coordination can be achieved by coordination chemistry between Fe-center atoms and deprotonated hydroxyl functions. The networks formed at the two substrates, Ag(111) and Cu(100), show identical bonding motifs. This strongly indicates that it is the metal-ligand interaction that determines the network topologies, but not the substrate symmetry.

8.3 Metal-atom triggered alteration of catenane structures

Catenanes and rotaxanes are molecular architectures containing interlocked or threaded rings [196, 197, 198, 199, 200, 201]. The components of these architectures can change their relative position under external stimulus, making these systems particularly promising for application as *molecular machines*, such as mechanical or electronic devices [202, 203, 204, 205, 206, 207, 208, 209, 210]. The envisaged exploitation of these molecules anchored to a metal substrate represents a crucial step towards realizing the concept of *molecular machines* grafted on a solid support [33, 211, 212, 213, 214]. Adsorption of these molecules on a surface allows surface assisted self-assembly as well as *in situ* observation of stimulated mechanical processes at a single-molecule level using advanced surface science techniques [33]. It is thus important to understand the behavior of these molecular species upon adsorption on solid surfaces, e.g. adsorption strength, conformation relaxation, mobility on the surfaces and freedom of mechanic circumrotational switching [33, 213, 214, 215, 216].

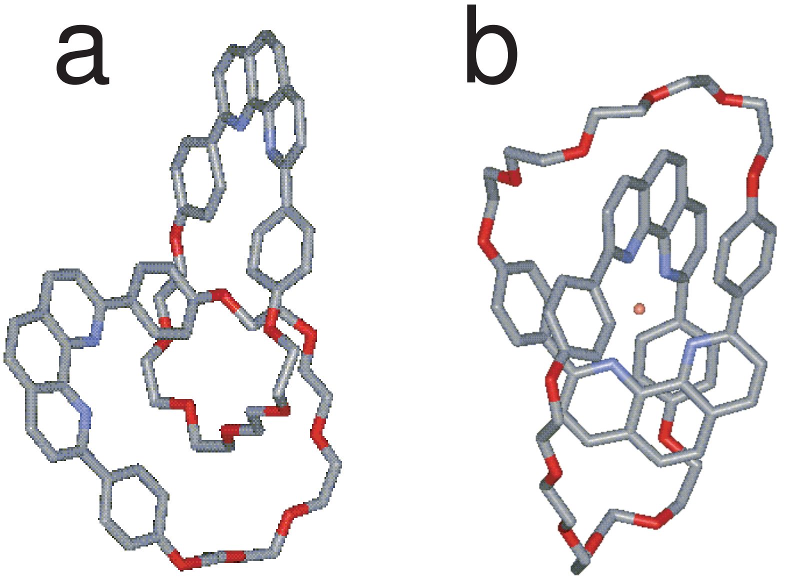

Figure 8.12: **a** Structural model of the cat30 catenane **b** Structural model of the cat30 metallo-catenate incorporating a Cu^{I} atom. Both structures were derived by X-ray diffraction experiments described in [218]

We studied the cat30 catenane and the cat30 metallo-catenate incorporating a Cu^I ion, adsorbed on Ag(111) and Cu(100). The cat30 catenanes are built up by two rings which consist of a phenanthroline group with N-atoms and a pentaethyleneoxy chain with O-atoms. The cat30 metallo-catenate is built up by the very same two rings with the addition of a Cu^I ion incorporated in the interior of the molecule. The Cu^I ion is bound to the N-atoms of the phenanthroline groups via complex formation. The details of the synthesis and the bulk-phase structures can be found in [217, 218].

The main ambition of our experiments was to determine if the cat30 molecules could be deposited by sublimation without thermal fragmentation and if cat30 molecules adsorbed onto a metal surface can react with Cu-atoms to form a cat30 metallo-catenate with an incorporated Cu^I ion. As this reaction is connected with a change in the shape of the molecules, this would be an experimental confirmation of the concept that catenanes adsorbed onto a metal surface can work as molecular machines.

The structures of the cat30 catenane and the cat30 metallo-catenate in crystalline bulk as derived from X-ray diffraction experiments are shown in Figure 8.12a and b [218]. The crystal structure of the pristine cat30 molecules contains benzene and water molecules, which are used as solvent and are not shown in the figure. There is a significant difference in the shape of the two molecules. In the cat30 metallo-catenate, the incorporated Cu atom is bound by a complex formation to the four nitrogen atoms of the two phenanthroline groups. The rings are not planar, the phenyl groups are tilted out of plane. In the cat30 catenane the two diphenyl phenanthroline fragments are totally disentangled and the rings are almost planar.

These structural differences induce different binding behaviors on the surface. In the pristine cat30 molecule, the nitrogen- and oxygen-atoms binding sites are unoccupied and can participate in intermolecular bindings. A change of molecular shape with respect to the crystalline structure upon adsorption on a metal surface cannot be excluded, as the interaction between the two rings of a molecule can be expected to be rather weak. In the cat30 metallo-catenate the N-atoms are involved in a complex formation with the Cu^I-ion and are therefore not expected to participate in intermolecular binding. Due to the different shapes and binding motifs of the pristine cat30 molecules and the cat30 metallo-catenate, one can expect that the two molecules will form different structures when adsorbed onto a surface. This alteration in the formed structure was used in our experiments to detect a reaction of the cat30 molecules with Cu atoms.

All experiments were performed under UHV conditions at a base pressure smaller than 2×10^{-10}mbar. The vacuum system was equipped with all standard equipment for sample cleaning and preparation. The Ag(111)- and the

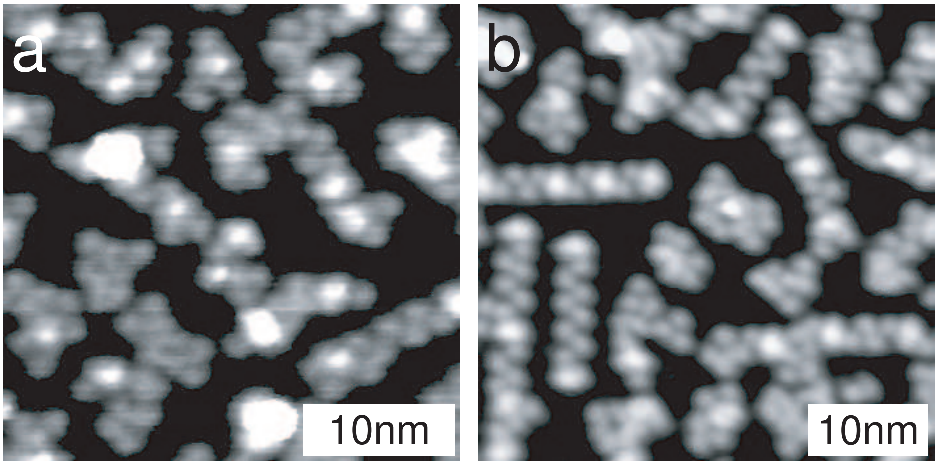

Figure 8.13: **a** STM-image of cat30 on Ag(111) after annealing to 300K. One can identify circular protrusions aggregated into clusters, some of them showing a typical *zigzag* structure. No fragments of cat30 could be clearly identified. (U=1500mV, I=300pA, T=5K) **b** STM image of cat30 on Ag(111) after annealing to 450K. Well-ordered *zigzag* structures based on uniform building blocks can be identified, with no distinct appearance of cat30 fragments. In STM-topographs of this preparation islands with an odd number of protrusions, single protrusions on step edges and islands with single protrusions neighboring a pair of protrusions can be identified, indicating that these protrusions correlate to the cat30 molecules. (U=750mV, I=200pA, T=5K)

Cu(100)-surfaces were cleaned by repeated cycles of sputtering with 500eV Ar^+ ions and subsequent annealing to 820K and 800K, respectively. The cat30 molecules were evaporated from an OMBE, with the crucible containing the cat30-molecules kept at a temperature of 600K, onto the Ag(111)- and the Cu(100)-surface kept at a temperature of 300K. The coverage of cat30 molecules was always in the submonolayer regime. The so obtained samples were either kept at 300K or annealed to 450K. Cu was deposited by means of a commercial Omicron e^--beam evaporator. All STM measurements were performed at a sample temperature of about 5K.

In Figure 8.13a one can see a typical STM-topograph of cat30 molecules deposited onto Ag(111) at 300K. In these STM images, one can identify protrusions aggregated into clusters. Because of the irregular appearance of some protrusions and the poor resolution inside the disordered clusters a reliable correlation of these features within these structures to the cat30 molecules was not possible. The protrusions in the clusters have a mean height of 1.04Å±0.1Å, independent of the tunneling parameters, and show no pronounced inner structure. The aggregation of the cat30-molecules into clusters is not surprising because of functional groups in the phenanthroline groups and the pentaethyleneoxy chains within the molecules, which should enable intermolecular bonding.

Although most of the clusters seem to have an arbitrary shape some cluster appear quite ordered, with the uniform protrusions arranged in a *zigzag*-structure. The formation of this *zigzag* structure was enhanced by annealing the sample to 450K. In Figure 8.13b one can see an STM-picture taken at 5K of cat30 molecules deposited onto Ag(111) a 300K and subsequently annealed to 450K. The same results can be obtained by depositing the cat30 molecules directly on a Ag(111) surface kept at 450K. A likely explanation for the evolution of the number of cluster showing the ordered *zigzag*-structure during annealing is that the movement of the cat30 molecules is thermally hindered at low temperature, making it impossible to reach the adequate binding positions to form the *zigzag*-structure whereas upon annealing the cat30 molecules can move into the binding positions. It can not be excluded that the movement of the molecules at 300K is hindered by solvent and fragments of cat30, generated at sublimation, which are desorbed upon annealing and thus enabling the formation of the *zigzag*-structure. The individual protrusions in the *zigzag* structure have a very uniform, circular shape and show no inner structure. The diameter, defined as the full width at half maximum (FWHM), is 1.62nm±0.18nm and the height is 1.07Å±0.06Å, as in the disordered clusters before annealing. The STM-topographs were acquired without moving the molecules at tunneling parameters of U=750mV and I=200pA.

The very uniform size and shape of the single protrusions of the *zigzag*-rows after annealing to 450K strongly indicate intact cat30 molecules on the Ag(111)-surface as it is almost impossible that thermally generated fragments of the cat30-molecules are all of the same shape. We expect that fragments of the cat30 molecules, such as an individual ring or a fragment of a ring, would be identifiable in STM-topographs. Single rings of the cat30 molecules would be almost planar and we should be able to see an inner structure as shown with our experiments on the macrocyclic molecule mt33 in Chapter 7, which is very similar to the single rings of cat30. Fragments of the rings would be much smaller than the observed protrusions and would be therefore easy to distinguish. Therefore we exclude a total thermal fragmentation of the cat30 molecules during sublimation, but rather conclude that most of the cat30 catenanes stay intact upon sublimation. Nevertheless, it can not be excluded that before annealing to 450K fragments of cat30 molecules were on the surface which were desorbed during the annealing.

The *zigzag* structure consists of pairs of protrusions arranged in linear

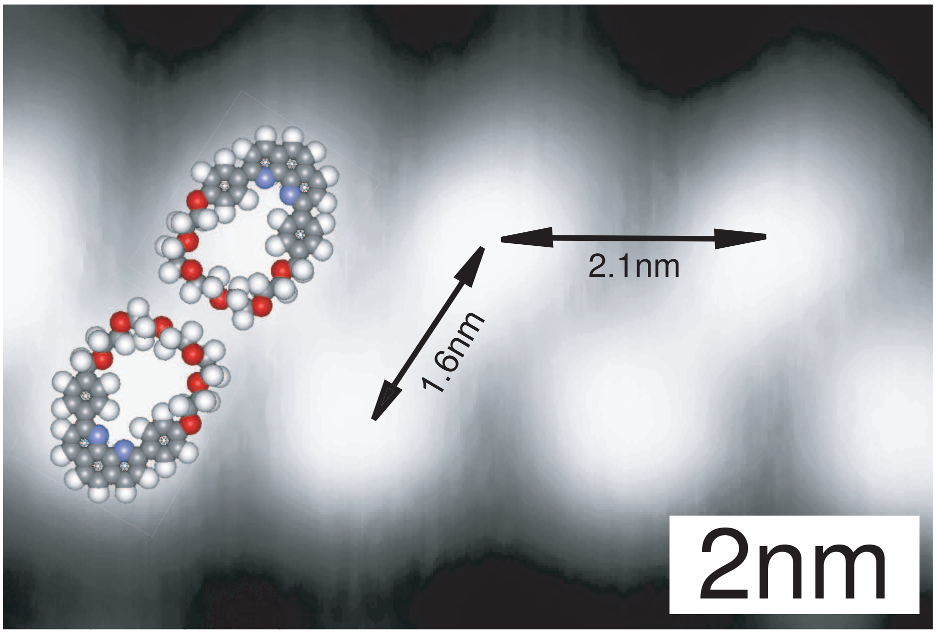

Figure 8.14: High-resolution STM-image of the cat30 *zigzag*-structure on Ag(111) after annealing to 450K. Superimposed structural models of the rings of the cat30 molecules show that a pair of protrusion cannot be correlated to one cat30 molecule as the distance between two protrusions is too large, strengthening the assumption that one protrusion corresponds to one cat30 molecule. (U=750mV, I=200pA, T=5K)

chains, with a peak-to-peak distance within each pair of 1.6nm±0.08nm and a distance of 2.1nm±0.1nm between the pairs along the chain direction. Two possibilities seem likely for correlation of the STM topograph to the actual cat30 molecule structure. The first one would assign each protrusion as one cat30 molecule. The second correlates two protrusions with one cat30 molecule. Several assumptions show that the first possibility, correlating one protrusion with one cat30 molecule, is a plausible one. In Figure 8.14 a high-resolution STM-topograph of the *zigzag*-structure with superimposed structural models of the rings of the cat30 molecules is shown. The assumption that a pair of protrusions is a cat30 molecule can be easily abolished as if one compares the size of the rings with the distance of the protrusions one will find that it is impossible that they are interlocked over this distance. Furthermore, in some STM-images one can see islands formed out of an odd number of protrusions, single protrusion on step edges or a single protrusion attached to the *zigzag* structure, which supports the idea that single protrusions are individual cat30 molecules.

Since we cannot resolve the adsorption orientation and morphology of the cat30 molecules we can not give a reliable model of the *zigzag* structure. Upon adsorption on the Ag(111) surface we have to expect alterations of the cat30 structure and the intermolecular binding motif compared to the crystal, as in the bulk structure benzene (used as solvent) is incorporated and the influence of the surface cannot be neglected. It is likely that the bonding motif of the cat30 molecules on Ag(111) is similar to the bulk structure. In the bulk structure of cat30, as obtained from X-ray diffraction experiments and described in [218], the cat30 crystal consist of linear chains of pairs of cat30 molecules, like the adsorbed cat30 structure we observed on Ag(111).

To test if cat30 molecules adsorbed onto a metal surface can act as molecular machines by performing a conformational change, we reacted cat30 catenanes and Cu-atoms which result in the formation of cat30 metallo-catenates, accompanied by a change of the molecular shape. This reaction was determined by the fact that in cat30 metallo-catenates the N-atoms of the phenanthrolines groups are involved in a coordination binding with the trapped Cu-atom and cannot be used for intermolecular binding. Considering this and the modified shape of the metallo-catenate with respect to the catenane observed by X-ray diffraction measurements in [218], the cat30 metallo-catenate structures formed onto a surface should significantly differ from the ones formed out of pristine cat30 molecules.

As a first test of the reactivity of cat30 with Cu atoms we deposited cat30 molecules onto a Cu(100) surface. As shown in Chapter 8.1, on this surface a highly reactive two-dimensional Cu-adatom gas exists, which should act as a huge reservoir for Cu-atoms and give the cat30 molecules ample opportunities

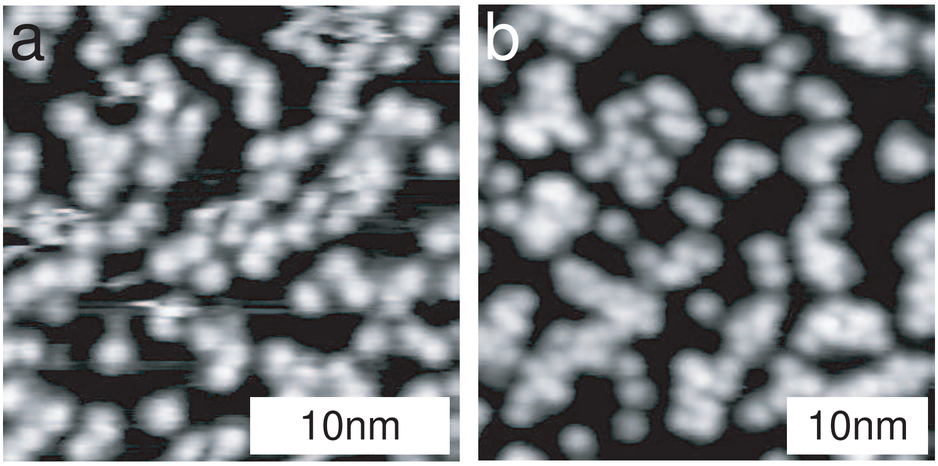

Figure 8.15: **a** STM-topograph of cat30 molecules deposited onto Cu(100) and a subsequent annealing to 300K. The protrusions appear circular with a height of 1.27Å±0.14Å. They are mostly aggregated into islands, although individual protrusions can be seen as well. Furthermore, again no fragments of cat30 could be clearly identified. (U=2000mV, I=300pA, T=5K). **b** STM image of cat30 on Cu(100) after annealing to 450K. The protrusions have a diameter of 1.66nm±0.2nm and a height of 1.38Å±0.18Å. No difference neither in the formed structures nor in the tunneling parameters occurred with respect to the preparation with an annealing temperature of 300K, especially the formation of *zigzag* structures could not be observed, indicating a modified bonding motif because of structural alterations of the cat30 molecules due to incorporated Cu-adatoms. (U=2000mV, I=300pA, T=5K)

to react with the Cu-atoms.

Figure 8.15a shows a typical STM-topograph obtained after the deposition of cat30 on Cu(100) at 300K in which one can identify protrusions, with a height of 1.27Å±0.14Å, aggregated into disordered structures. While *zigzag* rows appear on Ag(111) already at 300K, they cannot be observed on the Cu(100) surface but instead we can identify single protrusion not aggregated into clusters. In analogy to the preparation of the cat30 *zigzag* structure on Ag(111) we annealed the sample to 450K. In Figure 8.15b one can see an STM-picture taken at 5K of cat30 molecules deposited onto a Cu(100) substrate at 300K and subsequently annealed to 450K. The result of this preparation differs significantly from the one obtained on Ag(111). Whereas on Ag(111) most of the cat30 molecules aggregate in *zigzag* rows after annealing to 450K, on Cu(100) we see instead disordered islands consisting of protrusion with a uniform, almost circular shape with a FWHM of

1.66nm±0.2nm, no resolvable inner structure and a height of 1.38Å±0.18Å. We also observe single protrusions, which have the same shape and size as the ones aggregated into clusters. As the cat30 molecules on Cu(100) appear uniform after annealing to 450K, we conclude that they stay intact at this temperature. The observation of single protrusions supports the assumption that the individual protrusions can be correlated with single cat30 molecules. The STM-topographs had to be acquired with rather unusual tunneling parameters with the bias voltage U=2000mV and the tunneling current I=200pA. Lowering the bias voltage U or increasing the tunneling current I again resulted in a shifting of the cat30 molecules, indicating rather weak intermolecular interactions in the clusters or a weak diffusion barrier of the cat30-molecules on the Ag(111)-substrate. A reliable model of the binding geometry of the cat30 molecules with respect to the Cu(100) surface cannot be given.

The observed behavior of the cat30 molecules on the Cu(100) surface indicates a reaction of the cat30 molecules with the Cu atoms. The absence of the cat30 *zigzag* structure on the Cu(100) surface together with the observation of individual cat30 molecules and a decreased intermolecular stability is consistent with a missing intermolecular bonding motif. This is in agreement with our prediction that the cat30 molecules will react with the Cu-atoms and form metallo-catenates, in which all N-atoms are involved in a coordination binding with the Cu-atoms and can therefore not participate in intermolecular bindings, resulting in single cat30 molecules on the Cu(100) surface. The observed height-difference between the cat30 molecules on Ag(111) and Cu(100) can be attributed to the different configurations of the pristine cat30 catenanes on Ag(111) and the cat30 metallo-catenate on Cu(100). We can conclude that the formation of the cat30 metallo-catenate due to inclusion of the Cu atoms in the cat30 molecules must already occur at 300K as absolutely no *zigzag*-structures can be observed on Cu(100) at 300K, in contrast to the Ag(111) substrate where *zigzag*-rows already occur at 300K. This statement is supported by the fact that the tunneling parameters did not change due to annealing, implying that the intermolecular and translational barrier on the Cu(100) substrate of the cat30 molecules did not change during annealing.

To ensure that the observed differences between the cat30 structures formed on Ag(111) and Cu(100) are due to a transition of the cat30 catenanes to cat30 metallo-catenates because of a trapping of Cu-atoms and not due to a different binding behavior of the cat30 molecules with the Ag(111)- and Cu(100)-surface, further experiments were performed in which we prepared cat30 metallo-catenates, incorporating Cu atoms, onto a Ag(111) surface. This enabled us to directly compare the structure formation of the cat30 catenane and the cat30 metallo-catenate without the influence of different substrates. To prepare such a sample, we first deposited cat30 molecules onto a Ag(111) substrate and annealed to 450K to fabricate the *zigzag* structure and in a second step, Cu was deposited onto the sample. As we will show, this preparation results in the very same structures as cat30 on Cu(100), indicating the formation of cat30 metallo-catenates within this preparation.

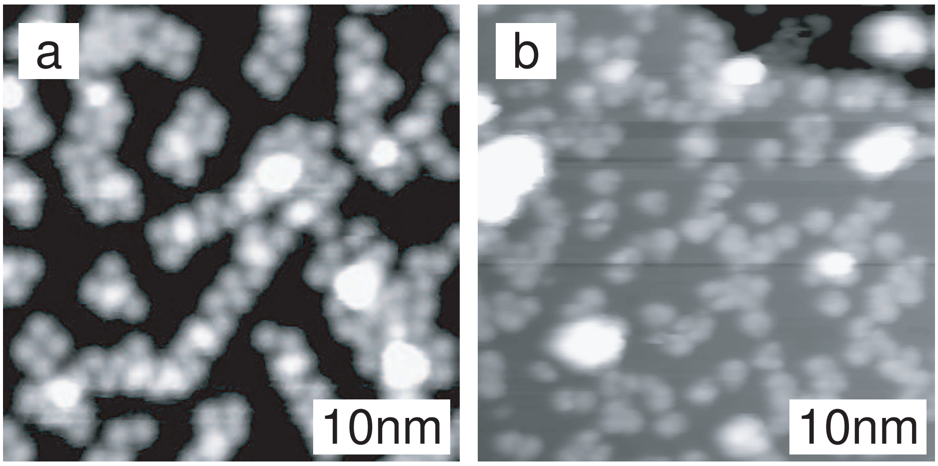

Figure 8.16: STM-image of cat30 on Ag(111) with codeposited Cu after annealing to 300K. **a** The initial preparation of cat30 on Ag(111) followed by an annealing to 450K shows the well-ordered *zigzag* structure. (U=750mV, I=200pA, T=5K)**b** The very same preparation after the codeposition of Cu onto the sample kept at 300K. A tremendous change occurred: the initial *zigzag* structure was replaced by disordered islands which resemble the cat30 structures formed on Cu(100). This supports the assumption that the structural difference between cat30 on Ag(111) and Cu(100) is due to a modified intermolecular binding motif because of a reaction between the cat30 molecules and Cu-atoms and not to an altered substrate-molecule interaction. (U=2000mV, I=200pA, T=5K)

Figure 8.16a shows the *zigzag* structure obtained after the depositing of cat30 molecules onto a Ag(111) surface and subsequent annealing to 450K. The sample was allowed to cool to 300K and Cu was deposited, without any further annealing needed to initiate a reaction. This is consistent with our experiments on the deprotonation of TMA in Chapter 8.1, where we showed that by depositing Cu atoms on Ag(111) it is possible to fabricate an artificial Cu adatom gas with a chemical activity comparable to the native adatom gas of the Cu(100) surface. We therefore expected a reaction between the cat30 molecules and the codeposited Cu atoms in this preparation. The so obtained structure is shown in Figure 8.16b. It is obvious that a tremendous change of the cat30 structure took place upon Cu deposition. The *zigzag* structure formed on Ag(111) was replaced completely by irregular cat30 structures and individual cat30 molecules, which resembles to the structure formation of the cat30 metallo-catenate molecules on Cu(100), with the FWHM of the cat30 molecules being 1.78Å±0.2Å. The height of the cat30 molecules changed from the initial value of 1.1nm±0.1nm on pristine Ag(111) to 1.41Å±0.24Å after the codeposition of Cu, which is in good agreement with the height of the cat30 molecules on Cu(100). The parameters for stable tunneling also changed in a rigorous way: while the *zigzag* structures formed out of pristine cat30 could be easily imaged without modifying the *zigzag* structures (U=750mV, I=200pA), after the deposition of Cu onto the *zigzag* structure one needed tunneling parameters like on the Cu(100) surface (U=2000mV, I=200pA) to image the surface without displacing the cat30 molecules. The behavior of the cat30 molecules on Ag(111) after Cu deposition was identical to the cat30 molecules on Cu(100). We conclude that in this preparation a reaction of the cat30 catenanes and Cu atoms takes place, resulting in the formation of cat30 metallo-catenates.

Apart from the cat30 molecules one can also see Cu islands in Figure 8.16, what indicates that much more Cu atoms were deposited than can react with the cat30 molecules. In a second step we prepared a *zigzag* structure and then deposited small amounts of Cu in a step-wise manner at 300K, with STM measurements between each deposition step. If the Cu atoms are reacting with the cat30 molecules one should expect to see a stepwise decrease of cat30 molecules in *zigzag* structures accompanied by a stepwise increase of irregular cat30 islands. In Figures 8.17a-d such a sequence of preparations is shown. Figure 8.17a shows the initial *zigzag* rows of pristine cat30 molecules on Ag(111). Figure 8.17b shows the very same preparation but after the deposition of ∼1% of a monolayer of Cu-atoms. The number of cat30 *zigzag* structure decreased and the number of disordered islands increased. The tunneling parameters used to acquire the STM images were U=700mV and I=200pA, like in the system cat30 on Ag(111). Figure 8.17c shows the very same preparation after an additional deposition of Cu, resulting in a total amount of Cu on the surface of ∼2% of a monolayer. In STM-topographs made on this preparation already no *zigzag* rows can be identified. To acquire STM-images without shifting the cat30 molecules the tunneling parameter had to be set to U=2000mV and I=300pA, like in the cat30 on Cu(100) system. Figure 8.17d shows the structure after an additional Cu deposition, with a total amount of Cu on the Ag(111) surface of ∼5%. Here we see Cu-islands and irregular cat30 islands, similar to the cat30 islands on Cu(100). Also the tunneling parameters of U=1500mV and I=200pA are similar to

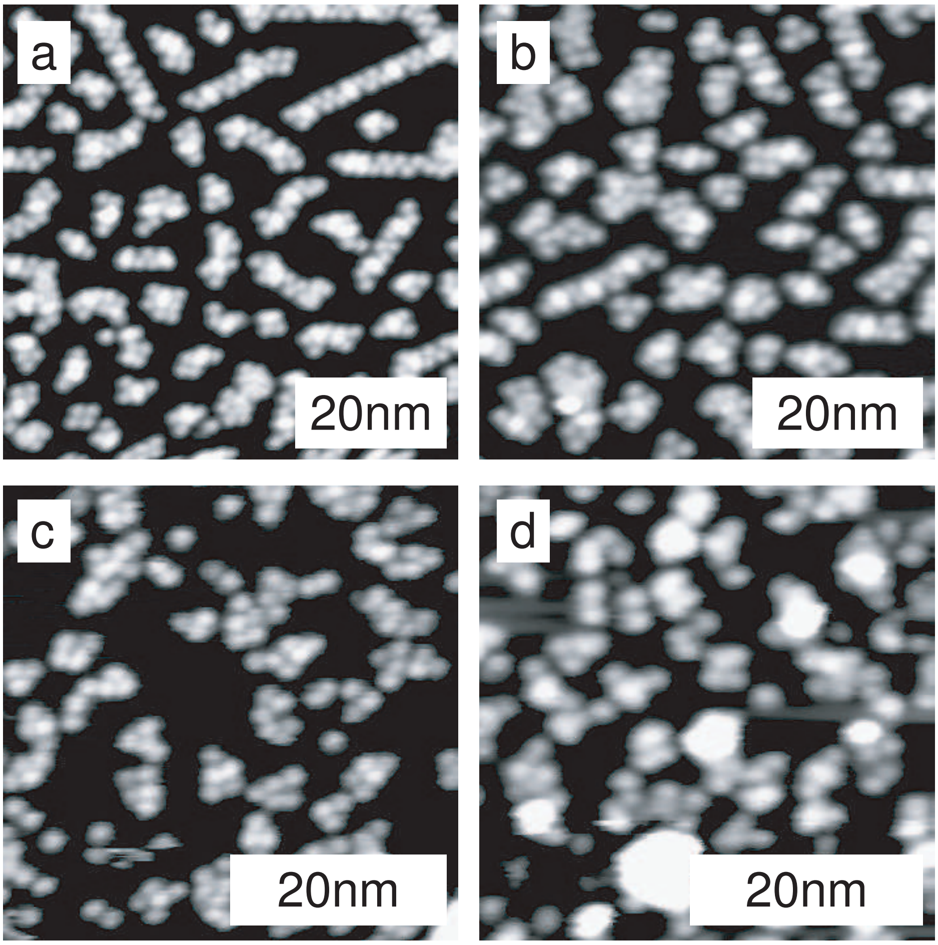

Figure 8.17: STM-images of cat30 on Ag(111) with an increasing amount of codeposited Cu. These experiments clearly shows that the structural modification is correlated to the deposited Cu-atoms. **a** The initial cat30 *zigzag* structure on pristine Ag(111) (U=700mV, I=200pA, T=5K)**b** The very same preparation after the deposition of ~1% of a monolayer of Cu at 300K. One can already identify a decrease of the amount of island showing *zigzag*-structure. (U=700mV, I=200pA, T=5K) **c** After the deposition of an additional ~1% of a monolayer of Cu, almost no *zigzag* structures can be found. (U=2000mV, I=300pA, T=5K) **d** In the last step a total amount of ~5% of a monolayer of Cu was on the sample. Absolutely no *zigzag* structure could be observed but instead the formation of Cu-islands can be seen, indicating a saturation of all cat30 molecules with Cu-atoms. (U=1500mV, I=200pA, T=5K)

these used the Cu(100) surface. These observations indicate the reaction of the cat30 molecules with Cu atoms. The difference in behavior of the cat30 molecules on the pristine Ag(111)-surface compared to the pristine Cu(100)-surface and the Ag(111) surface with codeposited Cu indicated the reaction of cat30 catenanes with Cu atoms to cat30 metallo-catenates. As there is no difference in the behavior of the cat30 metallo-catenates on Cu(100) and on Ag(111) we conclude that the surface has little influence on this reaction.

In our measurements of cat30 on Ag(111) and Cu(100) we obtained strong indications that we deposit intact cat30 molecules by thermal sublimation. In STM-topographs of cat30 on Ag(111) and Cu(100) we observe only circular and uniform protrusions, but no fragments of the catenanes. As we can identify individual protrusions and island containing an odd number of protrusion, we conclude that these protrusions correlate with individual cat30 molecules.

The cat30 molecules can react with the Cu-atoms when adsorbed on a surface, which is correlated to a change of the observed size. The reaction of the cat30 molecules with Cu atoms could be shown by observing a modified intermolecular binding behavior, which is consistent with the saturation of the N-atoms as intermolecular binding sites due to the complex formation with the Cu^{I}-ions and the accompanying structural alteration of the cat30 molecules associated with the incorporation of a Cu-adatom, upon adsorption onto Cu(100). This observation is supported by experiments with cat30 molecules on Ag(111) and a variable amount of codeposited Cu. With increasing amount of Cu the well-ordered *zigzag* structures on clean Ag(111) are replaced by the disordered structures found on Cu(100), showing that the different cat30 structures formed on Ag and Cu are not due to a altered molecule-substrate interaction on Cu(100) with respect to Ag(111) but due to a modified molecule-molecule interaction, induced by a reaction with the Cu-adatoms.

Bibliography

[1] Information found on http:\\www.intel.com

[2] D. Normile, *Science* 293(**2003**)787

[3] N. Maathur, *Nature* 419(**2002**)573

[4] J. Li, W. D. Schneider, R. Berndt, B. Delley, *Phys. Rev. Lett* 80(**1998**)2893

[5] V. Madhavan, W. Chen, T. Jamneala, M. F. Crommie, N. S. Wingreen, *Science* 280(**1998**)567

[6] B. C. Stipe, M. A. Rezaei, W. Ho, *Science* 280(**1998**)1732

[7] B. C. Stipe, M. A. Rezaei, W. Ho, *Phys. Rev. Lett.* 82(**1999**)1724

[8] D. M. Eigler, E. K. Schweizer, *Nature* 344(**1990**)524

[9] K. F. Braun, K. H. Rieder, *Phys. Rev. Lett.* 88(**2002**)096801

[10] J. V. Barth, G. Constantini, K. Kern, *Nature* 437(**2005**)671

[11] R. Raval, *J. Phys.: Condens. Matter* 14(**2002**)4119

[12] G. A. Jeffrey, W. Saenger, *Hydrogen bonding in biological systems* (Springer, Berlin, 1991)

[13] J. V. Barth, J. Weckesser, C. Cai, P. Günter, L. Bürgi, O. Jeandupeux, K. Kern, *Ang. Chem. Int. Ed.* 39(**2000)**1230

[14] J. A. Theobald, N. S. Oxtoby, M. A. Philips, N. R. Champness, P. H. Beton, *Nature* 424(**2003**)1029

[15] M. Furukawa, H. Tanaka, K. I. Sugiura, Y. Sakata, T. Kawai, *Surf. Sci.* 445(**2000**)L58

[16] J. Weckesser, A. DeVita, J. V. Barth, C. Cai, K. Kern, *Phys. Rev. Lett.* 87(**2001**)096101

[17] A. McNutt, S. Haq, R. Raval, *Surf. Sci.* 531(**2003**)131

[18] S. De Feyter, F. C. De Schryver, *Chem. Soc. Rev.* 32(**2003**)139

[19] M. Meot-Ner (Mautner), *Chem. Rev.* 105(**2005**)213

[20] F. Silly, M. Pivetta, M. Ternes, F. Patthey, J. P. Pelz, W. D. Schneider, *Phys. Rev. Lett.* 92(**2004**)0161011

[21] M. Ternes, C. Weber, M. Pivetta, F. Patthey, J. P. Pelz, T. Giamarchi, F. Mila, W. D. Schneider, *Phys. Rev. Lett.* 93(**2004**)146805

[22] L. Gross, F. Moresco, L. Savio, A. Gourdon, C. Joachim, K. H. Rieder, *Phys. Rev. Lett.* 93(**2004**)056103

[23] S. Crampin, H. Jensen, J. Kröger, L. Limot, R. Berndt, *cond. mat.*/0501102

[24] J. Kliewer, R. Berndt, S. Crampin, *New J. Phys.* 3(**2001**)22

[25] M. F. Crommie, C. P. Lutz, D. M. Eigler, *Science* 262(**1993**)218

[26] L. Diekhöner, M.A. Schneider, A.N. Baranov, V.S. Stepanyuk, P. Bruno, K. Kern *Phys. Rev. Lett.* 90(**2003**)236801

[27] J. Li, W. D. Schneider, R. Berndt, S. Crampin, *Phys. Rev. Lett.* 80(**1998**)3332

[28] F. Biscarini, W. Gebauer, D. Di Domenico, R. Zamboni, J. I. Pascual, D. A. Leigh, A. Murphy, D. Tetard, *Synthetic Metals* 102(**1999**)1466

[29] X. Zheng, M. E. Mulcahy, D. Horinek, F. Galeotti,T. F. Magnera, J. Michl, *J. Am. Chem. Soc.* 126(**2004**)4540

[30] D. Borissov, A. Ziegler, S. Höger, W. Freyland, *Langmuir* 20(**2004**)2781

[31] V. Kalsani, H. Ammon, F. Jäckel, J. P. Rabe, M. Schmittel, *Chem. Eur. J.* 10(**2004**)5481

[32] I. Kossev, S. Fahrenholz, A. Görling, W. Hieringer, C. A. Schalley, M. Sokolowski, *Synthetic Metals* 147(**2004**)159

[33] P. Samori, F. Jaeckel, Ö. Ünsal, A. Godt, J. P. Rabe, *ChemPhysChem* 7(**2001**)461

[34] J. Kolaszkiewicz, E. Bauer, *Surf. Sci.* 155(**1985**)700-714

[35] M. Nohlen, M. Schmidt, H. Wolter, K. Wandelt, *Surf. Sci.* 337(**1995**)294-301

[36] R.M. Tromp, M. Mankos, *Phys. Rev. Lett.* 81(**1998**)1050-1053

[37] W. Silvestri, A.P. Graham, J.P. Toennies, *Phys. Rev. Lett.* 81(**1998**)1034-1037

[38] J. Kolaszkiewicz, *Surf. Sci.* 183(**1987**)251-262

[39] S. Abbet, A. Sanchez, U. Heiz, W.D. Schneider, A.M. Ferrari, G. Pacchioni, N. Rösch, *J. Am. Chem. Soc.* 122(**2000**)3453-3457

[40] S. Abbet, U. Heiz, H. Häkkinen, U. Landmann, *Phys. Rev. Lett.* 86(**2001**)5950-5953

[41] C. Nozaki, C.G. Lugmair, A.T. Bell, T.D. Tilley, *J. Am. Chem. Soc.* 124(**2002**)13194-13203

[42] J. Michl, T. F. Magnera, *Proc. Natl. Acad. Sci. USA* 99(**2002**)4788

[43] A. Semenov, J. P. Spatz, M. Möller, J. M. Lehn, B. Sell, D. Schubert, C. H. Weidl, U. S. Schubert, *Ang. Chem. Int. Ed.* 38(**1999**)2547

[44] D. G. Kurth, N. Severin, J. P. Rabe, *Ang. Chem. Int. Ed.* 41(**2002**)3681

[45] U. Ziener, J. M. Lehn, A. Mourran, M. Möller, *Chem. Eur. J.* 8(**2002**)951

[46] A. Dmitriev, H. Spillmann, N. Lin, J. V. Barth, K. Kern, *Ang. Chem. Int. Ed.* 42(**2003**)2670

[47] M. A. Lingenfelder, H. Spillmann, A. Dmitriev, S. Stepanow, N. Lin, J. V. Barth, K. Kern, *Chem. Eur. J.* 10(**2004**)1913

[48] S. Stepanow, M. Lingenfelder, A. Dmitriev, H. Spillmann, E. Delvigne, N. Lin, X. Deng, C. Cai, J. V. Barth, K. Kern, *Nat. Mater.* 3(**2004**)229

[49] N. Lin, S. Stepanow, F. Vidal, J. V. Barth, K. Kern, *Chem. Comm.* (**2005**)1681

[50] G. Binning, H. Rohrer, C. Gerber, E. Weibel, *Phys. Rev. Lett.* 49(**1982**)57

[51] J. Frohn, J. F. Wolf, K. Besocke, M. Teske, *Rev. Sci. Instrum.* 60(**1989**)1200

[52] B. C. Stipe, M. A. Rezai, W. Ho, *Rev. Sci. Instrum.* 70(**1999**)137

[53] K. J. Wahl, L. E. Seitzman, R. N. Bolster, I. L. Singer, M. B. Peterson, *Surface and Coatings Technology* 89(**1997**)245

[54] I. Giaever, *Phys. Rev. Lett.* 5(**1960**)147

[55] J. Tersoff, D. R. Hamann, *Phys. Rev. Lett.* 50(**1983**)1998

[56] J. Bardeen, *Phys. Rev. Lett.* 6(**1961**)57

[57] N. D. Lang, *Phys. Rev. B* 34(**1986**)5947

[58] A. Einstein, *Annalen der Physik* 17(**1905**)132

[59] M. P. Seah, W. A. Dench, *Surf. Interface Anal.* 1(**1979**)2

[60] D. A. Shirley *Phys. Rev. B* 5(**1972**)4709

[61] J. W. Niemantsverdriet, *Spectroscopy in Catalysis - An Introduction* (VCH, Weinheim, 1995)

[62] J. Chastian, R. C. King *Handbook of x-ray photoelectron spectroscopy: A reference book of standard spectra for identification and interpretation of XPS spectra* (Physical Electronics Inc., Eden Prairie, Minesota, 1995)

[63] J. Stöhr, *NEXAFS spectroscopy* (Springer, Berlin, 1992)

[64] J. M. Lehn, *Science* 295(**2002**)2400

[65] J. M. Lehn, *Proc. Natl. Acad. Sci. USA* 99(**2002**)4763

[66] M. Ruben, *Angew. Chem. Int. Ed.* 44(**2005**)1594

[67] K. Uosaki, R. Yamada, *J. Am. Chem. Soc.* 121(**1999**)4090

[68] J. V. Barth, J. Weckesser, N. Lin, A. Dmitriev, K. Kern, *Appl. Phys. A* 76(**2003**)645

[69] B. Immaraporn, P. Ye, A. J. Gellman, *J. Phys. Chem. B* 108(**2004**)3504

[70] L. S. Caputi, G. Chiarello, M. G. Lancellotti, G. A. Rizzi, M. Sambi, G. Granozzi, *Surf. Sci. Lett.* 291(**1993**)L756

[71] M. Bowker, E. Rowbotham, F. M. Leibsle, S.Haq, *Surf. Sci.* 349(**1996**)97

[72] J. G. Lee, J. Ahner, D. Mocuta, S. Denev, J. T. Yates, *J. Chem. Phys.* 112(**2000**)3351

[73] B. Parker, B. Immaraporn, A. J. Gellmann, *Langmuir* 17(**2001**)6638

[74] D.S Martin, R.J. Cole, S. Haq, *Surf. Sci* 539(**2003**)171

[75] S. Stepanow, T. Strunskus, M. Lingenfelder, A. Dmitriev, H. Spillmann, N. Lin, J. V. Barth, Ch. Wöll,K. Kern, *J. Phys. Chem. B* 108(**2004**)19392

[76] A. Dmitriev, N. Lin, J. Weckesser, J.V. Barth, K.Kern, *J. Phys. Chem. B* 106(**2002**)6907

[77] D. Braga, A. Angelino, E. Tagliavini, F. Grepioni, *J. Chem. Soc., Dalton Trans.* (**1998**)1961

[78] S. Griessl, M. Lackinger, M. Edelwirth, M. Hietschold, W.M. Heckl, *Single Mol.* 3(**2002**)25

[79] K. G. Nath, O. Ivasenko, J. A. Miwa, H. Dung, J. D. Wuest, A. Nanci, D. F. Perepichka, F. Rosei, *J. Am. Chem. Soc.* 128(**2006**)4212

[80] N. Lin, D. Payer, A. Dmitriev, T. Strunskus, C. Wöll, J. V. Barth, K. Kern, *Angew. Chem. Int. Ed.* 44(**2005**)1488

[81] Y. Ishikawa, A. Ohira, M. Sakata, C. Hirayama, M. Kunitake, *Chem. Comm.* (**2002**)2652

[82] G. J. Su, H. M. Zhang, L. J. Wan, C. L. Bai, T. Wandlowski, *J. Phys. Chem. B* 108(**2004**)1931

[83] J. Li, W.D. Schneider, R. Berndt, O.R. Bryant, S. Crampin, *Phys. Rev. Lett.* 81(**1998**)4464

[84] L. Bürgi, L. Petersen, H. Brune, K. Kern, *Surf. Sci.* 447(**2000**)L157

[85] L. Bürgi, N. Knorr, H. Brune, M.A. Schneider, K. Kern, *Appl. Phys. A* 75(**2002**)141

[86] L.H. Dubois, B.R. Zegarski, R.G. Nuzzo, *Langmuir* 2(**1986**)412

[87] S.W. Han, S.W. Joo, T.H. Ha, Y. Kim, K. Kim, *J. Phys. Chem. B* 104(**2000**)11987

[88] M. Wühn, J. Weckesser, C. Wöll, *Langmuir* 17(**2001**)7605

[89] G. Axelson, U. Ericson, A. Fahlman, K. Hamrin, J. Hedman, R. Nordberg, R. Nordling, K. Siegbahn, *Nature* 213(**1967**)70

[90] D.L. Hoof, D.G. Tisley, R.A. Walton, *J. Chem. Soc. Dalton Trans.* (**1973**)200

[91] U. Gelius, P.F. Heden, J. Hedman, B.J. Lindberg, R. Manne, R. Nordberg, C. Nordling, K. Siegbahn, *Physica Scripta* 2(**1970**)70

[92] R. Car, M. Parrinello, *Phys. Rev. Lett.* 55(**1985**)2471

[93] D. Payer, A. Comisso, A. Dmitriev, T. Strunskus, N. Lin, C. Wöll, A. DeVita, J.V. Barth, K. Kern, *Ionic hydrogen bonds in 2-dimensional supramolecular systems at metallic surfaces; Chemistry - a European Journal, in press*

[94] R. Paniago, R. Matzdorf, G. Meister, A. Goldmann, *Surf. Sci.* 325(**1995**)336

[95] H. Hövel, B. Grimm, B. Reihl, *Surf. Sci.* 477(**2001**)43

[96] T. Andreev, I. Barke, H. Hövel, *Phys. Rev. B* 70(**2004**)205426

[97] S. Lehwald, H. Ibach, J.E. Demuth, *Surf. Sci.* 78(**1978**)577

[98] P. Yannoulis, R. Dudde, K.H. Frank, E.E. Koch, *Surf. Sci.* 189(**1987**)519

[99] C. Mainka, P. S. Bagus, A. Schertel, T. Strunskus, M. Grunze, C. Wöll, *Surf. Sci.* 341(**1995**)L1055

[100] K. Weiss, S. Gebert, M. Wühn, H. Wadepohl, C. Wöll, *J. Vac. Sci. Technol. A* 16(**1998**)1017

[101] S. Lukas, S. Söhnchen, G. Witte, C. Wöll, *Chem. Phys. Chem.* 5(**2004**)266

[102] W. Jacob, V. Dose, A. Goldmann, *Appl. Phys. A* 41(**1986**)145

[103] S. A. Lindgren, J. Paul, L. Wallden, *Surf. Sci.* 117(**1982**)426

[104] C. T. Chen, N. V. Smith, *Phys. Rev. B* 40(**1989**)7487

[105] A. Lindgren, L. Wallden, *Solid. State Commun.* 34(**1980**)671

[106] A. Lindgren, L. Wallden, *Phys. Rev. Lett.* 59(**1987**)3003

[107] B.G. Frederick, Q. Chen, F.M. Leibsle, M.B. Lee, K.J: Kitching, N.V. Richardson, *Surf. Sci.* 394(**1997**)1

[108] M. Vladimirova, G. Trimarchi, A. Baldereschi, J. Weckesser, K. Kern, J. V. Barth, A. De Vita, *Acta Mat.* 52(**2004**)1589

[109] M. Böhringer, K. Morgenstern, W.D. Schneider, R. Berndt, F. Mauri, A. De Vita, R. Car, *Phys. Rev. Lett.* 83(**1999**)324

[110] J.V. Barth, J. Weckesser, G. Trimarchi, M. Vladimirova, A. De Vita, C. Cai, H. Brune, P. Günter, K. Kern, *J. Am. Chem. Soc.* 124(**2002**)7991

[111] M. Vladimirova, M. Stengel, A. De Vita, A. Baldereschi, M. Böhringer, K. Morgenstern, R. Berndt, W.D. Schneider, *Europhys. Lett.* 56(**2001**)254

[112] P. F. Schwab, F. Fleischer, J. Michl, *J. Org. Chem.* 67(**2002**)443

[113] M. Ruben, D. Payer, A. Landar, A. Comisso, C. Gattinoni, N. Lin, J. P. Collin, J. P. Sauvage, A. De Vita, K. Kern, *J. Am. Chem. Soc.* 128(**2006**)15644

[114] C. Kittel, *Introduction to Solid State Physics - 7th edition* (John Wiley & Sons, New York, 1996)

[115] S. G. Davison, M. Steslicka, *Basic Theory of Surface States* (Oxford Press, New York, 1992)

[116] A. Zangwill, *Physics at Surfaces* (Cambridge University Press, New York, 1988)

[117] E. Bertel, P. Roos, J. Lehmann, *Phys. Rev. B* 52(**1995**)R14384

[118] N. Memmel, *Surf. Sci. Rep.* 32(**1998**)91

[119] N. Memmel, E. Bertel, *Phys. Rev. Lett.* 75(**1995**)485

[120] R. Matzdorf, G. Meister, A. Goldmann, *Phys. Rev. B* 54(**1996**)14807

[121] R. Matzdorf, *Surf. Sci. Rep.* 30(**1998**)153

[122] R. Paniago, R. Matzdorf, G. Meister, A. Goldmann, *Surf. Sci.* 336(**1995**)113

[123] B. A. McDougall, T. Balasubramanian, E. Jensen, *Phys. Rev. B* 51(**1995**)13891

[124] S. LaShell, B. A. McDougall, E. Jensen, *Phys. Rev. Lett.* 77(**1996**)3419

[125] S. L. Hulbert, P. D. Johnson, N. G. Stoffel, W. A. Royer, N. V. Smith, *Phys. Rev. B* 31(**1985**)6815

[126] S. L. Hulbert, P. D. Johnson, N. G. Stoffel, N. V. Smith, *Phys. Rev. B* 32(**1985**)3451

[127] D. P. Woodruff, W. A. Royer, N. V. Smith, *Phys. Rev. B* 34(**1986**)764

[128] A. Goldmann, V. Dose, G. Borstel, *Phys. Rev. B* 32(**1985**)1971

[129] M. F. Crommie, C. P. Lutz, D. M. Eigler, *Nature* 363(**1993**)524

[130] J. Li, W. D. Schneider, R. Berndt, *Phys. Rev. B* 56(**1997**)7656

[131] O. Jeandupeux, L. Bürgi, A. Hirstein, H. Brune, K. Kern, *Phys. Rev. B* 59(**1999**)15926

[132] L. Bürgi, O. Jeandupeux, H. Brune, K. Kern, *Phys. Rev. Lett.* 82(**1999**)4516

[133] L. Bürgi, H. Brune, O. Jeandupeux, K. Kern, *J. Electr. Spectr. Related Phenom.* 109(**2000**)33

[134] M. Pivetta, F. Silly, F. Patthey, J. P. Pelz, W. D. Schneider, *Phys. Rev. B* 67(**2003**)193402

[135] W. Chen, V. Madhaven, T. Jamneala, M. F. Crommie, *Phys. Rev. Lett.* 80(**1998**)1469

[136] N. Knorr, H. Brune, M. Epple, A. Hirstein, M.A. Schneider, K. Kern, *Phys. Rev. B* 65(**2002**)115420

[137] E. Wahlström, I. Ekvall, H. Olin, W. Walldn, *Appl. Phys. A* 66(**1998**)S1107

[138] L. Bürgi, O. Jeandupeux, A. Hirstein, H. Brune, K. Kern, *Phys. Rev. Lett.* 81(**1998**)5370

[139] O. Jeandupeux, L. Bürgi, A. Hirstein, K. Kern, *Phys. Rev. B* 59(**1999**)15926

[140] J. Li, W. D. Schneider, S. Crampin, R. Berndt, *Surf. Sci.* 422(**1999**)95

[141] H. C. Manoharan, C. P. Lutz, D. M. Eigler, *Nature* 403(**2000**)512

[142] S. Pons, P. Mallet, L. Magaud, J. Y. Veuillen, *Europhys. Lett.* 61(**2003**)375

[143] M. F. Crommie, C. P. Lutz, D. M. Eigler, E. J. Heller, *Physica D* 83(**1995**)98

[144] K. Shimoda, *Introduction to Laser Physics* (Springer, Berlin, 1986)

[145] I. Poleschak, J. K. Kern, J. P. Sauvage, *Chem. Commun.* (**2004**)474

[146] M. Deleuze, *J. Am. Chem. Soc.* 122(**2000**)1130

[147] C. P. Collier, G. Mattersteig, E. W. Wong, Y. Luo, K. Beverly, J. Sampaio, F. M. Raymo, J. F. Stoddart, J. M. Heath, *Science* 289(**2000**)1172

[148] Y. Luo, C. P. Collier, J. O. Jeppesen, K. A. Nielsen, E. Delonno, G. Ho, J. Perkins, H. R. Tseng, T. Yamamoto, J. F. Stoddart, J. R. Heath, *ChemPhysChem* 3(**2002**)519

[149] S. Stepanow, N. Lin, F. Vidal, A. Landa, M. Ruben, J. V. Barth, K. Kern, *Nanolett.* 5(**2005**)901

[150] F. Vidal, E. Delvigne, S. Stepanow, N. Lin, J. V. Barth, K. Kern, *J. Am. Chem. Soc.* 127(**2005**)10101

[151] M. Piacentra, S. Grimme, *ChemPhysChem* 6(**2005**)1554

[152] M. Stöhr, M. Wahl, C. H. Galka, T. Riehm, T. A. Jung, L. H. Gade, *Ang. Chem. Int. Ed.* 44(**2005**)7394

[153] T. Zambelli, J. Wintterlin, J. Trost, G. Ertl, *Science* 273(**1996**)1688-1690

[154] S. Dahl, A. Logadottir, R.C. Egeberg, J.H. Larsen, I. Chorkendorf, E. Tornquist, J.K. Norskov, *Phys. Rev. Lett.* 83(**1999**)1814-1817

[155] P. Gambardella, Z. Sljivancanin, B. Hammer, M. Blanc, K. Kuhnke, K. Kern, *Phys. Rev. Lett.* 87(**2001**)056103

[156] R. Schaub, R. Thostrup, N. Lopez, E. Laegsgaard, I. Stensgard, J.K. Norskov, F. Besenbacher, *Phys. Rev. Lett.* 87(**2001**)266104

[157] B. Hammer, *J. Catal.* 199(**2001**)171-176

[158] Z.P. Liu, P. Hu, *J. Am. Chem. Soc.* 125(**2003**)1958-1967

[159] T. Micheley, T. Land, U. Littmark, G. Comsa, *Surf. Sci.* 272(**1992**)204

[160] K. Kyuno, A. Gölzhauser, G. Ehrlich *Surf. Sci.* 397(**1998**)191

[161] C.C. Perry, S. Haq, B.G. Frederick, N.V. Richardson, *Surf. Sci.* 409(**1998**)512-520

[162] J.V. Barth, J. Weckesser, N. Lin, A.Dmitriev, K. Kern, *Appl. Phys. A* 76(**2003**)645-652

[163] N. Lin, A. Dmitriev, J. Weckesser, J.V. Barth, K. Kern, *Angew. Chem.* 114(**2002**)4973-4977

[164] N. Lin, A. Dmitriev, J. Weckesser, J.V. Barth, K. Kern, *Angew. Chem. Int. Ed.* 41(**2002**)4779-4783

[165] H.S. Taylor, *Proc. R. Soc. London A* (**1925**)108

[166] D.W. Goodman, *Chem. Rev.* 95(**1995**)523-536

[167] G.A. Somorjai, K.R. McCrea, J. Zhu, *Top. Catal.* 18(**2002**)157-166

[168] J. Wintterlin, T. Zambelli, J. Trost, J. Greeley, M. Mavrikakis, *Angew. Chem.* 115(**2003**)2956-2959

[169] J. Wintterlin, T. Zambelli, J. Trost, J. Greeley, M. Mavrikakis, *Angew. Chem. Int. Ed.* 42(**2003**)2850-2853

[170] M. Giesen, *Prog. Surf. Sci.* 68(**2001**)1-153

[171] F. Besenbacher, J.K. Norskov, *Prog. Surf. Sci.* 44(**1993**)5-66

[172] W.W. Pai, N.C. Bartelt, M.R. Peng, J.E. Reutt-Robey, *Surf. Sci.* 330(**1995**)L679-L685

[173] T. Zambelli, J.V. Barth, J. Wintterlin, *Phys. Rev. B* 58(**1998**)12663-12666

[174] O. Nakagoe, K. Watanabe, N. Takagi, Y. Matsumoto, *Phys. Rev. Lett.* 90(**2003**)226105

[175] K. Morgenstern, K. F. Braun, K. H. Rieder, *Phys. Rev. Lett.* 93(**2004**)056102

[176] H. Brune, *Surf. Sci. Rep.* 31(**1998**)121

[177] R. Kalousek, M. Schmid, A. Hammerschmid, E. Lundgren, P. Varga, *Phys. Rev. B* 68(**2003**)233401

[178] X. L. Zhou, J. M. White, B. E. Koel, *Surf. Sci.* 218(**1989**)201

[179] P. Messina, A. Dmitriev, N. Lin, H. Spillmann, M. Abel, J. V. Barth, K. Kern, *J. Am. Chem. Soc.* 124(**2002**)14000

[180] N. Lin, A. Dmitriev, H. Spillmann, P. Messina, M.A. Lingenfelder, S. Stepanow, J.V. Barth, K. Kern, *AIP Conference Proceedings* 696(**2003**)144

[181] S. Leininger, B. Olenyuk, P. J. Stang, *Chem. Rev.* 100(**2000**)853

[182] B. J. Holliday, C. A. Mirkin, *Ang. Chem. Int. Ed.* 40(**2001**)2022

[183] M. Ruben, J. Rojo, F. J. Romero-Salguero, L. H. Uppadine, J. M. Lehn, *Ang. Chem. Int. Ed.* 43(**2004**)3644

[184] B. Moulton, K. J. Zaworotko, *Chem. Rev.* 101(**2001**)1629

[185] S. Kitagawa, R. Kitaura, S. Noro, *Ang. Chem. Int. Ed.* 43(**2004**)2334

[186] O. M. Yaghi, M. O′Keeffe, N. W. Ockwig, H. K. Chae, M. Eddaoudi, J. Kim, *Nature* 423(**2003**)705

[187] L. R. Macgillivray, S. Subramanian, M. J. Zaworotko, *Chem. Comm.* (**1994**)1325

[188] X. Xu, M. Nieuwenhuyzen, S. L. James, *Ang. Chem. Int. Ed.* 41(**2002**)764

[189] A. B. Mallik, S. Lee, E. B. Lobkovsky, *Cryst. Growth. Des.* 5(**2005**)609

[190] X. C. Guo, R. J. Madix, *Surf. Sci.* 341(**1995**)L1065

[191] B. G. Frederick, M. R. Ashton, N. V. Richardson, T. S. Jones, *Surf. Sci.* 292(**1993**)33

[192] S. Poulston, R. A. Bennet, A. H. Jones, M. Bowker, *Phys. Rev. B* 55(**1997**)12888

[193] M. Bowker, S. Haq, R. Holroyd, P. M. Parlett, S. Poulston, N. V. Richardson, *J. Chem. Soc. Faraday Trans.* 92(**1996**)4683

[194] J. Lee, S. Ryu, S. K. Kim, *Surf. Sci.* 481(**2001**)163

[195] A. Dmitriev, H. Spillmann, M. Lingenfelder, N. Lin, J. V. Barth, K. Kern, *Langmuir* 20(**2004**)4799

[196] C. O. Dietrich-Buchecker, J. P. Sauvage, *Chem. Rev.* 87(**1987**)795

[197] D. B. Amabilino, J. F. Stoddart, *Chem. Rev.* 95(**1995**)2725

[198] F. Voegtle, T. Duennwald, T. Schmidt, *Acc. Chem. Res.* 29(**1996**)451

[199] M. Fujita, *Acc. Chem. Res.* 32(**1999**)53

[200] T. Hoshimo, M. Miyauchi, Y. Kawaguchi, H. Yamaguchi, A. Harada, *J. Am. Chem. Soc.* 122(**2000**)9876

[201] A. Bogdan, M. O. Vysotsky, T. Ikai, Y. Okamoto, V. Boehmer, *Chem. Eur. J.* 10(**2004**)3324

[202] V. Balzani, A. Credi, F. M. Raymo, F. J. Stoddart, *Ang. Chem. Int. Ed.* 39(**2000**)3348

[203] D. A. Leigh, J. K. Y. Wong, F. Dehez, F. Zerbetto, *Nature* 424(**2003**)174

[204] M. C. Jimenez-Molero, C. Dietrich-Buchecker, J. P. Sauvage *Chem. Comm.* (**2003**)1613

[205] E. Katz, O. Lioubashevsky, I. Wilner, *J. Am. Chem. Soc.* 126(**2004**)15520

[206] J. P. Sauvage, *Chem. Comm.* (**2005**)1507

[207] L. Fabbrizzi, M. Licchelli, P. Pallavicini, *Acc. Chem. Res.* 32(**1999**)846

[208] T. R. Kelly, H. de Silva, R. A. Silva, *Nature* 401(**1999**)150

[209] N. Koumura, R. W. J. Zijistram R. A. van Delden, N. Harada, B. L. Feringa, *Nature* 401(**1999**)152

[210] A. Harada, *Acc. Chem. Res.* 34(**2001**)456

[211] D. A. Leigh, M. Lubonska, S. M. Mendoza, E. M. Perez, P. Rudolph, G. Theobaldi, F. Zerbetto, *Nature Materials* 4(**2005**)704

[212] R. A. van Delden, M. K. T. rer Wiel, M. M. Pollard, J. Vicario, N. Koumura, B. Feringa, *Nature* 437(**2005**)1337

[213] C. A. Fustin, S. Haq, A. Wingen, C. Gregoire, R. Raval, P. Dumas, J. S. Hannam, D. A. Leigh, P. Rudolf, *Surf. Sci.* 580(**2005**)57

[214] Y. H. Lee, S. S. Jang, W. A. Goddard III, *J. Am. Chem. Soc.* 127(**2005**)4959

[215] S. S. Jang, Y. H. Jang, Y. H. Kim, W. A. Goddard III, A. H, Flood, B. W. Laursen, H. R: Tseng, J. F. Stoddart, J. O. Jeppesen, J. Wook Choi, D. W. Steuerman, E. Delonno, J. R. Heath, *J. Am. Chem. Soc.* 127(**2005**)1563

[216] Y. Liu, A. H. Flood, P. A. Bonvallet, S. A. Vignon, B. H. Northtrop, H. R. Tseng, J. O. Jeppesen, T. J. Huang, B. Brough, M. Baller, S. Magonov, S. D. Solares, W. A. Goddard, C. M. Ho, J. F. Stoddart, *J. Am. Chem. Soc.* 127(**2005**)9745

[217] C. O. Dietrich-Buecker, J. P. Sauvage, J. M. Kern, *J. Am. Chem. Soc.* 106(**1984**)3043

[218] M. Cesario, C. O. Dietrich-Buchecker, J. Guilhem, C. Pascard, J. P. Sauvage, *Chem. Comm.* (**1985**)244

[219] S. Stepanow, N. Lin, D. Payer, U. Schlickum, F. Klappenberger, G. Zoppelloro, M. Ruben, H. Brune, J.V. Barth, K. Kern, *Angew. Chem. Int. Ed.* 46(**2007**)710

[220] H. Ihm, J. M. White, *J. Phys. Chem. B* 104(**2000**)6202

Appendix

Ionic hydrogen bonds controlling 2-dimensional supramolecular systems at a metal surface

Paper in press in "Chemistry, a European Journal"

D. Payer, A. Comisso, A. Dmitriev, T. Strunskus, N. Lin, C. Wöll,
A. DeVita, J. V. Barth, K. Kern

Supramolecular self-assembly of molecular building blocks on well-defined substrates provides appealing opportunities to engineer low-dimensional nanostructures [A1]. Molecules with functional groups for hydrogen bonding have been widely employed, especially carboxyl groups because of their ability to form self-complementary dimer synthons, that is, pairing of $OH \cdots O$ hydrogen bonds, which enhances the strength of the hydrogen bonding considerably [A2, A3]. A crucial requirement in the stability of these structures is the integrity of the carboxyl groups upon adsorption onto surfaces, as it was shown that under certain conditions the carboxyl groups may undergo deprotonation to create carboxylate functions [A4 - A11]. This process destabilizes the dimer synthons and introduces new possibilities for intermolecular interactions. In particular, if the carboxylate groups stay charged upon adsorption onto a surface, this could enable the formation of stronger intermolecular ionic hydrogen bonds, which are a special class of hydrogen bonds that form between ionic donors (acceptors) and neutral acceptors (donors) and have bond strength up to one-third of the strength of covalent bonds [A12, A13]. Ionic hydrogen bonds may represent a new type of motif-controlling functional elements to assemble supramolecular structures at surfaces under solvent-free conditions. To understand the role of ionic hydrogen bonds in supramolecular assembly processes we studied 1,3,5-benzenetricarboxylic acid (trimesic acid, TMA) (Figure A.1, inset) on Ag(111) under ultrahigh vacuum as a model system by scanning tunneling microscopy (STM), scanning tunneling spectroscopy (STS), X-ray photoelectron spectroscopy (XPS), near-edge X-ray absorption fine structure (NEXAFS), and molecular dynamics calculations. Our previous study showed that TMA forms a honeycomb network structure mediated by neutral hydrogen bonds at room temperature [A5]. Here we show that upon annealing above 300K the carboxyl groups of the TMA molecules are gradually deprotonated. Above 420K one out of three carboxyl groups per TMA molecule is deprotonated, and an irreversible phase transformation occurs. The new phase is densely packed, stabilized by ionic hydrogen bonds between the remaining carboxyl groups and the charged carboxylate moieties. The ionic hydrogen bonds effectively overcome the Coulomb repulsion between the charged species. To our knowledge this is the first time that ionic hydrogen bonds and their role in supramolecular organization under solvent-free, "dry", ultrahigh-vacuum conditions have been comprehensively studied. Our findings deepen the understanding of hydrogen bonding in the vicinity of metal surfaces and expand the design capabilities to realize 2D supramolecular systems.

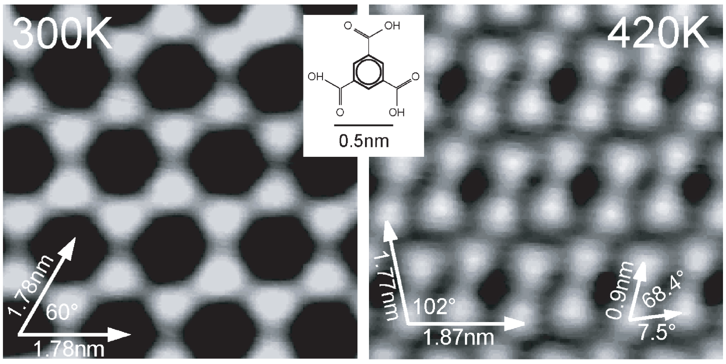

Figure A.1 STM topographs of a) the honeycomb and b) quartet structures formed at 300 and 420 K, respectively. In both topographs the triangular appearance of the TMA molecules indicates flat-lying molecules. The inset shows the molecular model of the TMA molecules. Tunneling current: 0.5 nA, bias voltage: 0.5 V.

Figure A.1a shows an STM topograph of the TMA structure after annealing the sample to 300K. The molecules are aggregated into the known honeycomb structure in which each molecule is connected to three neighboring molecules through carboxylic acid dimer synthons between the carboxyl groups. This gives a hexagonal lattice with a lattice constant of 1.78 ± 0.05 nm and an $O\cdots O$ distance in the hydrogen bonds of 0.34 ± 0.05 nm, in agreement with previous results obtained with TMA on other substrates [A11, A14 - A16] Attempts to determine the registry of the honeycomb structure with respect to the Ag(111) surface were not successful, because we could not resolve the Ag(111) atomic lattice and the honeycomb structure simultaneously.

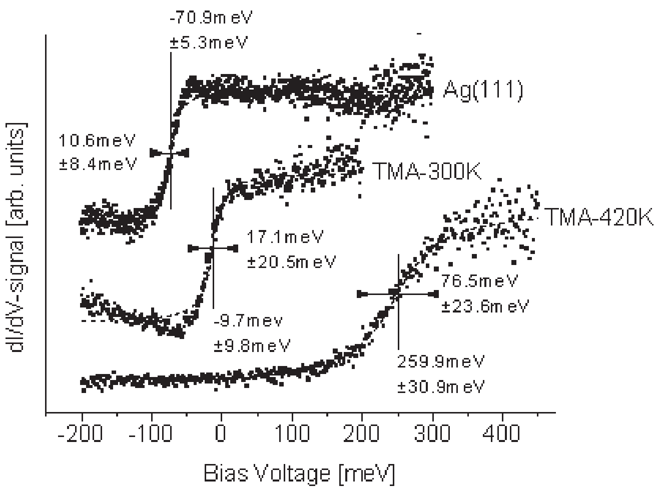

Figure A.2 ST spectra acquired on clean Ag(111), the honeycomb structure, and the quartet structure. The spectra were normalized to a constant onset height and shifted along the y axis for better discrimination.

The ST spectra acquired on the clean Ag(111) surface show a sharp step-like feature with an onset at an energy E0 of -70.9±5.3mV and a width of 10.6±8.4mV. In contrast ST spectra acquired on the honeycomb phase show an onset at -9.7±9.8mV and are broadened to 17.1±20.5mV with the flat plateau extending above 1500 mV, as shown in Figure A.2. Because there is no significant difference between ST spectra taken at different positions of the TMA honeycomb structure, we can rule out that the onset is a signature of TMA molecular orbitals. We attribute this onset to the surface state formed by a two-dimensional electron gas, but shifted to higher energy and broadened by the weakly adsorbed TMA molecules. It has been reported that weakly adsorbed noble gas atoms have similar effects on the surface state of (111) surfaces of noble metals [A17 - A19]. Thus, the STS data suggest weak surface bonding, in agreement with the generally accepted picture that planar aromatic hydrocarbons are weakly π-bonded with the benzene rings parallel to the close-packed noble-metal substrate [A20, A21]

Measurements by XPS and NEXAFS provided complementary insight into the chemical states and the bonding geometry of the TMA molecules in the structure at 300K, corroborating the picture obtained by the STM measurements. The upper curve in Figure 3a shows the C 1s signal of the 300K structure, and the upper curve in Figure 3b shows the O1s signal of the 300K structure. In the C 1s spectrum two well-separated peaks are

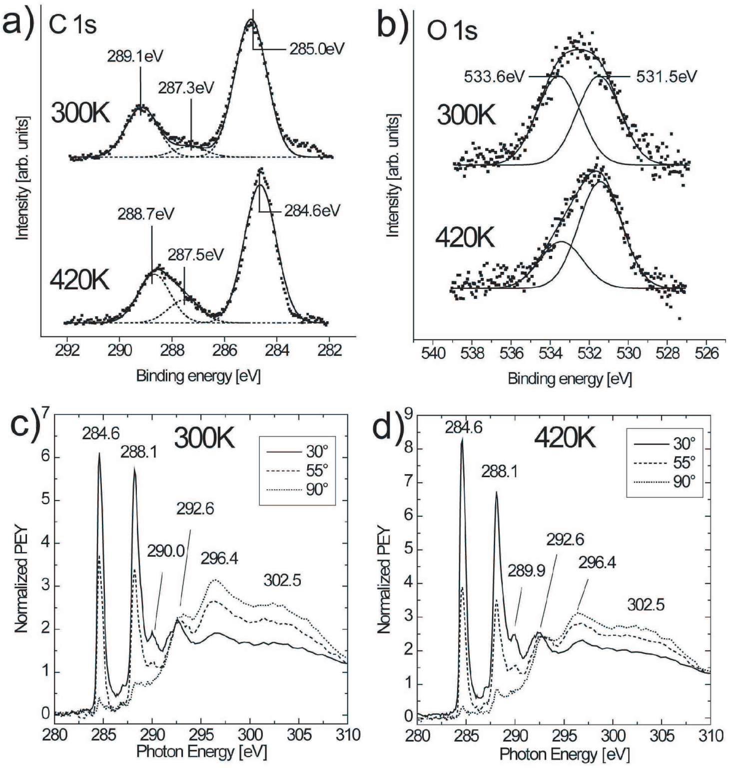

Figure A.3 X-ray photoelectron spectra in a) the C 1s and b) the O1s regions, acquired on samples annealed to 300 K (upper graphs) and 420 K (lower graphs). NEXAFS spectra of the c) 300 K and d) 420 K phases recorded at the C K-edge. Solid and dashed lines indicate spectra obtained at different angles of incidence of the synchrotron light (90° means normal incidence to the Ag(111) surface).

identified, a larger one at a binding energy (BE) of 285.0eV, which is assigned to the six carbon atoms in the benzene ring, and a smaller one at a BE of 289.1eV, which is assigned to the three carbon atoms in the carboxyl groups, in accordance with previous reports [A10, A17 - A22]. The fit of the spectrum to Gaussian-shaped peaks with a full width at half-maximum (FWHM) of 1.4eV is improved by adding a small additional peak with a BE of 287.3eV, which is assigned to a small amount of carbon atoms of TMA molecules in a different chemical state or can be attributed to impurities on the surface such as adsorbed CO. The O 1s signal consists of a broad symmetric peak, which is a convolution of the signals of oxygen in hydroxyl groups (BE of 533.6eV) and carbonyl groups (BE of 531.5eV), in accordance with similar systems bound by hydrogen bonds between carboxyl groups.[A10, A18 - A20] The C 1s and O1s XP spectra clearly show that after annealing to 300 K the carboxyl groups of the TMA molecules are still protonated, and dimer hydrogen bonds are formed between carboxyl groups.

The NEXAFS spectra of the 300 K honeycomb structure are displayed in Figure 3c, in which several pronounced π^*-resonances are clearly discernible. Assignment was made in analogy to that for TPA, which was thoroughly discussed in reference [22]. The π^*-resonance at 284.6 eV is assigned to transitions related to the carbon atoms of the aromatic ring, whereas the prominent peak at 288.2 eV and the shoulder at 290.0 eV are assigned to transitions related to the carboxyl carbon atoms. At higher energy several σ^*-transitions at 292.6, 296.4, and 302.5 eV can be identified. The π^*-resonances of the benzene carbon atoms and of the carboxyl carbon atoms both show pronounced dichroism with almost completely vanishing intensity for normal photon incidence (90°). The average tilt angles calculated from the observed dichroism are 18°±7° and 20°±7° for the benzene and carboxyl parts of the molecule, respectively. These data indicate that the carboxyl groups are coplanar with the benzene rings. There is a significant deviation of the obtained average tilt angle from the 0° expected for perfectly flat-lying molecules. Frequently, average tilt angles of up to 10° are observed by NEXAFS spectroscopy even for perfectly flatlying aromatic molecules on metal surfaces [A23A25]. Tilting has been attributed to adsorption-induced nonplanar intramolecular distortions involving bending of the C-H bonds out of the ring plane. Therefore, a plausible explanation of our data is that the vast majority of the molecules are indeed adsorbed in a flat geometry, and the deduced average tilt angle is caused by the above-mentioned distortions and a small number of molecules deviating significantly from a flat adsorption geometry. Such molecules may be adsorbed at defects or step edges.

After annealing the sample to 420 K the open TMA honeycomb structure is transformed irreversibly into a dense packed structure, as shown in the STM image in Figure A.1b. The basic motif of this structure is a TMA quartet, a group of four closely packed TMA molecules in a rhombic arrangement with a side length of 0.9 nm and an angle of 68.4°. These quartet units are repeated in an oblique lattice with lattice constants of 1.87±0.05, 1.77±0.05 nm and an angle of 102°. Similar to the 300 K structure the registry of the 420 K structure with respect to the Ag(111) substrate could not be determined. The ST spectra acquired on the TMA quartet structure reveal pronounced changes in the surface electronic structure. The spectrum reproduced in Figure 2 shows a broad onset around 259.9±30.9 mV with a width of 76.5±23.6 mV. Again there is no spatial variation of the STS signal, hence we attribute the onset feature in the ST spectrum to the surface-state electrons. It is known that stronger adsorbatesubstrate interactions can lead to substantial changes in the electronic structure of the substrate and even quenching of the surface state. The observed significant deviation of the ST spectrum of the 420 K structure from that of the weakly bound neutral adsorbate implies notable impact of the TMA quartets on the surface electronic state.[A26 - A28]

A detailed analysis of the XPS measurements on the close-packed 420 K structure reveals a distinct change in the chemical state of the TMA molecules. The C 1s signal shown in the lower part of Figure A.3a still consists of two peaks, but the smaller one at a BE of 289.0 eV is broadened relative to the small peak in the 300 K structure. The C 1s signal was fitted by three Gaussian-shaped peaks with an FWHM of 1.4 eV, and the obtained binding energies were compared to the results of the 300 K structure and to published data. The smaller peak has been deconvoluted into two peaks, one for carbon atoms in the carboxyl groups at a BE of 288.7 eV, in good agreement with the 300 K structure, and one for carbon atoms in a new state at a BE of 287.5 eV. This new peak is assigned to carbon atoms in carboxylate groups, in agreement with previous measurements [A4, A8, A10, A35 - A40]. Carbon atoms in the benzene ring are found at a BE of 284.6 eV, also in good agreement with the 300 K structure. The relative peak areas, with the total area of the spectrum normalized to the nine carbon atoms in a TMA molecule, were 5.9 for the benzene peak, 2.1 for the carboxyl peak, and 1.0 for the carboxylate peak. The areas of the carboxyl and carboxylate peaks sum to three carbon atoms, and this implies that the carboxylate groups have their origin in the carboxyl groups. The O1s signal (Figure A.3b, lower curve) became asymmetric after annealing to 420 K and could no longer be fitted with two equal Gaussian-shaped peaks. Instead, the asymmetric signal clearly shows the formation of oxygen atoms in different chemical states, in contrast to those found in the purely hydrogen-bonded honeycomb arrangement [A4, A17 - A20]. A quantitative interpretation of the O1s signal is much more difficult than for the C 1s signal, as the chemical neighborhood and therefore the number of different kinds of oxygen atoms in the 420 K structure are not known. Therefore, we refrained from a quantitative analysis of the O1s signal. In summary, the appearance of new chemical states in the carbon and oxygen spectra is attributed to the often-observed deprotonation of carboxyl groups upon adsorption on metal surfaces and the formation of carboxylate groups [A5, A7, A9, A11, A29]. Based on the relative peak areas in the C 1s signal, the number of carbon atoms is 2.1 in carboxyl groups and 1.0 in carboxylate groups. Considering the high symmetry of the structure, we conclude that after annealing to 420 K one out of three carboxyl groups per molecule is deprotonated and transformed into a carboxylate group.

The NEXAFS spectra of the 420 K structure are displayed in Figure A.3d. Upon warming to 420 K and measuring the sample again at 300 K the dichroism of the π^*-resonances remains very pronounced (see Figure 3d). The calculated average tilt angles are now 14°±5° for the benzene rings and 23°±5° for the carboxyl groups. This indicates that the molecules remain in a essentially flat-lying geometry on the surface. It seems that the carboxyl groups on average are now tilted by 5°-10° out of the plane of the benzene ring. Comparing the NEXAFS spectra obtained for the two phases one notices only small differences; in particular, the intensity of the carboxyl π^*-resonance is not much reduced relative to the π^*-resonance of the benzene ring. These changes are consistent with only partial deprotonation of the carboxyl groups. For complete deprotonation we would expect a much more pronounced decrease of the carboxyl π^*-resonance, as has been observed by us in a related system, that is, terephthalic acid (TPA) on Cu(100) [A10].

The deprotonation of carboxyl groups upon adsorption on metal surfaces has been observed in many other systems, but usually the oxygen atoms of the carboxylate groups bind to substrate atoms, and this tilts the whole molecule to an upright-standing configuration [A5, A7, A9, A11, A29]. In contrast to these results, our STM and NEXAFS measurements for the 420 K structure clearly provide evidence for flat-lying TMA molecules containing one carboxylate group. This suggests that the carboxylate groups are engaged in lateral intermolecular binding by forming ionic hydrogen bonds with neutral carboxyl groups of the neighboring TMA molecules. A fundamental and evident precondition for the formation of ionic hydrogen bonds is that the carboxylate group is still charged and the charge is not distributed over the entire molecule or compensated by the metallic substrate.

To gain information about the charge states of the partially deprotonated molecule, ab initio calculations were performed on a single TMA molecule containing one carboxylate group (denoted "deprotonated" TMA molecule in what follows). Then classical molecular dynamics calculations were performed to reproduce the quartet structure and to gain better understanding of the interplay between charged carboxylate groups and the neutral carboxyl groups.

We performed ab initio calculations of the 0 K structure of a single TMA molecule placed on a five-layer slab of Ag(111) (Figure A.4). The solid curve in Figure 4a shows the response of the electronic charge density to deprotonation. This is computed from the electron densities ρ_{prot} and ρ_{deprot} of the protonated and deprotonated molecule systems as -e*(ρ_{deprot}-ρ_{prot}). The atomic positions in both calculations are those obtained for the relaxed protonated molecule adsorbed on the metal surface. The electron density difference is integrated over the xy planes and plotted as a function of the z variable (the origin of the z axis corresponds to the first atomic layer of the Ag surface).

Deprotonation involves loss of a proton screened by release of some elec-

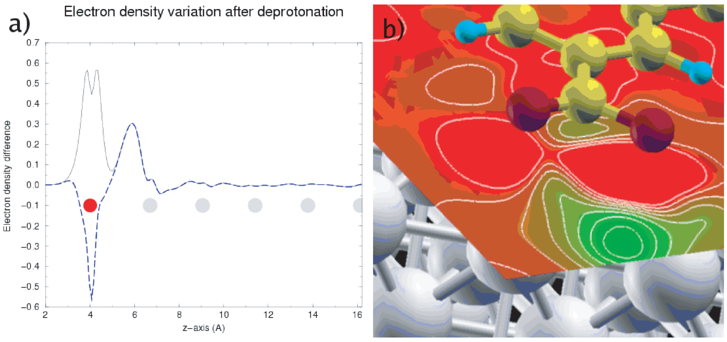

Figure A.4 a) Charge-density variations upon deprotonation of a TMA molecule adsorbed on a slab of Ag(111). All quantities are integrated over the xy plane and plotted along the z direction. The blue dashed curve refers to the total charge density variation, which yields a negative surface dipole density profile. The electronic contribution to the total charge density variation is shown in the solid curve (see text). The red and gray filled circles correspond to the z positions of the adsorbed molecules and the first four layers of the metal substrate, respectively. b) The electron-density depletion (or positive charge-density accumulation) corresponding to the peak centered at z=-0.9$\mathring{A}$ is also visible as a green lobe located under the carboxylate group (the contour plot of the density difference is taken at z=-0.7$\mathring{A}$).

tron density to the surface, so that the net final charge of the molecular ion is a value q between 0 and -e. The release of electron density corresponds to the prominent positive (double) peak of the solid line centered at the position z=-2.8$\mathring{A}$ of the adsorbed molecule (the relaxed adsorption geometry of the molecule was in all cases flat). A second, lower peak of the solid line is centered at about -0.9$\mathring{A}$, that is, in the region between the molecule and the first surface layer of the metal substrate. This peak corresponds to a surface screening effect mostly localized under the missing proton (see also Figure A.4b). As above, a positive peak here represents the loss upon deprotonation of some of the negative charge density originally screening the proton. The total charge-density variation upon deprotonation is simply the sum of its electronic contribution described by the solid curve in Figure A.4a and the negative contribution due to the loss of proton charge (modeled by a Gaussian of width 0.3$\mathring{A}$ centered on the proton site and normalized to -e). The total charge-density variation is represented by the blue dashed line in Figure A.4a, and its overall shape is that of the charge-density profile of a negative surface dipole layer. To estimate the charge q of the molecule after deprotonation we integrated the total charge density variation discussed above over the z interval "occupied" by the molecule. This interval can be taken to start at any z0 value located well inside the vacuum region where all densities are zero and end at an upper value z1 located between the molecular plane and the first Ag layer.

The value for z1 was obtained by imposing the neutrality condition on the protonated molecule. The value of q was then simply obtained by integration of the blue dashed curve in Figure 4a between z0=-5.0 $\AA$ and z1=-1.48$\AA$. These calculations predict a total charge q=-0.3 e for the deprotonated TMA molecule. Note that in the calculations described so far and illustrated by Figure A.4 the molecule/ slab systems were in all cases neutral: in particular, one electron was subtracted from the overall system together with the proton to obtain the model used for the geometry in the deprotonated state. Imposing charge neutrality on the deprotonated system and repeating the calculation yields similar results, with a somewhat higher charge q=-0.5 e associated with the adsorbed deprotonated molecule. Overall, these results predict the formation of a negative surface dipole layer on the Ag(111) substrate upon deprotonation, corresponding to the blue curve distribution in Figure A.4a. We note that a physical picture of temperature-induced deprotonation with formation of a negative dipole lowering the electrostatic potential in the surface region is consistent with the upshift of the surface-state energy level visible in the ST spectrum of Figure A.2 [A26 - A28].

The classical MD force field can be used to model the presence of charged surface species by appropriate modification of the partial Coulomb charges. As we are investigating the possibility of supramolecular assembly between similarly charged molecular ions, the charges on the oxygen atoms of the carboxyl group after the removal of the hydrogen atom were adjusted to achieve the overall calculated total ionic charge of q=-0.5 e corresponding to the least favorable (most repulsive) case for assembly in our calculated range.

The partial charges used are reported in Figure A.5a. As the TMA molecules are always adsorbed in a flat-lying geometry on the surface, we performed two-dimensional classical MD simulated annealing runs, with the further constraint of describing the molecules as rigid bodies. The interaction between the molecules was modeled by a superimposition of a Coulomb term obtained from the partial charges and a short-range repulsive term designed to ensure that the molecules do not overlap. The electrostatic screening of the metal surface was taken into account by introducing mirror images of the partial point charges of the potential [A30].

We then considered an isolated group of four molecules to find a stable candidate for a model structure of the quartet units revealed by the experimental observations. Consistent with the XPS results and the high symmetry of the structure, we assumed that each molecule bore one carboxylate

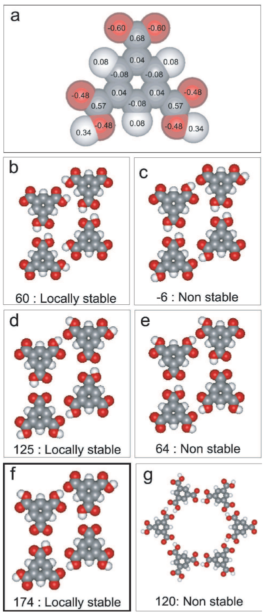

Figure A.5 (a) Effective atomic point charges of a deprotonated TMA molecule. The total molecular charge of -0.5 e (mostly localized on the carboxylate group) is consistent with the results of an ab initio calculation on a deprotonated systems of total charge -e (see text); bf) Ball-and-stick models of the different investigated configurations of the quartet molecular unit are reported with indication of their stability (structures corresponding to local minima are denoted here as "metastable"). The interaction energy per molecule calculated with the classical force field is given for each structure in units of 10^{-4}a.u. g) Model of a hypothetical deprotonated honeycomb structure, which is found to be unstable in simulations using the force field.

group. We explored the stability of different configurations by systematically changing the positions of the two remaining carboxyl protons of each TMA molecule in the unit cell. Furthermore, since the STM images showed C2 symmetry, we limited the search to the different proton configurations that have this symmetry, as shown in Figure A.5bf. This cluster structure was used (with minor adjustments obtained by MD annealing) to produce a periodic pattern compatible with the experimental dimensions of the surface unit cell. The lowest energy structure found corresponds to the configuration shown in Figure A.5f. The final equilibrium structure obtained in this way, shown in Figure A.6a, is in good agreement with the experimentally observed structure. All charged carboxylate groups are bound to neutral carboxyl groups, and furthermore two different kinds of carboxylate groups exist in the 420 K structure, highlighted in Figure A.6a and magnified in Figure A.6b and c. Figure A.6b shows the first kind of ionic hydrogen bond of this structure, which stabilizes a TMA dimer in which the carboxylate group is bound to a single carboxyl group. Figure A.6c shows the second kind of ionic hydrogen bond, in which the carboxylate group is bound to two carboxyl groups on different molecules. These different bonds to different molecules ultimately allow the dimers to assemble into the observed chain structure. The calculated O$\cdots$O distance for both ionic hydrogen bonds was 0.256 nm.

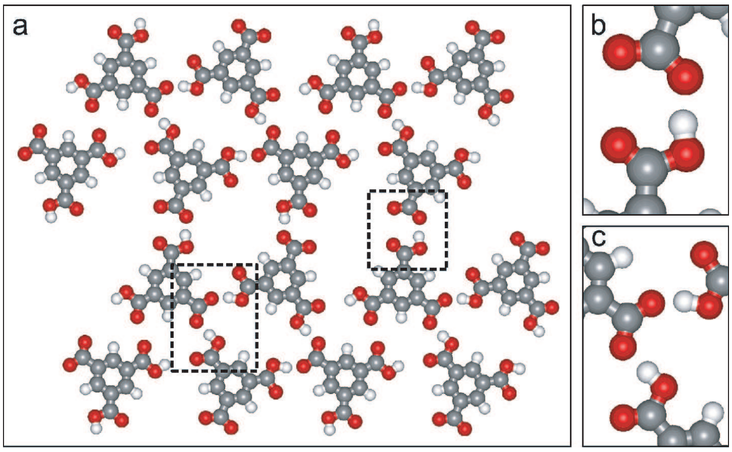

Figure A.6 (a) Calculated structure of the most stable configuration of the building block (Figure A.5 f). The two different kinds of ionic hydrogen bonds are outlined. b) Ionic hydrogen bond between one carboxylate group and one carboxyl group. c) Ionic hydrogen bond between one carboxylate group and two carboxyl groups.

In addition, the possibility of forming a honeycomb structure from deprotonated TMA molecules was investigated, as shown in Figure A.5g. We note that a honeycomb structure undergoing a single deprotonation per molecule as shown in Figure A.5g would involve the same overall number of hydrogen bonds as observed in the predicted stable structure of Figure A.5f (as the overall residual number of hydrogen atoms would be the same in the two structures). However, the hexagonal arrangement would imply pairs of adjacent negatively charged and mutually repulsive oxygen atoms, located on the non-hydrogen-bonded side of facing carboxyl group pairs. This cannot happen in the denser packing experimentally observed, in which carboxyl group pairs never face each other and can thus be connected by at most one hydrogen bond. As one can see from the interaction energies reported in Figure A.5, the deprotonated hexagonal phase (honeycomb structure) is significantly less stable than the densely packed structure. Thus a structural transformation would presumably occur upon deprotonation of the carboxyl groups. The preferred arrangement of the molecules upon deprotonation is determined by the concurrent need to maximize the number of hydrogen bonds, while minimizing the Coulomb repulsion between negatively charged deprotonated carboxyl groups. In this scenario, the honeycomb structure becomes unstable upon deprotonation and the system "collapses" into a more densely packed structure in which ionic hydrogen bonds play an important role. The phase transition is driven by deprotonation and is thus irreversible, consistent with the experimental findings.

In conclusion, our experiments and calculations suggest that intermolecular ionic hydrogen bonds offer novel possibilities to steer the assembly of supramolecular structures on surfaces. The realized supramolecular structures are notably stable in the absence of counterions (necessary in solvent phases to stabilize ionic hydrogen bonds) due to the charge-screening effect of the metal surface. This process implies that the energy gain resulting from intermolecular ionic hydrogen bonds exceeds that of potential molecule to substrate bonds. The latter depends on the chemistry of the substrates. For example, when employing Cu surfaces, deprotonated TMA or related species can be engaged in carboxylate anchoring to the surface rather than forming intermolecular ionic hydrogen bonds [A11, A31]. In general, chemically inert substrates like Ag and Au are more appropriate for formation of ionic hydrogen bond with adsorbed carboxylate species.

All measurements were made in ultra high vacuum (UHV) systems equipped with standard equipment for sample cleaning and preparation. The Ag(111) surface was cleaned by repeated cycles of sputtering with 500eV Ar^+-ions and subsequent annealing to 800K. Commercially available TMA (Aldrich, purity 95%) was deposited onto the Ag(111) surface by means of organic molecular beam epitaxy (OMBE), with the crucible containing the TMA powder held at a temperature of 473K during deposition. The Ag(111) substrate was kept at a temperature of 100K during deposition, followed by annealing steps to 300K and 420K , respectively. The annealing time had no influence on the self-ordering process. The coverage was always in the submonolayer range, typically a quarter to a third of the Ag(111) surface was covered by TMA molecules. STM and STS data were acquired using a home-built Besocke type STM operated at a temperature of 5K. The STM measurements were performed in the constant-current mode with electrochemically etched W-tips. ST-spectra were recorded using a lock-in amplifier set to a frequency of 5kHz and a modulation-amplitude of 10mV. The cleanness of the tip was checked by acquiring ST-spectra on the clean Ag (111) surface, which showed the typical onset of the two-dimensional surface state at an energy E0 of -70.9±5.3meV and a width of 10.6±8.4meV [A32 - A34]. The XPS and the NEXAFS data were acquired at the HE-SGM Beamline of the BESSY II Synchrotron Radiation Facility in Berlin at a temperature of 300K. The XP-spectra were recorded with beam energies of 400eV for the Carbon 1s peak and 670eV for the Oxygen 1s peak, both with a pass-energy of the analyzer offset to 50eV. Additional spectra were made using the Al K_α-radiation of a laboratory source and a pass-energy of the analyzer of 100eV. The spectra were referenced to the Ag $3d_{5/2}$-line at 368.2eV. The XP spectra were fitted after a linear background substraction with a suitable number of Gaussian-shaped peaks, linked to carbon and oxygen atoms in different states within the structures. These peaks could be allocated to the different states of carbon and oxygen in the TMA molecules and the areas of the peaks were used as a measure for the amount of atoms within these states [A10, A15 - A40]. All NEXAFS spectra were recorded in the partial electron yield mode (retarding voltage -150eV) using a double channel plate as electron detector. For the methods used for energy-calibration and normalization of the spectra see Ref. [A10]. In our theoretical investigation we used a combination of classical and ab-initio molecular dynamics (MD) methods. All our first principle calculations were carried out using the Car-Parrinello method [A41], with Troullier Martins norm-conserving pseudopotentials [A42] and a gradient corrected exchange-correlation functional [A44]. The metallic systems were treated within the scheme of Ref. [A26], using a smearing energy width of E_s=0.25eV. The Brillouin zone sampling was limited to the gamma point only. The plane wave expansion was truncated at an energy cutoff of 50Ry. In calculations including surfaces this cutoff was increased to 80Ry. We initially performed ab-initio simulations of isolated molecules. The electron densities were used to determine a classical potential according to the well-established procedure of Refs. [A45 - A47]: the Poisson equation was first solved to obtain the electrostatic potential. The effective partial Coulomb point charges, positioned on the core ions, were then determined from the best fit of the electrostatic potential outside a Van der Waals exclusion area defined by the atomic effective radii (0.38nm, 0.33nm and 0.29nm for C, O and H atoms respectively) [A45].

This research was funded by the program EUROCORES-SONS of the European Science Foundation. AC acknowledges funding from Area Science Park of Trieste.

[A1] J. V. Barth, G. Constantini, K. Kern, Nature 2005, 473, 671-679
[A2] J. V. Barth, J. Weckesser, N. Lin, A. Dmitriev, K. Kern, Appl. Phys. A 2003, 76, 645-652
[A3] S. DeFeyter, F. C. DeSchryver, Chem. Soc. Rev. 2003, 32, 139-150

[A4] B. Immaraporn, P. Ye, A. J. Gellman, J. Phys. Chem. B 2004, 108, 3504-3511
[A5] N. Lin, D. Payer, A. Dmitriev, T. Strunskus, C. Wöll, J. V. Barth, K. Kern Angew. Chem. 2005, 117, 1512-1515; Angew. Chem. Int. Ed. 2005, 44, 1488-1491.
[A6] M. Bowker, E. Rowbotham, F. M. Leibsle, S. Haq, Surf. Sci. 1996, 349, 97-110
[A7] J. G. Lee, J. Ahner, D. Mocuta, S. Denev, J. T. Yates, J. Chem. Phys. 2000, 112, 3351-3357
[A8] B. Parker, B. Immaraporn, A. J. Gellmann, Langmuir 2001, 17, 6638-6646
[A9] D. S. Martin, R. J. Cole, S. Haq, Surf. Sci 2003, 539, 171-181
[A10] S. Stepanow, T. Strunskus, M. Lingenfelder, A. Dmitriev, H. Spillmann, N. Lin, J. V. Barth, C. Wöll, K. Kern, J. Phys. Chem. B 2004 108, 19392-19397
[A11] A. Dmitriev, N. Lin, J. Weckesser, J. V. Barth, K. Kern, J. Phys. Chem. B 2002, 106, 6907-6912
[A12] M. Meot-Ner (Mautner), Chem. Rev. 2005, 105, 213-284
[A13] D. Braga, A. Angelino, E. Tagliavini, F. Grepioni, J. Chem. Soc., Dalton Trans. 1998, 1961-1968
[A14] S. Griessl, M. Lackinger, M. Edelwirth, M. Hietschold, W. M. Heckl, Single Mol. 2002, 1, 25-31
[A15] Y. Ishikawa, A. Ohira, M. Sakata, C. Hirayama, M. Kunitake, Chem. Comm. 2002, 22, 2652-2653
[A16] G. J. Su, H. M. Zhang, L. J. Wan, C. L. Bai, T. Wandlowski, J. Phys. Chem. B 2004, 108, 1931-1937
[A17] R. Paniago, R. Matzdorf, G. Meister, A. Goldmann, Surf. Sci 1995, 325, 336-342
[A18] H. Hövel, B. Grimm, B. Reihl, Surf. Sci 2001, 477, 43-49
[A19] T. Andreev, I. Barke, H. Hövel, Phys. Rev. B 2004, 70, 2054261-20542613
[A20] S. Lehwald, H. Ibach, J. E. Demuth, Surf. Sci 1978, 78, 577-590
[A21] P. Yannoulis, R. Dudde, K. H. Frank, E. E. Koch, Surf. Sci 1987, 189, 519-528
[A22] T. Okajima, K. Teramoto, R. Mitsumoto, H. Oji, Y. Yamamoto, I. Mori, H. Ishii, Y. Ouchi, K. Seki, J. Phys. Chem. A. 1998, 102, 7093-7099
[A23] C. Mainka, P. S. Bagus, A. Schertel, T. Strunskus, M. Grunze, C. Wöll, Surf. Sci. 1995, 341, L1055-L1060
[A24] K. Weiss, S. Gebert, M. Wühn, H. Wadepohl, C. Wöll, J. Vac. Sci. Technol. A 1998, 16, 1017-1022

[A25] S. Lukas, S. Söhnchen, G. Witte, C. Wöll, ChemPhysChem 2004, 5, 266-270
[A26] R. Paniago, R. Matzdorf, G. Meister, A. Goldmann, Surf. Sci. 1995, 325, 336-342
[A27] W. Jacob, V. Dose, A. Goldmann, Appl. Phys. A 1986, 41, 145-150
[A28] S. A. Lindgren, J. Paul, L. Wallden, Surf. Sci. 1982, 117, 426-433
[A29] B. G. Frederick, Q. Chen, F. M. Leibsle, M. B. Lee, K. J. Kitching, N. V. Richardson, Surf. Sci 1997, 394, 1-25
[A30] M. Vladimirova, M. Stengel, A. De Vita, A. Baldereschi, M. Böhringer, K. Morgenstern, R. Berndt, W. D. Schneider, Europhys. Lett. 2001, 56, 254-260
[A31] A. Dmitriev, H. Spillmann, S. Stepanow, T. Strunskus, Ch. Wöll, A. P. Seitsonen, M. Lingenfelder, N. Lin, J.V Barth, K. Kern, ChemPhysChem 2006, 7, 2197-2204
[A32] J. Li, W. D. Schneider, R. Berndt, O. R. Bryant, S. Crampin, Phys. Rev. Lett. 1998, 81, 4464-4467
[A33] L. Bürgi, L. Petersen, H. Brune, K. Kern, Surf. Sci. 2000, 447, L157-L161
[A34] L. Bürgi, N. Knorr, H. Brune, M. A. Schneider, K. Kern, Appl. Phys. A 2002, 75, 141-145
[A35] L. H. Dubois, B. R. Zegarski, R. G. Nuzzo, Langmuir 1986, 2, 412-417
[A36] S. W. Han, S. W. Joo, T. H. Ha, Y. Kim, K. Kim, J. Phys. Chem. B 2000, 104, 11987-11995
[A37] M. Wühn, J. Weckesser, C. W öll, Langmuir 2001, 17, 7605-7612
[A38] G. Axelson, U. Ericson, A. Fahlman, K. Hamrin, J. Hedman, R. Nordberg, R. Nordling, K. Siegbahn, Nature 1967, 213, 70-71
[A39] D. L. Hoof, D. G. Tisley, R. A. Walton, J. Chem. Soc. Dalton Trans. 1973, 2, 200-204
[A40] U. Gelius, P. F. Heden, J. Hedman, B. J. Lindberg, R. Manne, R. Nordberg, C. Nordling, K. Siegbahn, Physica Scripta 1970, 2, 70-80
[A41] R. Car, M. Parrinello, Phys. Rev. Lett 1985, 55, 2471-2474
[A42] N. Troullier, J. L. Martins, Phys. Rev. B 1991, 43, 1993-2006
[A43] J. P. Perdew, Y. Wang, Phys. Rev. B 1992, 45, 13244-13249
[A44] J. VandeVondele, A. De Vita, Phys. Rev. B 1999, 60, 13241-13244
[A45] M. Vladimirova, G. Trimarchi, A. Baldereschi, J. Weckesser, K. Kern, J. V. Barth, A. De Vita, Acta Mat. 2004, 52, 1589-1595
[A46] M. Böhringer, K. Morgenstern, W. D. Schneider, R. Berndt, F. Mauri, A. De Vita, R. Car, Phys. Rev. Lett. 1999, 83, 324-327
[A47] J. V. Barth, J. Weckesser, G. Trimarchi, M. Vladimirova, A. De Vita, C. Cai, H. Brune, P. Günter, K. Kern, J. Am. Chem. Soc. 2002, 124, 7991-8000

Acknowledgments

First of all I want to say thanks to my parents, my brothers, my grandmother and the rest of my family for always supporting me and encouraging me in my work on this thesis.

I want thank Professor Klaus Kern, the director of my thesis, for giving me the opportunity to work in his group and for his guidance in accomplishing this thesis.

I am grateful to Dr. Nian Lin, who supervised this work. He was directly involved in the planning, realization, analysis and interpretation of our experiments and his ideas, help and abilities contributed a lot to the success of this thesis.

Thanks to the present and former group members Sebastian Stepanow, Alex Langner, Steven Tait, Alexandre Dmitriev, Franck Vidal and Frederick Leroy, for fruitful discussions and that they always had time to help me.

I also want to thank Dr. Mario Ruben and Professor Jean-Pierre Sauvage for the synthesis of molecules employed in this research and for helping me with their expertise in organic chemistry, Dr. Thomas Strunskus and Professor Christof Wöll for enabling me to perform synchrotron measurements and introduce me in the analysis of the so obtained data and Professor Johannes Barth, who was closely involved in the projects and always had time to bring in new ideas.

Wolfgang Stiepany, Wolfgang Heinz, Peter Andler and Andreas Koch have been always a help in solving technical problems or when machining was necessary.

Prof. Vincenzo Savona, Prof. Wolf-Dieter Schneider, Dr. Karl-Heinz Ernst and Prof. Pascual Jose Ignacio for finding time to participate on the examination.

Apart from people directly involved in the accomplishment of my thesis I want to thank Peter Wahl, Sören Neubeck, Lars Diekhöner, Robin Ohmann, Violetta Sessi, Thomas Weitz, Stephan Rauschenbach, Alexander Bittner, Thomas Classen, Michael Vogelgesang, Ralf Vogelgesang, Maggi Lingenfelder and all others for the pleasant time at the institute.

Curriculum vitae

Name	Dietmar Payer
Date of Birth	6. 12. 1976
Nationality	Austrian

January 2007	PhD thesis: ”Single-molecule level characterization of supramolecular systems at surfaces”
2003—2007	Research assistant in the group of Prof. Dr. K. Kern at the Max Planck Institute for Solid State Research in Stuttgart, Germany
2002—2003	Military Service
2002	Diploma thesis in the group of Prof. Dr. P. Varga at the Institut für Allgemeine Physik at the Vienna University of Technology: ”CO-Adsorption auf PtFe-Legierungsschichten”
1995—2002	Diploma studies in physics at the Vienna University of Technology, Vienna, Austria
1995	Matura at the Bundesrealgymnasium Mödling, Austria

Publications

Two-dimensional adatom gas bestowing dynamic heterogeneity on surfaces
N. Lin, D. Payer, A. Dmitriev, T. Strunskus, C. Wöll, J.V. Barth, K. Kern
Angewandte Chemie International Edition 44(**2005**)1488

Ionic hydrogen bonds in 2-dimensional supramolecular systems at metallic surfaces
D. Payer, A. Comisso, A. Dmitriev, T. Strunskus, N. Lin, C. Wöll, A. DeVita, J.V. Barth, K. Kern
Chemistry, a European Journal, in press

2D Supramolecular Assemblies of Benzene 1,3,5-tri-yl Tribenzoic Acid: Temperature-Induced Phase Transformations and Hierarchical Organization with Macrocyclic Molecules
M. Ruben, D. Payer, A. Landa, A. Comisso, C. Gattinoni, N. Lin, J. P. Collin, J. P. Sauvage, A. De Vita, K. Kern
Journal of the American Chemical Society 128(**2006**)15644

Surface-Assisted Assembly of 2D Metal Organic Networks Exhibiting Unusual Three-fold Coordination Symmetry
S. Stepanow, N. Lin, D. Payer, U. Schlickum, F. Klappenberger, G. Zoppellaro, M. Ruben, H. Brune, J.V. Barth , K. Kern
Angewandte Chemie International Edition 46(**2007**)710

Single atoms are the most active: Cu-catalyzed carboxylic deprotonation
D. Payer, T. Strunskus, A. Dmitriev, N. Lin, J. V. Barth, C. Wöll, K. Kern
*BESSY Annual Report 2005 (***2006***)260*